SYNTHESIS OF STABLE NEAR INFRARED RESPONSIVE GOLD NANOPARTICLES FOR PLASMONIC PHOTOTHERMAL THERAPY APPLICATIONS

A
Thesis
For the award of

Doctor of Philosophy

Submitted by

PARVEER KAUR
(Registration No. 901212005)

Under the Supervision of

Dr. Bhupendra Chudasama

School of Physics & Materials Science
THAPAR INSTITUTE
OF ENGINEERING & TECHNOLOGY
(Deemed to be University)

Patiala
India

AUGUST 2017

DEDICATION

This dissertation is dedicated first and foremost to myself. I never expected to arrive at such a great stage of my life.

I also dedicate my thesis to my parents and my parents-in-laws, for their love, patience, kindness, support and their belief in me.

My brother and sister-in-law for bearing my frustrations and temper and making me feel comfortable with their love and care.

To my loving husband, Inderpreet, for his friendship, love, patience, humour and willingness in my every decision.

CERTIFICATE OF ORIGINALITY

I certify that this thesis fully or partially has not been submitted for any other degree or diploma in any other university or other institute of higher learning.

I also certify that the thesis does not contain any material previously published in another name or written by another person except where due acknowledgement is made in the text.

I also certify that thesis has been written by me and that to my knowledge and belief, any help I have received in preparing the thesis and all sources used have been acknowledged in the thesis.

Parveer Kaur

Parveer Kaur
(Regd. No. 901212005)

School of Physics and Materials Science
Thapar Institute of Engineering & Technology (TIET)
Patiala-147001

Date: 24/02/2018
Place: Patiala

CERTIFICATE

This is to certify that the thesis entitled "**Synthesis of Stable Near Infrared Responsive Gold Nanoparticles For Plasmonic Photothermal Therapy Applications**" which is being submitted by **Parveer Kaur** for the partial fulfilment of the requirement for the Award of the Degree of Doctor of Philosophy in the School of Physics and Materials Science, Thapar Institute of Engineering & Technology, Patiala (Punjab), India is an exclusive record of candidate's own research work under my supervision. This thesis in part or full has not been submitted in any other University or Institute for the award of any degree. This thesis is fit to be considered for the award of degree of Doctor of Philosophy.

B. Chudasama

Dr. Bhupendra Chudasama
(Supervisor)
Associate Professor
School of Physics and Materials Science
Thapar Institute of Engineering & Technology (TIET)
Patiala-147004 (INDIA)

Dated: 24/02/2018

Place: Patiala (India)

ACKNOWLEDGEMENT

It is not a fair task to acknowledge all the people who made my doctoral thesis possible with few words. However, I will try to do my best to extend my great appreciation to everyone who helped me scientifically and emotionally throughout this study.

I shall begin with God the Almighty: without His will I would have never found the right path. His mercy was with me throughout my life and ever more in this study. I am grateful to God for enlightening my soul with the respect, love and concern for the other humans and allowing me to enter a field where I could practice this desire.

With great appreciation, first and foremost, I offer my sincerest gratitude to my advisor, Dr. Bhupendra Chudasama, Associate Professor, School of Physics and Materials Science, TIET, Patiala, for his patience, motivation, enthusiasm and immense knowledge sharing. He patiently provided the vision, encouragement and advice necessary for me to proceed through the doctoral program and complete my thesis. I simply could not have had a better and more concerned advisor. He has been generous with his knowledge, approachable to clarify doubts and willing to assist me overcome whatever hurdles I came across during my doctoral research. He always guided me to work towards substantial long-term objectives, structure my research, present my ideas effectively and promote both myself and my research results. I am where I am all because of his selfless efforts and support. I am also thankful for the excellent example he has set as a successful young scientist and professor.

With great appreciation I would like to express my gratitude towards Dr. O. P. Pandey, Senior Professor and Dean Research and Sponsored Projects, TIET, Patiala, for his invaluable support and cooperation. I am thankful to him for providing the necessary research facilities to meet the goals of this assignment.

I would like to express my special appreciation and thanks to Dr. Kulvir Singh, Professor, School of Physics and Materials Science, TIET, Patiala, for encouraging my research and appreciating me to grow as a research scientist. Your advice on both research as well as on my career have been invaluable.

I am indebted to Dr. Manoj K. Sharma, Head, Professor, School of Physics and Materials Science, TIET, Patiala, for his support and cooperation. I would also like to acknowledge other members of the doctoral committee, Dr. B. C. Mohantay and Dr. Siddharth Sharma for their encouragement, insightful comments, constructive feedback and challenging questions.

Some faculty members and non-teaching staff of the Institute have been very kind enough to extend their help at various phases of this research, whenever I approached them, and I do hereby acknowledge all of them.

I would like to express sincere thanks to Dr. Manoj Baidwal, Assistant Professor, Department of Biotechnology, TIET, Patiala for his kind help and assistance and for extending facilities of Animal and Tissue Culture (ATC) Lab. I am thankful to Purnima Sharma for her help and support during experimentation in Animal and Tissue Culture (ATC) lab. I am thankful to SAIF, IIT Bombay, for extending TEM facilities.

I would also like to thank present and past members of the Laboratory of Nanomedicine, Dr. Nidhi Andhariya and Dr. Chandni Khurana, for giving me introduction to the lab and for sharing their knowledge. Many thanks to my juniors Navjot Kaur and Purnima Sharma for their love and cheerful company. My colleagues, Baldeep Kaur, Manpreet Kaur, Navjot Kaur, Anu Gupta and Chandni Rana with whom I started this journey. My brother and friend, Satwinder Singh, for extending his support in a very special way. I gained a lot from my other lab mates through their personal and scholarly interactions, their suggestions at various points of my research programme. I also acknowledge my pals, Dr. Kamaldeep Kaur, Arshdeep Singh, Alice Goyal, Amandeep Kaur, Dr. Gurbinder Kaur and Dr. Gurmeet Singh Lotey for their well wishes. Their friendship and assistance mean a lot to me and my research would not have been possible without their help.

I gratefully acknowledge the funding sources that made my Ph.D. work possible. I was funded by the University Grants Commission, New Delhi, thru Maulana Azad National Fellowship for Minority Classes, for my 5 years as Junior and Senior Research Fellow.

Lastly, I would like to thank my parent-in-laws for all their encouragement, my parents who raised me with love and supported me in all my pursuits. My brother and sister-in-law for their naughty-fights and constant support and most of all for my loving, supportive, encouraging and patient husband *Inderpreet* whose faithful support during the final stages of this Ph.D. is so appreciated. Lastly, to all those who came and left me knowingly or unknowingly in these years of my life. Thank you.

Parveer Kaur

List of publications:

SCI Journals

1. Parveer Kaur and Bhupendra Chudasama, "*Single step synthesis of pluronic stabilized IR responsive gold nanoplates*", RSC Advances, 4, **(2014),** 36006–36011, Impact factor: 3.108.

2. Parveer Kaur and Bhupendra Chudasama, "*Effect of Colloidal Medium on the Shelf-Life and Stability of Gold Nanorods Prepared by Seed-Mediated Synthesis*", Journal of Nanoscience and Nanotechnology, 17, (**2017**), 1-10, Impact factor: 1.459

3. Parveer Kaur and Bhupendra Chudasama, "*Seedless Co-Surfactant Based Dimensional and Optical Tunability of Gold Nanorods with Simultaneous pH Regulation*", Journal of Materials Science, 52, (**2017**), 11675–11687, Impact Factor: 2.599

4. Parveer Kaur and Bhupendra Chudasama, "*Enhanced optical and dimensional stability of as-synthesized GNRs via seedless synthesis*", Journal of Physical Chemistry C *(communicated).*

5. Parveer Kaur and Bhupendra Chudasama, "*Size and shape dependent cytotoxic studies of GNRs and GNPs on RAW 264.7 Macrophage cells*", Journal of Biomedical materials B *(communicated).*

Non-SCI Journals

1. Parveer Kaur and Bhupendra Chudasama, "*Study of seed aging in seed-mediated synthesis of IR responsive gold nanorods*", 1591, 543, 2014, AIP Conference Proceedings, American Institute of Physics.

Conference Presentations:

Oral Presentations

1. Parveer Kaur and Bhupendra Chudasama. "*Enhanced Stability of Pluronic F-127 Stabilized Plasmonic Gold Nanorods*". International Conference on Nanoscience and Nanotechnology (ICNN-2013), Babasaheb Bhimrao Ambedkar University, Lucknow, India (**2013**).
2. Parveer Kaur and Bhupendra Chudasama. "*Study of Seed Aging in Seed-mediated Synthesis of IR Responsive Gold Nanorods*". 58th DAE Solid State Physics Symposium, held at Thapar University, Patiala, India (**2013**).

Poster Presentations

1. Parveer Kaur and Bhupendra Chudasama. "*Synthesis of Gold Nanorods for Optical Hyperthermia of Cancer*". National Conference on Innovative Molecules for Sustainable Future (NCIMSF), Thapar University, Patiala, Punjab, India (**2013**).
2. Parveer Kaur and Bhupendra Chudasama. "*Study of Seed Aging in Seed-mediated Synthesis of IR Responsive Gold Nanorods*". 58th DAE Solid State Physics Symposium, held at Thapar University, Patiala, India (**2013**).
3. Parveer Kaur and Bhupendra Chudasama, "*Tuneable Plasmonic Properties of NIR Responsive Gold Nanorods for Photothermal Therapy of Cancer*", International conference on condensed matter physics (ICCMP-2014), held at Shimla University, India (**2014**).
4. Parveer Kaur and Bhupendra Chudasama, "*Effect of Storage Medium on the Stability of Gold Nanorods for Photothermal Therapy of Cancerous Tumors*", International symposium on Nanotechnology and Cancer Theranostics (ISNACT-2015), held at IIT Mumbai, India (**2015**).

TABLE OF CONTENTS

CHAPTER 1

INTRODUCTION

1.1 CANCER: AN OVERVIEW

Cancer is a group of disease caused by unrestrained evolution of cells due to malfunctioning of the genes responsible for cell growth and division [1]. This unrestricted phenomenon, if not controlled, could lead to death. It is not a new disease. Paleopathological findings indicate that tumors existed in animals since prehistoric times, long before man appeared on Earth. The earliest evidences of cancer were found in mummies in ancient Egypt, which were scripted in ancient manuscripts that are as old as 1600 B.C. [2]. The term 'Cancer' originates from a Greek word "Karkinos" to describe carcinoma tumors. It was discovered in 460-370 B.C. by physician Hippocrates. Egyptians attempted to treat tumors and cancer with cautery, knives and salts, and introduce arsenic paste that remained in use as ''Egyptian ointment'' until the 19^{th} century [3]. With the development in the understandings of the human body from 15^{th} to 17^{th} century, John Hunter the Scottish surgeon (1728-1793) suggested surgery as a way to cure cancers [4]. With the birth of modern microscope in the 19^{th} century, the study of oncology flourished. Since 20^{th} century, cancer is known as a leading cause of deaths in both the developed and underdeveloped countries [5]. Both external factors (like, drug intake such as tobacco and alcohol and exposure to harmful chemicals and radiations) and internal factors (imbalanced hormones, inherited mutations, poor diet, physical inactivity and reproductive changes) are the main causes of cancer [6].

Based on GLOBOCON estimates, 14.1 million new cancer cases and 8.2 million deaths occurred worldwide in 2012 [7]. With more than 10 million new cases every year, cancer has become the most devastating disease worldwide. With the advancement in cancer diagnosis and treatment in the developed countries, 65 % deaths worldwide due to were reported from the developing countries. Lung cancer is the leading cause of cancer deaths among male in both the developed and developing countries and has surpassed the breast cancer which is the leading cause of cancer death among females in developed countries (**Fig. 1.1**). Breast cancer remains the leading cause of cancer deaths among females in developing countries. Other leading causes of cancer deaths in developed countries include

colorectal cancer and prostate cancer among males. In developing countries, liver and stomach cancer among males and cervical cancer among females are also the leading causes of cancer deaths (**Fig. 1.1**).

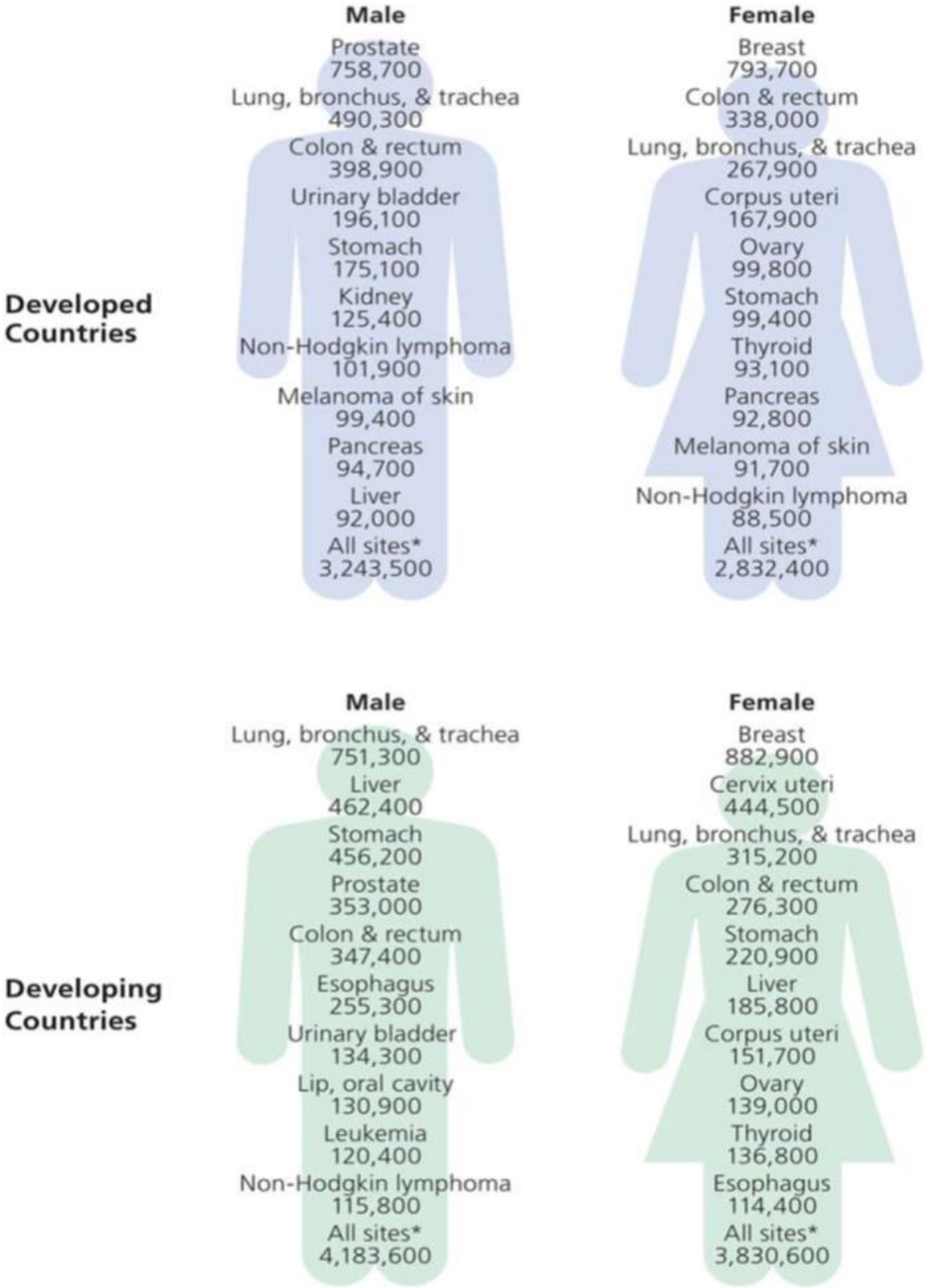

Fig. 1.1 Estimated new cancer cases worldwide by sex and level of economic development [1].

Although incidence rates for all cancer combined are nearly twice as high in developed countries as compared to developing countries in both the males and the females, mortality rates are only 8-15% higher in developed countries [8]. This disparity is due to regional differences in risk factors and detection practices and/or the availability of treatment.

Advanced treatment methods are required in most of the cases and ongoing research initiatives are not sufficient for the complete understanding of disease and its control. Technological advances and the ever increasing understanding of cancer make this field one of the rapidly evolving areas of modern medicine.

1.2 CANCER THERAPY

1.2.1 Conventional Treatments

The kind of a treatment that a patient will receive depends upon the type and the stage of cancer. Conventional therapies for cancer treatment include surgery, radiation therapy, and chemotherapy or combined strategies for these treatments. Other than these, targeted therapy, hormonal therapy, immunotherapy therapy and photodynamic therapies have also been attempted.

Surgery is the ancient form of cancer treatment [9]. Most solid tumors are cured with this treatment. Taking into account the tumor size, extent of spread, and other characteristics, it can be entirely removed by surgery. It is a primary treatment for many types of cancer. If the cancer has metastasized in the body prior to surgery, complete surgical excision is usually impossible. The other limitation of surgery is patient loses the organ and there are strong chances of reoccurrence of cancer.

Second most widely used treatment method for cancer is radiation therapy [10]. In this therapy, cancerous tumors are burnt by radiations like gamma rays, X-rays and high-energy particle like neutrons or pi-mesons [10]. Radiation therapy is a local treatment, as it only affects the part of the body which is infected with cancer. In many cases radioisotopes are implanted in tumors [11]. When high energy radiations interact with tumor, they ionize the water or proteins or other molecules in the tumor cells' cytoplasm or DNA. This passivates the bioactivities of the cell, thus inhibiting the cell mutation resulting into the cell death. The goals of the radiation therapy include, shrinking of the tumor size before the surgery, minimizing the possibility of cancer reoccurrence after surgery, eliminating cancer

cells in other parts of the body, and pain management. Side effects from radiation therapy may include fatigue, mild skin reactions, upset stomach, and loose bowel movements. Internal radiation therapy may cause bleeding, infection or irritation after the implant is removed. The major limitation of radiation therapy is: it can damage healthy cells too in the vicinity of tumor. In addition, burning of cancerous cells' is non uniform and the burnt part may become nonfunctional.

Chemotherapy is the third modality of cancer treatment [12]. It is used to treat cancers that can no longer be treated with localized methods such as surgery and radiation therapy. It works by slowing or stopping the growth of cancer cells by drug's toxic effects or by stopping them from getting nutrients needed to divide or by inhibiting the mechanism responsible for cell division. Taxol and doxorubicin or daunorubicin adversely affects the process of cell division, thus are expected to destroy aggressive cancers. Side effects of chemotherapy include fatigue, risk of infection, nausea and vomiting, loss of appetite and diarrhea. These side effects usually go away once the treatment is over. The limitation of this approach is that the chemotherapeutic drugs do not distinguish between healthy and cancerous cells and hence damage them too. This approach is rarely successful if the cancer is in the advance stage.

Over the past 25 years, chemotherapy has improved significantly but still it is far from eliminating cancer from the globe. Specialized therapies, such as targeted therapy [13] use specific monoclonal antibodies or small molecule inhibitors to interfere with the specific molecules which are necessary for tumor growth and progression. This treatment modality can be applied for certain malignancies, such as, breast cancer, lung and pancreatic cancers, leukemia, lymphoma and multiple myeloma [13]. The toxicity of targeted therapies to healthy cells is quite low as compared to traditional chemotherapy.

Several types of cancer only grow and spread in the presence of hormones. Hormonal therapy therefore treats cancer by lowering the amounts of androgen levels necessary for tumor growth in the body [14]. It is generally used to treat cancers of the prostate, breast, thyroid and reproductive system. As like any other treatments hormonal therapy has severe side-effects and most of these vanish once the patient finishes the treatment. Side effects of the hormonal therapy depend on the drug used and often affects male and female differently.

Immunotherapy improves body's self-defense against cancer [15]. It is a treatment for specific cancers that affect the immune system; like cancer of lymphatic tissues (lymphoma) and cancer of leukocytes (leukemia). Administration of cytokines or monoclonal antibodies stimulates the patient's immune system. Cytokines binds to the cancer cells. It enhances the activity of the immune cells and increases the natural ability of the body to repair cells that are damaged by radiations or chemotherapy.

Photodynamic therapy (PDT) also known as photo-radiation therapy, phototherapy, or photo-chemotherapy is a treatment modality that uses photosensitizing agents along with light to kill cancer cells [16]. Photosensitizer drugs have toxic effects only after they have been exposed to visible radiation. Depending on the part of the body being treated, photosensitizer is either being put into the bloodstream or implanted below the skin. It is then absorbed by the cancer cells. Following this the tissue to be treated is exposed to light. It excites the photosensitizer drug which then reacts with the oxygen and releases the toxic singlet oxygen which irreversibly kills the cancer cells [16]. PDT also works by destroying the blood veins that feed the cancer cells and by stimulating the immune system against cancer cells. This therapy has no long-term side effects. It is less invasive as compared to surgery. Unlike radiation therapy, PDT can be repeated many times at the same site, if needed. There is little or no scarring after the site heals. It often cost less than the other cancer treatment modalities. PDT has some serious limitations, too. It can only treat tissues or organs where light can reach. This means that it can be used to treat tumors on or just under the skin, or in the lining of internal organs such as melanomas, head and neck cancer and tumors of the bladder [17, 18]. The patient remain highly sensitive to light after the treatment, hence special precautions are required once the drug is injected into the body.

Hyperthermia is a treatment modality in which cancerous cells/tissues are exposed to temperature in the range of 41–47°C [19]. Tumors are destroyed in this temperature range because of their reduced heat tolerance as compared to healthy tissues. Hyperthermia can be achieved by different means of heating such as, radiofrequency [20], high-intensity focused ultrasound [21], microwaves and photothermal [22, 23]. These conventional means of hyperthermia is not much popular as it causes extensive damage to surrounding healthy tissues. A revolution in cancer therapy can be achieved if controlled and confined thermal damage in the tumor tissue can be produced with laser light and photosensitive materials

[24]. The photo absorbing materials can be natural chromophores already present in the tissues or externally added dye molecules, like neocyanine green [25], porphyrins [26] and naphthalocyanines [27] synchronized with transition metals. The major problem with these dye molecules is their photobleaching under laser irradiation. Thus there is a need for exogenous photothermal agents that has high optical absorption cross-section, as well as being efficient at converting incident light into heat, making the therapy less invasive due to lower incident laser powers. Innovation in nanoscience has led to nanostructures with various shapes that exhibit novel optical and photonic properties [28]. These nanoparticles can be used in hyperthermia for localized treatment of cancer. At present two different variants of nanoparticles based hyperthermia is under active clinical trials. One of them uses AC magnetic field to induce hyperthermia through magnetic nanoparticles while the other one uses visible and NIR radiations to induce optical hyperthermia with plasmonic nanostructures.

1.2.2. Nanomaterials in Cancer Therapy

Delivery of chemotherapeutic drugs only to the infected tissues within the body is a major challenge to the clinicians. Chemotherapeutic drugs when injected intravenously results into non-specific distribution in the body thus affecting both the cancerous and the normal cells. Only part of the drug reaches to the cancerous cells resulting into suboptimal treatment and unnecessary toxicity to normal cells [29]. Preferential and specific delivery of drugs to their biological targets can be improved by means of metal nanoparticles [30]. Due to their small size, high colloidal stability, optical activity and ability to conjugate with the tumor specific ligands, metal nanoparticles are widely exploited in optical hyperthermia [31]. They can be used in active and passive therapy of cancer hyperthermia.

In active targeting, surface of the nanoparticle is modified by monoclonal antibodies, aptamers, ligands or folates and peptides in order to interact with the receptors at the surface of cancer cells [32]. In passive targeting, nanoparticles travel into the tumors due to large interstitial spacing between their vasculatures [32]. This leads to localization of nanoparticles in tumors due to their high permeability and retention. This effect is known as enhanced permeability and retention (EPR) [33].

Growth of tumor is accompanied by angiogenesis i.e. formation of new blood vessel in order to fulfill the increasing demand of nutrition and oxygen by growing tumor [33]. This

neovasculature thus formed in tumor cells is different from those of normal cells. Vessels in tumors are leaky, irregular, defective and poorly aligned with large fenestrations. Tumor vessels have wide lumen whereas tumor tissues have poor lymphatic drainage. Due to structural defectiveness and functional abnormalities within the tumors, there is an excessive leakage of blood plasma components, like, macromolecules, lipidic particles and nanoparticles [34]. Poor lymphatic drainage retains these components into the tumors for longer time, whereas extravasation into tumors continues. EPR effect thus differentiates normal tissues from cancerous cells. This phenomenon of EPR effect is the basis of effective targeting of drugs to tumor sites by means of functionalized nanoparticle. The schematic representation of functioning of EPR effect is shown in **Fig. 1.2**. Thus considerate use of nanoparticles that can exploit the EPR effect and targeting moieties which can guide the drugs to the cells, can serve as worthy recipe for improved cancer therapy.

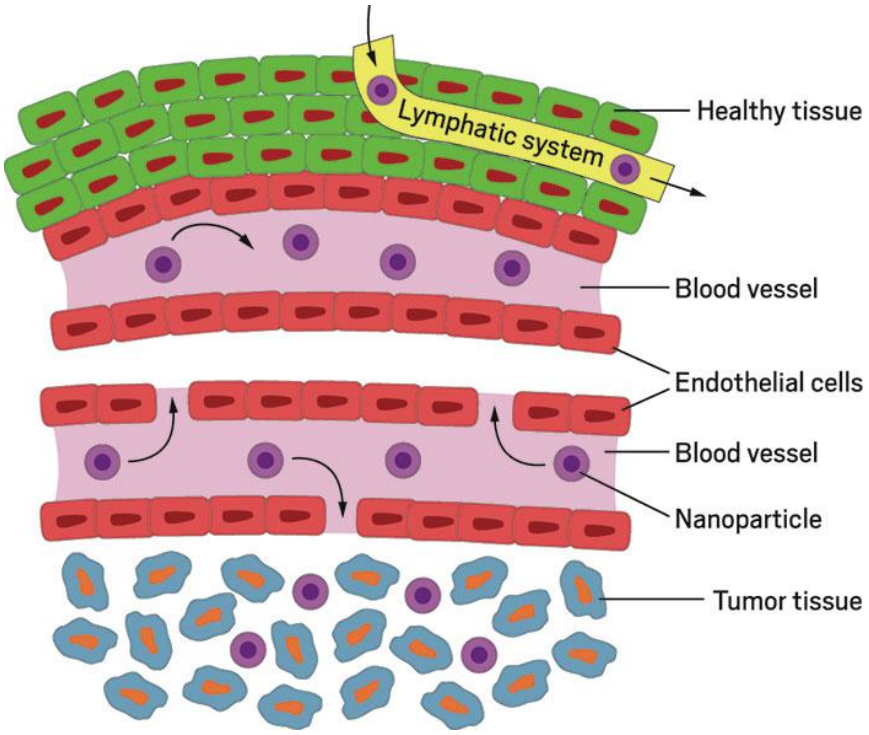

Fig. 1.2 Cartoon representations of enhanced permeability and retention (EPR) effect in tumors [34].

In magnetic hyperthermia [35] tissues are heated by alternating magnetic field in the presence of magnetic nanoparticles. The goal of this approach is to heat specifically and exclusively the local tumour region by means of the magnetic losses of nanoparticles in an external, alternating magnetic field. In an alternating magnetic field, magnetic nanoparticles

dissipate heat in response to the alternating field by means of Brownian or Neel rotation. Heat is generated through hysteresis and relaxation losses.

Optical hyperthermia also known as photothermal therapy [PTT] is a therapeutic process in which PTT agents absorb electromagnetic radiation and excites electrons [30]. This electronic excitation energy subsequently relaxes through non-radiative decay channels leading to heating of the local environment around the PTT agents. Metal nanoparticles can be used as PTT agents because of their enhanced absorption cross sections, which are four to five orders of magnitude higher than those offered by conventional photo absorbing dyes. This strong absorption ensures effective laser therapy at relatively lower impact energies rendering the therapy method minimally invasive. In addition, metal nanostructures have higher photostability and they do not undergo photobleaching [30].

Amongst metal nanoparticles, gold is a potential candidate as PTT agent in photothermal therapy of cancer. Various gold nanoparticle shapes like nanospheres [36], rods [37], plates [38], shells [39], cubes [40] cages [41] have been explored as PTT agents in literature. Amongst these nanostructures gold nanorods (GNRs) and gold nanoplates (GNPs) are highly promising because of ease of preparation, surface functionalization and tunable optical properties. Photothermal therapy when performed with plasmonic gold nanoparticles. It is known as plasmonic photothermal therapy (PPTT) [30]. When gold nanoparticles are irritated with electromagnetic radiation, strong surface fields are induced due to the coherent excitation of the electrons which is known as surface plasmon resonance (SPR) [37]. Rapid relaxation of these excited electrons produces strong localized heat which is capable of destroying surrounding cancerous cells.

There are two decay channels for the optical excitation in the nanoparticles: radiation damping which involves transformation of the plasmons into photons (scattering) and non-radiative decay into electron-hole excitations (absorption). The non-radiative decay occurs via excitation of electron-hole pairs either within the conduction band (intraband excitation) or between the d band and the conduction band (interband excitation) (**Fig. 1.3**) [42].

Metal nanostructures when excited with incident light of resonant frequency, it results in the formation of electron clouds which subsequently relaxes through decay channels rapidly within ~1 ps by exchanging energy with the nanoparticle lattice [43]. These electronic excitations within the nanoparticles' lattice generate heat energy. Nanoparticles'

lattice cools by phonon-phonon interactions by exchanging energy with the surrounding medium in a time scale of 100 ps. Thus low rate dissipation of heat as compared to its generation can be used for localized heating in tumor environment. Temperatures up to few thousand kelvins can be easily reached in nanoparticles with laser power as low as 100 nJ [30]. This high flux of heat generation by gold nanoparticles by absorbing light of resonant frequency makes them a promising candidate for plasmonic photothermal therapy (PPTT) of cancer.

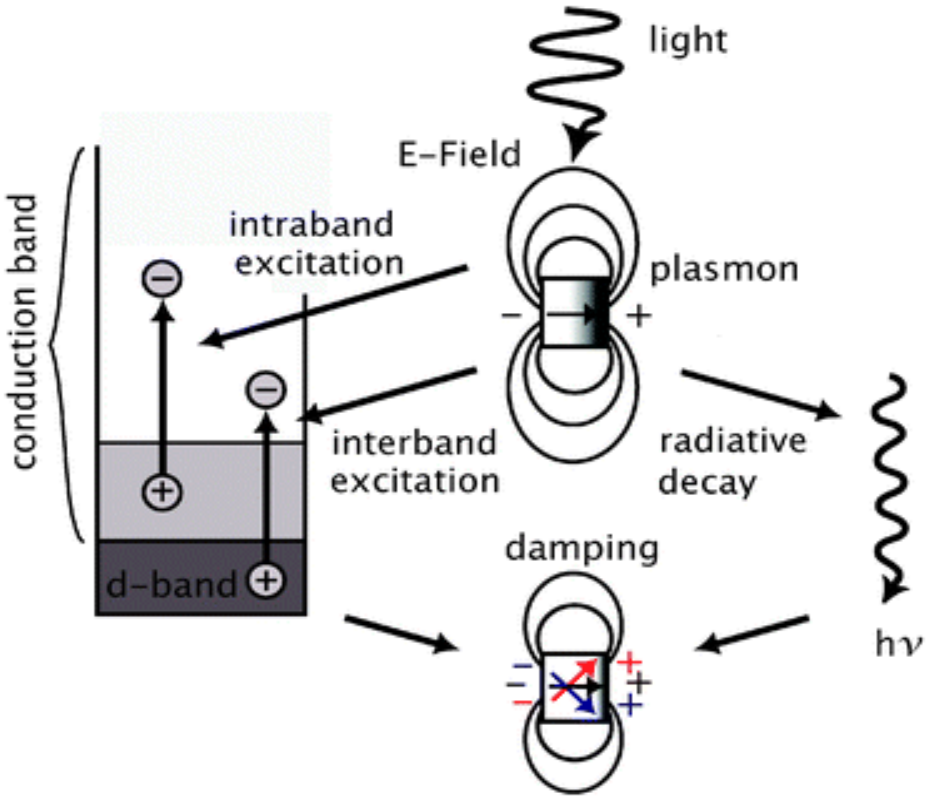

Fig. 1.3 Radiative and non-radiative decay channels in noble-metal nanoparticles [42].

SPR of gold nanoparticles strongly depend on the size, shape as well as dielectric constant of the surrounding medium, thus allowing unique optical tunability of plasmon resonance band of these nanoparticles [44]. With increase in the size of spherical gold nanoparticle, SPR band undergoes a red-shift [37]. On changing the shape of nanoparticles from sphere to rods or plates, SPR band of spherical gold nanoparticles splits into two bands: strong long-wavelength band into the NIR region due to the longitudinal oscillations of the electrons and a week short-wavelength band in the visible region due to the transverse

oscillations of the electrons [45]. The longitudinal absorbance of the nanorods is highly sensitive to the aspect ratio of these anisotropic nanostructures. With increase in the aspect ratio, the longitudinal band red-shift to the NIR region. GNRs and GNPs, can absorb radiation heavily in the NIR region. Light penetration is optimal in the NIR region due to minimal absorption by tissues, water and blood in this window [45]. This makes NIR responsive gold nanostructures highly promising for clinical therapies of tumors that are located deep within the body tissues.

1.3 SPR IN GOLD NANOPARTICLES

1.3.1 SPR in Spherical Gold Nanoparticles

Metal nanoparticles with small sizes (< 100 nm) exhibit complex optical and physical properties due to confinement of the electrons in small size. The conduction band electrons of metal nanoparticles undergo collective coherent oscillations with the incident electromagnetic light of resonant frequency. This phenomenon is known as surface plasmon resonance (SPR) [46.]. Gold nanoparticles of sub-wavelength size show strong absorption, in the presence of oscillating electromagnetic field. This is known as localized surface plasmon resonance [47]. As a consequence, nanoparticles exhibit bright colors both in transmitted and reflected light due to resonance enhanced absorption and scattering. A charge separation is induced between the free electrons and the ionic metal due to these oscillations, which in turn exerts a restoring Coulomb force that makes electrons oscillate back and forth on the nanoparticle surface resulting in the dipole oscillations (**Fig. 1.4**) [48]. Interaction of the nanoparticles with the electric field results in polarization of electrons with respect to the ionic core of the nanoparticle. The polarizability α, of the spherical metal nanoparticles is [48]

$$\alpha = 4\pi a^3 \frac{\epsilon_M - \epsilon_0}{\epsilon_M + \epsilon_0} \qquad 1.1$$

Where 'a' is the radius of the nanoparticle; ϵ_M is dielectric constant of isotropic and non-absorbing medium and $\epsilon_0$is the dielectric constant on nanoparticles surface. The SPR of spherical nanoparticles induce strong absorption of electromagnetic radiations at ~520 nm (**Fig. 1.5**) [49].

Mie explained the SPR in spherical metal nanoparticles by using Maxwell's equations. For small metal nanoparticles, only the dipole oscillations contribute to the extinction cross section. According to Mie's theory extinction cross section (C_{ext}) can be defined as:

$$C_{ext} = 9\frac{\omega}{c}V\frac{\epsilon}{[\epsilon_1+\epsilon_2]^2+\epsilon_2^2} \qquad 1.2$$

Where V is the volume of colloidal solution containing nanoparticles, ω is the angular frequency of the incident light, c is the speed of light, and ϵ_0 is the dielectric constant of the surrounding medium and $\epsilon = \epsilon_1 + i\epsilon_2$, is the dielectric constant of the metal. The resonance condition is fulfilled when $\epsilon_1(\omega) = -2\epsilon_0$, if ϵ_2 is small or weakly dependent on ω [50].

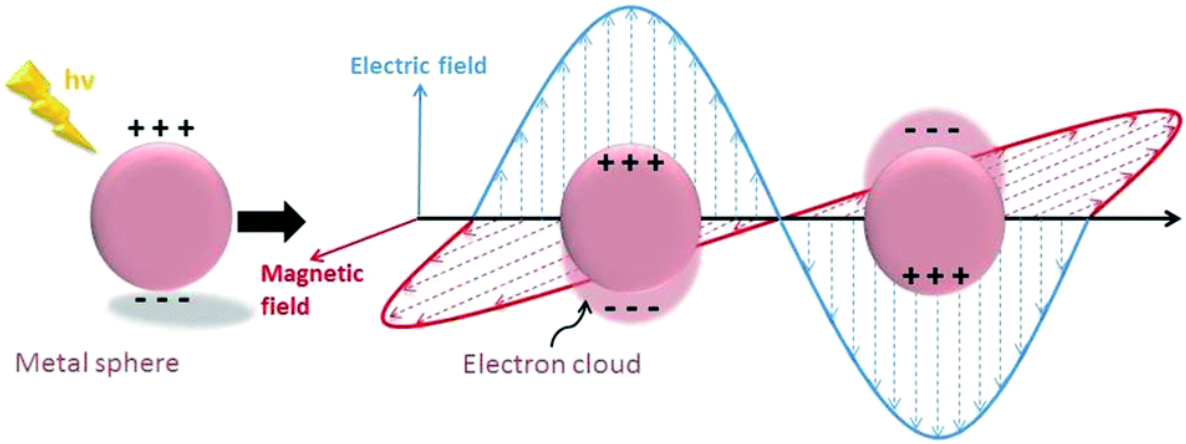

Fig. 1.4 Surface plasmon resonance in spherical gold nanoparticles, showing the displacement of the conduction band electron cloud relative to the ion core resulting in the dipole surface oscillations of plasmons [48].

For larger size nanoparticles (d>100 nm), the light is not able to polarize the nanoparticles homogeneously and the retardation effect leads to the extinction of higher-order modes [51]. From equation (1.2), it can be seen that the peak intensity and position of the SPR absorption band is dependent on the size and shape of the metal nanoparticles as well as on the dielectric constant of the metal and the medium surrounding the nanoparticles. As the size of the nanoparticle increases, the absorption maximum undergoes a red shift (**Fig. 1.6 (a)**). Band width too is affected (**Fig. 1.6 (b)**) [52].

Link and El-Sayed have shown that the band width decrease with the increase in the nanoparticle size when the nanoparticle are less than 20 nm and it increases with the increase in the nanoparticle size when the size of nanoparticles are greater than 20 nm [50]. It is also observed that the absorption coefficient is linearly depending on the volume of the nanoparticles, which is also in agreement with the Mie theory (**Fig.1.6 (c)**) [50]. Spherical nanoparticles of gold, silver and copper have their SPR in the visible region. Amongst these metal nanoparticles silver has highest absorption coefficient, followed by gold. The absorption coefficient of copper is quite low as compared to the gold and silver [52].

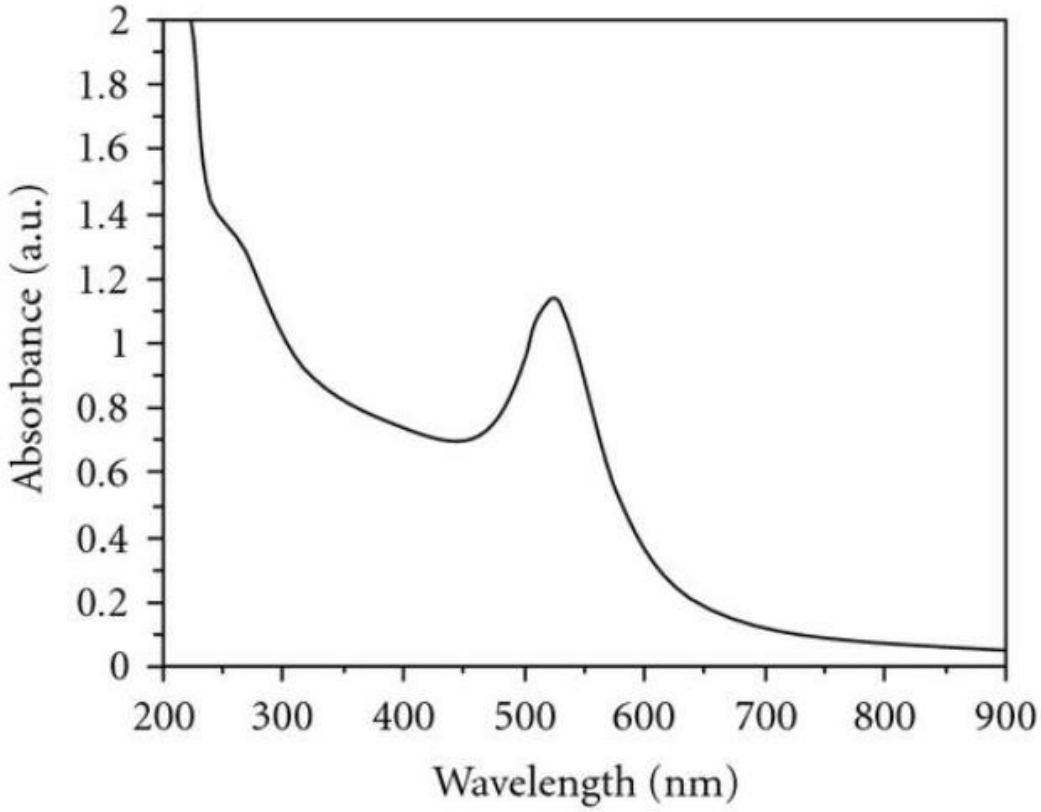

Fig. 1.5 UV-Visible spectra of spherical gold nanoparticles. A surface plasmon absorption band centered at 520 nm is due to the collective coherent oscillations of electrons on the surface of nanoparticles.

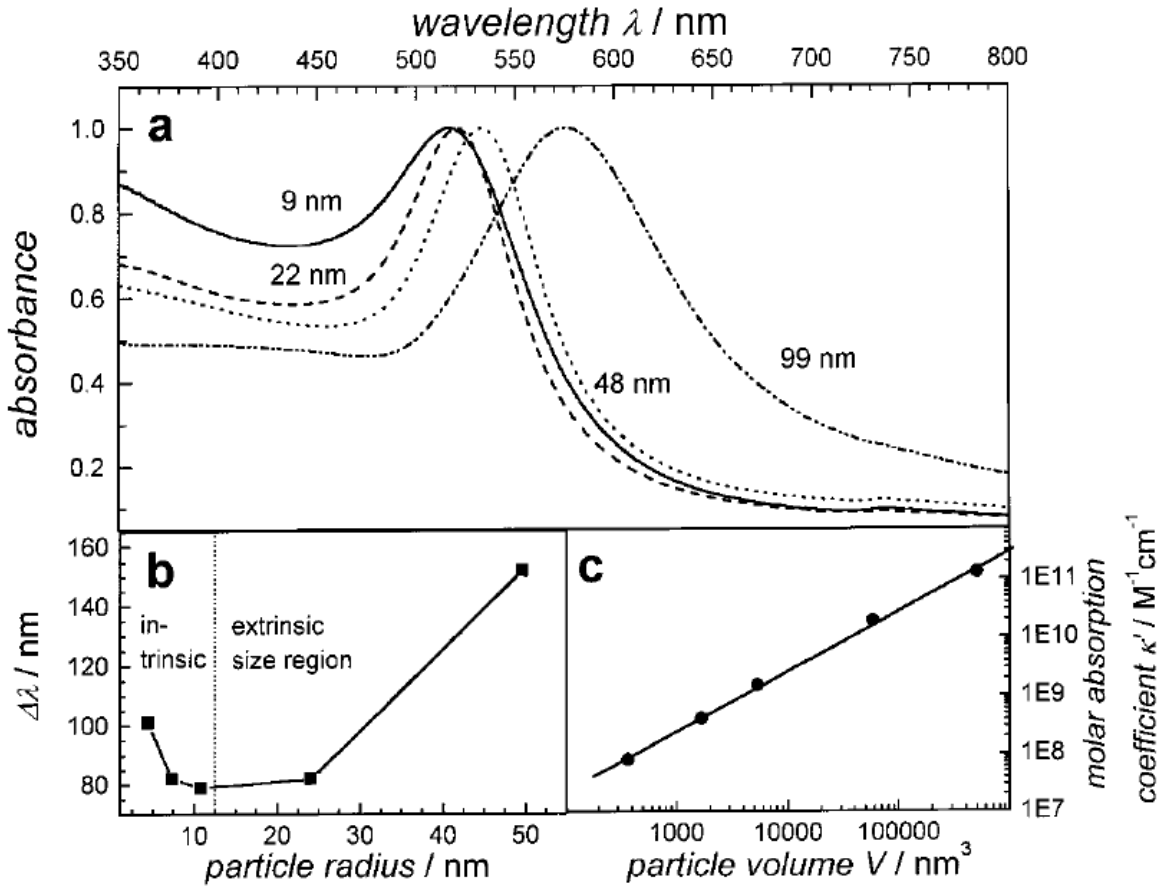

Fig 1.6 Effect of size on the surface plasmon absorption band of spherical gold nanoparticles. (a) UV-Visible absorption spectra of gold nanoparticles with diameters ranging between 9 and 99 nm. It shows that with increase in particle size, the absorption maximum red-shifts towards higher wavelength. (b) The bandwidth increases as the nanoparticles size decreases in the intrinsic size region and increases with increase in radius of nanoparticles in the extrinsic size region. (c) The extinction coefficients have a linear dependency on particle volume [50].

1.3.2 SPR of Anisotropic Gold Nanoparticles

Anisotropic metal nanostructures, such as triangles [53], branched [54], rods and plates have SPR band which is red shifted as compared to their spherical analogs. For metal nanorods and plates, electron cloud can oscillate either along the short axis or along the long-axis (**Fig 1.7**).

SPR along the short axis, known as transverse oscillations absorbs in the visible region. This plasmon resonance band is similar to those observed for gold nanospheres. The optical excitation along the long axis provides a stronger absorption in the higher wavelength region. This is referred as the longitudinal oscillations [55]. While the transverse band is

insensitive to the size of the nanorods, the longitudinal band undergoes a red-shift into the near infrared (NIR) region as the size/aspect ratio of GNRs increases. This shape dependence was explained by Gans theory which is based on discrete dipole approximation [56]. According to discrete dipole approximation (DDA), the SPR absorption maximum (λ_{max}) corresponding to oscillations along the long axis is linearly proportional to the aspect ratio (R) [57]:

$$\lambda_{max} = 95R + 420 \qquad 1.3$$

thus, SPR band corresponding to the longitudinal oscillations can be tuned into the tissue transparent window of NIR region by appropriately tuning the aspect ratio of GNRs modeling synthesis protocols in wet-chemical synthesis.

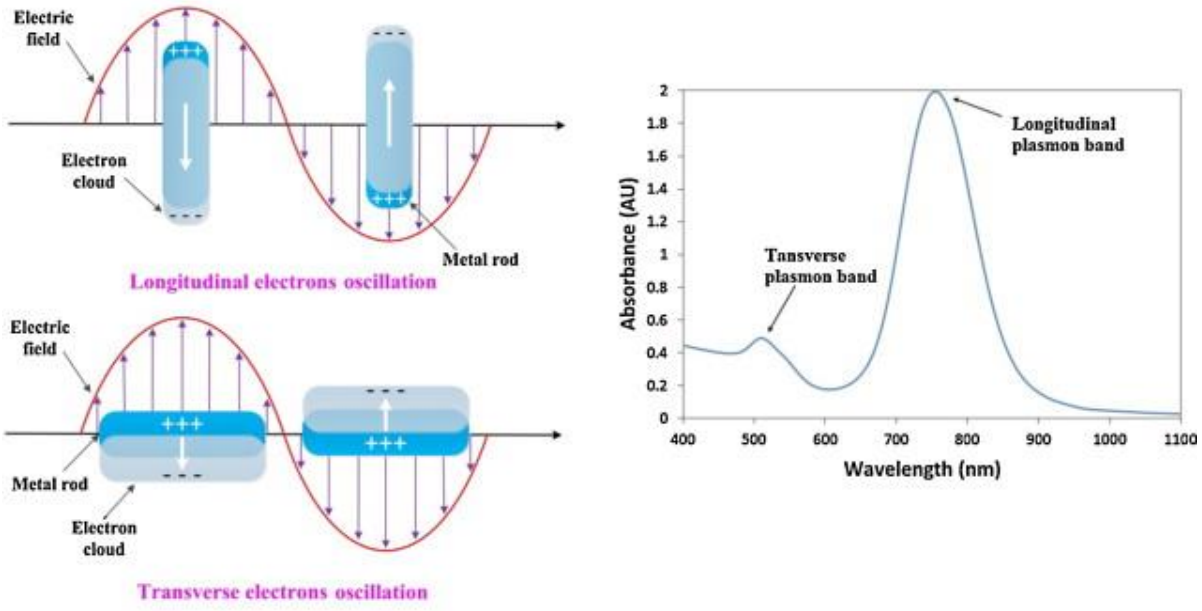

Fig. 1.7. Schematic representation of the interaction of polarized light in nanorods that form coherent SPR along the long and short axis of nanorods [55].

1.4 BIOCOMPATABILITY OF GOLD NANOPARTICLES

Gold metal in its bulk form is biocompatible [58]. However, gold at nanoscale could be toxic. Although successive studies are carried out to evaluate the biocompatibility of gold nanoparticles *in-vitro* they remain inconclusive. Spherical gold nanoparticles and GNRs are being widely investigated in photothermal therapy due to their plasmonic properties. Colloidal gold nanoparticles contain gold metal bound with capping and stabilizing agents

and many left-over chemicals [59]. Toxicity could arise from any of these components from the colloid. Thus evaluating the contribution of each component is essential to understand the origin of toxicity. Goodman et al. have observed that 2 nm cationic-gold nanoparticles are about seven times cytotoxic than their anionic counterparts [60]. Pernodet et al. studied the concentration dependent toxicity of gold nanoparticles that in turn depends on the number of particles inside the cells [61]. It is found that 10 nm and 50 nm citrate-capped gold nanoparticles are non-toxic to embryo fibroblast cells, but they cause adverse effect on cellular proliferation [61]. Patra et al. found that toxicity of nanoparticles is cell type dependent. 33 nm gold nanoparticles were non-toxic to hamster kidney cells HepG2 but toxic to human carcinoma cell line A549 [62].

Surface coating of the GNRs drastically affects the biocompatibility and toxicity and their cellular uptake [63-66]. GNRs are synthesized using cetyltrimethlyammonium bromide (CTAB). Excess CTAB is toxic can cause cell death [67]. Functionalization of GNRs with biocompatible polymers improves their biocompatibility [68]. For example, coating CTAB-capped GNRs with polyelectrolytes [69], replacing or exchanging surface-bound CTAB with biocompatible phospholipids or polyethylene glycol [70], free-radical polymerization of CTAB-bound nanorods [65] can effectively improve their biocompatibility. Although rich data of toxicity studies of gold nanoparticles is available, still we lag in successive clinical trials of these nanostructures due to criticism on the prevailing data.

References:

1. Cancer Facts & Figures, *American Cancer Society*, **2013**.
2. A. Sudhakar, *J Cancer Sci Ther.*, **2009**, 1, 1–4.
3. S.I. Hajdu, *Cancer*, **2010**,117, 1097-1102.
4. S.I. Hajdu, F. Darvishian, *Cancer*, **2013**, 119, 1450-1466.
5. R.L. Siegel, K.D. Miller, *CA Cancer J Clin.*, **2015**, 65, 1, 5-29.
6. L.A. Torre, F. Bray, R.L. Siegel, J. Ferlay, J. Lortet-Tieulent, A. Jemal, *CA Cancer J Clin.*, **2015**, 65, 87-108.
7. Cancer Facts & Figures, *American Cancer Society*, **2012**.
8. G.A. Atlanta, *J Consum. Health Internet.*, **2012**, 16, 366-368.
9. C.A. Cullinane, T. Borneman, D.D. Smith, D.Z.J. Chu, B.R. Ferrell, L.D. Wagman, *Cancer*, **2003**, 98, 2266-2273.
10. M.K. Bucci, A. Bevan, M. Roach III, *CA Cancer J Clin.*, **2005**, 55, 117–134.
11. M. Djabełek-Maciaś , I. Wiśniewska, M. Ochman, A. Kołodziejczyk, J. Zebrowski, P. Piwkowski, *Nucl Med Rev Cent East Eur.*, **2006**, 9, 138-143.
12. C.N. Baxevanis, S.A. Perez, M. Papamichail, *Cancer Immunol Immunother.*, **2009**, 58, 317–324.
13. M.M. Sulochana, *World J Pharm Pharm Sci.*, **2016**, 5, 612-626.
14. A. Jones, P.J. Barrett-Leeb, M.D. Mason, *Medicine*, **2004**, 32, 30-32.
15. S.A. Rosenberg, *Immunity*, **1999**, 10, 281-287.
16. M.C. DeRosa, R.J. Crutchley, *Coord. Chem. Rev.*, **2002**, 233, 351-371.
17. A.K. D'Cruz, M.H. Robinson, M.A. Biel, *Head Neck*, **2004**, 26, 232-240.
18. D.E. Dolmans, D. Fukumura, R.K. Jain, *Nat Rev Cancer*, **2003**, 3, 380-387.
19. B.A. Britt, W. Kalow, *J Anesth Hist.*, **1970**, 17, 293–315.
20. A. Jordan, R. Scholz, P. Wust, H. Fahling, R. Felix, *J. Magn. Magn. Mater.*, **1999**, 201, 413-419.
21. P.P. Lele, *Radiat. Environ. Biophys.*, **1980**, 17, 205–217.
22. J. Mendecki, E. Friedenthal, C. Botstein, *Int J Radiat. Oncol. Bio.l Phys.*, **1978**, 4, 1095-1103.
23. T. Niidome, Y. Akiyama, M. Yamagata, T. Kawano, T. Mori, Y. Niidome, Y. Katayama, *J Biomater. Sci. Polym Ed.*, **2009**, 20, 1203-1215.
24. N.J. Halas, *Nanomedicine*, **2009**, 4, 369-371.
25. W.S. Kuo, Y.T. Chang, K.C. Cho, K.C. Chiu, C.H. Lien, C.S. Yeh, S.J. Chen, *Biomaterials*, **2012**, 33, 3270-3278.
26. C.S. Jin, J.F. Lovell, J. Chen, G. Zheng, *ACS Nano*, **2013**, 7, 2541–2550.
27. A. Busettia, M. Soncina, E. Reddia, M.A.J. Rodgersb, M.E. Kenneyc, G. Joria, *J. Photochem. Photobiol.*, **1999**, 53, 103-109.
28. I. Brigger, C. Dubernet, P. Couvreur, *Adv. Drug Deliv. Rev.*, **2002**, 54, 631-651.
29. W.E. Gutteridge, *Br Med. Bull.*, **1985**, 41, 162-168.
30. X. Huang, P.K. Jain, I.H. El-Sayed, M.A. El-Sayed, *Lasers Med Sci.*, **2008**, 23, 217–228.
31. W. Cai, T. Gao, H. Hong, J. Sun, *Nanotechnol Sci. Appl.*, **2008**, 1, 17–32.
32. M.D. Blanco, C. Teijón, R.M. Olmo, J.M. Teijón, *Nano Today*, **2007**, 2, 14-21.
33. A.K. Iyer, G. Khaled, J. Fang, H. Maeda, *Drug Discov., Today*, **2006**, 11, 812-818.

34. M. Torrice, *ACS Cent. Sci*., **2016**, 2, 434–437.
35. A.K. Gupta, M. Gupta, *Biomaterials*, **2005**, 26, 3995-4021.
36. D. Pissuwana, S.M. Valenzuelaa, M.B. Cortie, *Trends Biotechnol.*, **2006**, 24, 62-67.
37. B. Nikoobakht, M.A. El-Sayed, *Chem. Mater.*, **2003**, 15, 1957–1962.
38. L. Chen, F. Ji, Y. Xu, L. He, Y. Mi, F. Bao, B. Sun, X. Zhang, Q. Zhang, *Nano Lett*., **2014**, 14, 7201–7206.
39. S.J. Oldenburg, J.B. Jackson, S.L. Westcott, N.J. Halas, *Appl. Phys. Lett*., **1999**, 75, 2897.
40. S.I. Lim, I.O. Jiménez, M. Varon, E. Casals, J. Arbiol, V. Puntes, *Nano lett*., **2010**, 3, 964-973.
41. J. Chen, F. Saeki, B.J. Wiley, H. Cang, M.J. Cobb, Z.Y. Li, L. Au, H. Zhang, M.B. Kimmey, X. de, Y. Xia, *Nano Lett*., **2005**, 5, 473–477.
42. M. Rycenga, K.K. Hou, C.M. Cobley, A.G. Schwartz, P.H.C. Camargo, Y. Xia. *Phys. Chem. Chem. Phys*., **2009**, 11, 5903-5908
43. E.A. Coronado, G.C. Schatz, *J. Chem. Phys.*, **2003**, 1, 3926-3934.
44. A. Melikyan, H. Minassian, *Appl. Phys. B: Laser Opt.*, **2004**, 78, 453-455.
45. J. Justea, I.P. Santosa, L.M. Liz-Marzána, P. Mulvaney, *Coord. Chem. Rev.*, **2005**, 249, 1870-1901.
46. M.A. El-Sayed, *Acc. Chem. Res.*, **2001**, 34, 257-264.
47. X. Huang, S. Neretina, M.A. El-Sayed, *Adv. Mater.*, **2009**, 21, 4880–4910
48. S. Peiris, J. McMurtriea, H.Y. Zhu, *Catal. Sci. Technol*., **2016**, 6, 320-338.
49. K.A. Willets, R.P.V. Duyne, *Annu Rev Phys Chem.*, **2007**, 58, 267-297.
50. H. Horvath, *J. Quant. Spectrosc. Radiat. Transfer.*, **2009**, 110, 787–799.
51. S. Link, M.A. El-Sayed, *Int Reviews Phys Chem.*, **2000**, 19, 409-453.
52. U. Kreibig, M. Vollmer, *Optical Properties of Metal Clusters*, New York:Springer, **1995**.
53. M. Faraday, *Philos. Trans.*, **1857**, 147, 145-181.
54. Y. Sun, B. Mayers, Y. Xia, *Nano Lett*., **2003**, 3, 675-679.
55. J. Cao, T. Sun, K.T.V. Grattan, *Sens. Actuators. B Chem.*, **2014**, 195, 332-351.
56. X. Huang, S. Neretina, M.A. El-Sayed, *Adv. Mater.*, **2009**, 28, 4880-4910.
57. P.V.A. Rani, G.L.K. Mun, M.P. Hande, S. Valiyaveettil, *ACS Nano*, **2009**, 3, 279–290.
58. A.E. Finkelstein, D.T. Walz, V. Batista, M. Mizraji, F. Roisman, A. Misher, *Ann Rheum. Dis*., **1976**, 35, 251–257.
59. A.M. Alkilany, C. J. Murphy, *J Nanopart. Res.*, **2010**, 12, 2313–2333.
60. C.M. Goodman, C.D. McCusker, T. Yilmaz, V.M. Rotello, *Bioconjug Chem*., **2004**, 15, 897–900.
61. N. Pernodet, X. Fang, Y. Sun, A. Bakhtina, A. Ramakrishnan, J. Sokolov, A. Ulman, M. Rafailovich, *Small*, **2006**, 2, 766-73.
62. H.K. Patra, S. Banerjee, U. Chaudhuri, P. Lahiri, A.K. Dasgupta, *Nanomedicine*, **2007**, 3, 111–119.
63. A. Verma, O. Uzun, Y. Hu, Y. Hu, H.S. Han, N. Watson, S. Chen, D.J. Irvine, F. Stellacci, *Nat. Mater*., **2008**, 7, 588-95.

64. A.M. Alkilany, P.K. Nagaria, C.R. Hexel, T.J. Shaw, C.J. Murphy, M.D. Wyatt, *Small*, **2009**, 5, 701–708.
65. Y.J. Gu, J.P. Cheng, C.C. Lin, Y.W. Lam, S.H. Cheng, W.T. Wong, *Toxicol Appl. Pharmacol*., **2009**, 237, 196–204.
66. B. Nikoobakht, M.A. El-Sayed, *Langmuir*, **2001**, 17, 6368–6374.
67. A.M. Alkilany, C.J. Murphy, *Langmuir*, **2009**, 25, 13874–13879.
68. T.S. Hauck, A.A. Ghazani, W.C.W. Chan, *Small*, **2008**, 4, 153–159.
69. Y.L. Liu, M.K. Shipton, J. Ryan, E.D. Kaufman, S. Franzen, D.L. Feldheim, *Anal. Chem.*, **2007**, 79, 2221–2229.
70. H. Takahashi, Y. Niidome, T. Niidome, K. Kaneko, H. Kawasaki, S. Yamada, *Langmuir*, **2006**, 22, 2–5.

CHAPTER 2

LITERATURE SURVEY

2.1 INTRODUCTION

The primitive realizations in the practice of gold for curative and soothing purposes originated over 5000 years ago in Alexandria in Egypt [1]. Egyptians consumed gold for mental and biological refining. Gold was generally used in medication for its spiritual powers until late Middle Age. Around 1300 AD, Geber dissolved gold by preparing aqua regia, a mixture of hydrochloric and nitric acid. With the dissolution of gold, it began to be used medicines. In the early 17^{th} century gold entered the approved drug compendia. Mid 18^{th} and early 19^{th} century is known for gold's progression in medicine [1]. The modern synthesis of colloidal gold discovered in 1850's, when Michael Faraday reduced gold chloride to prepare colloidal gold using phosphorus [2]. He recognized that the color of the colloid was due to the small size of the particles. In 1890, Robert Koch discovered the bacteriostatic properties of colloidal gold [1]. In the mid-19^{th} century gold was used in curing many diseases like breast and venereal diseases, dysentery, epilepsy, tumors and syphilis [3]. Gold has also been used in several other fields of medicine like dentistry, gene delivery and renal stents etc. [1, 3].

After several decades of intense research nanoparticles of, gold now can be synthesized in variety of shapes and sizes with functionalizable surfaces [4]. Spherical gold nanoparticles are commonly prepared by citrate reduction introduced by Turkevich and Frens [5, 6]. By varying the concentration of gold and citrate, spherical nanoparticles with varying size can be prepared. Control over size and shape could be achieved by carefully varying the experimental conditions such as reduction rate, reaction temperature and time, capping agents, gold precursor, etc. [7, 8]. Spherical gold nanoparticles exhibit surface plasmon band at 520 nm [7]. By changing the shape and size of gold nanoparticles this band can be tuned into tissue transparent NIR region [9]. Recent success in wet-chemistry has allowed significant progress in the synthesis of non-spherical gold nanoparticles [10, 11]. Out of various non-spherical gold nanoparticles (like, triangles, stars, cube, rods, plates, branched etc.) gold nanorods (GNRs) and gold nanoplates (GNPs) are of particular interests to material

chemist due to their ease of synthesis, unique optical properties that could be tuned to NIR region by carefully controlling the reaction parameters [12-14].

Research activities and number of publications on synthesis of anisotropic gold nanostructures have increased dramatically since 2001 when a simple solution synthesis was developed yielding GNRs with aspect ratios between 1.5 and 5 [15]. The position of LSPR band depends on the aspect ratio of GNRs and hence control of LSPR band position which is essential for biomedical applications of GNRs assumes a special significance in the synthesis of GNRs and GNPs [15-18].

Another important aspect of these gold nanoparticles viz-z-viz their biomedical applications is their shelf-life [19]. One of the major limitations of gold nanoparticles is their poor colloidal stability and limited shelf-life. The cytotoxicity of nanoparticles also assumes special significance, especially when they are designed for *in-vivo* biomedical use [20]. In this chapter, existing literature on various aspects of synthesis of GNRs and GNPs have been summarized. It also covers the literature related to the studies on colloidal stability and shelf-life of GNRs. In the last section, the literature on biocompatibility and cytotoxicity of GNRs and GNPs has been reviewed.

2.2 SYNTHESIS OF GOLD NANORODS (GNRs)

This section reviews literature on the prevailing synthesis processes for GNRs. This review covers all the synthesis techniques from the electrochemical synthesis introduced by Wang et al. in 1997 [21] to seed-mediated synthesis introduced by Jana and Murphy in 2001[15] to seedless synthesis introduced by Min Gu et al. in 2006 [22]. Further developments in Jana and Min Gu's methodologies have resulted into the improvement on size and shape control.

Wang et al. in 1997 [21] have used electrochemical route for the synthesis of GNRs in reverse micelles. In this method, ionic surfactant acts as both the supporting electrolyte and the main constituent for the micellar framework. However its complex chemistry limits its utility and the method was not explained further. Martin and co-workers in 1998 [23] introduced template method for the synthesis of GNRs. In this method gold is deposited electrochemically within the pores of the nonporous polycarbonate and alumina template membranes. The widths of the GNRs depend upon the pore diameter of the membrane template and length is varied by the amount of Au deposited within the pores of membrane.

Thus aspect ratio of GNRs can be tuned. This method is time consuming and cumbersome as template needs to be replaced for the synthesis of different aspect ratio GNRs.

Jana and Murphy in 2001[15] reported size-controlled synthesis of GNRs. They have used small spherical citrate-capped gold nanospheres as seeds. GNRs were grown separately in cetyletrimethylammonium bromide (CTAB) surfactant micelles that act as templates for directional growth. Rod-like gold nanoparticles with aspect ratios 1-5 were prepared. The same group has also introduced three-step seeded protocol for the synthesis of GNRs with aspect ratio >7 [24]. The drawback of this method is it produces large fraction of gold nanospheres, which requires time-consuming centrifugation steps to separate them from rods. Yield of GNRs by this method is also quite low (4%) [24] In 2003, Murphy had reported an improved methodology that produces GNRs with high aspect ratio, with improved yield (90%) [25]. It was achieved by changing the pH of the growth solution from 2.8 to 5.6, which resulted in the large aspect ratio of GNRs. The major limitation of this method is polydispersity of GNRs also increases rapidly with the increase in the aspect ratio of GNRs.

Yang et al. in 2002 [26] have synthesized GNRs with controllable aspect ratio by using photochemistry in the presence of silver ions. The presence of silver ions improves the yield and increases the aspect ratio of GNRs. However, control on UV-irradiations play an important role in fabricating GNRs for a given silver ion concentration. Exposure to an UV-irradiation for an excess period shortens the rod length.

Nikoobhakat and El-Sayed in 2003 [27] replaced sodium citrate coated seeds with CTAB coated seeds in Jana's seed mediated method and utilized silver ions to control the aspect ratio of GNRs. Silver nitrate is added to the growth solution before seed addition to facilitate the rod formation and to tune the aspect ratio of GNRs. This method produces small aspect ratio (1.5-4.5) GNRs with reasonable yield. Murphy et al. in 2004 [28] have evaluated the effect of seed size and its surface charge on the size and shape of GNRs. Negatively charged citrate-capped seeds and positively charged CTAB-capped seeds in the size range of 3 to 18 nm were used to grow GNRs. Decrease in the aspect ratio of GNRs was observed on with the increase in the seed size irrespective of surface charge of seeds along with formation of triangles and hexagons. In another study Murphy et al. [29] have observed that with increase in seed concentration at constant concentration of Au (III) ions the length of GNRs

decreased. Synthesized GNRs have low aspect ratio with formation of spherical nanoparticles as byproduct. To verify the feasibility of use of other metals as seeds, Xu et al. have prepared GNRs with Ag seeds [30]. A shape transformation from rod to sphere was observed as the seed concentration is increased beyond 25 µL. Effect of seed aging on the shape and size of GNRs was firstly studied by Pileni et al. [31]. It was concluded that pseudo-spherical Au seeds are unstable and grows to spherical nanoparticles with aging owing to Ostwald repining. 2 h aged seeds results in the formation of well-defined GNRs with high yields (~90 %). No GNRs were formed if seeds were aged beyond 30 days. Effect of seed reaction temperature was also evaluated by Huber et al., [32] in which gold seeds were grown at 28°C, 37°C, and 40°C. Higher temperature during seeding increases the concentration of gold ions due to enhanced reduction reaction yielding spherical nanoparticles with large size. When these seeds were used for GNRs synthesis, the yield was low.

Min Gu et al. in 2006 [22] proposed the high temperature seedless synthesis of GNRs by increasing the temperature of the reaction solution to 97 °C. In this method nucleation and growth proceed simultaneously. $NaBH_4$ acts as a reducing agent in the absence of seed in order to enhance the reduction of Au^+ to Au^0. The growth rate of GNRs increases by 3 orders of magnitude when the temperature is raised above room temperature. Decrease in nanorod length was observed with increase in the temperature, while no change was observed in GNRs width. El-Sayed et al. [33] have also introduced seedless approach for the synthesis of small GNRs. They have studied the role of silver ions, pH and $NaBH_4$ in the seedless synthesis of GNRs. pH plays the vital role and controls the polydispersity of the GNRs. GNRs with LSPR band upto 800 nm could be obtained with this improved method.

Yi et al. in 2007 [34] added hydroxylamine to improve the yield of GNRs. Their results show an increase in the yield by varying the reaction temperature and hydroxylamine concentration. Aspect ratio up to 17 was obtained at 0 ºC which decreased to 4.5 when temperature was increased to 20 ºC. The process lags in its feasibility due to low temperatures involved. Large number of spherical and triangular plates also formed along with GNRs.

Huang et al. in 2007 [35] have reported synthesis of monodispersed GNRs with addition of nitric acid in the growth solution in three-step seed-mediated synthesis. Nitric

acid addition substantially reduced the formation of gold nano triangles and increase the aspect ratio of GNRs. Tiwari et al. [36] has used KOH to adjust the pH of the growth solution. Reducing ability of ascorbic acid decreased with decreasing pH. With increase in KOH, LSPR band of synthesized nanoparticles undergo a blue shift. A similar study was also conducted by Hong et al. [37] by using sodium hydroxide. They have observed that the presence of nitrate ions reduce the formation of spherical and triangular shaped nanoplates. Aspect ratio of GNRs decreases with the increase in the pH of the growth solution.

Role of halide ions in the GNRs' formation was studied by Liz-Marzan et al. and Zheng et al. Liz-Marzan et al. [38] studied the effect of iodide ions on the morphological and optical properties in GNRs. LSPR band shifts by 250 nm with change in iodide ions concentration. Iodine addition into to the growth solution changes the shape of the nanoparticles form rod to dumbbell-like structure. Role of bromide ions on the formation of GNRs was also studied by Zheng et al. in 2013[39]. They have concluded that GNRs with tunable LSPR bands up to 850 nm can be prepared by using bromide-free binary surfactant mixture composed of alkyltrimethylammonium chloride and NaOL.

2.3 SYNTHESIS OF GOLD NANOPLATES (GNPs)

Very few methods have been developed for the synthesis of GNPs. This section of reviews the prevailing literatures on the methods for the synthesis of GNPs. GNPs were either prepared by biological routes or by polyamine process. Dong et al. in 2004 [40] described L-amino acid-based one-pot synthesis of gold nanostructures. They have synthesized single crystal GNPs with thickness less than 30 nm. Among natural L-amino acids, aspartate shows a very distinct capability of shape control to produce GNPs. Asparate reduction of gold chloride forms hexagonal and truncated triangular shaped GNPs.

Yun et al. in 2005 [41] reported synthesis of size-controlled GNPs by reduction of auric acid with sodium citrate, in the presence of PVP. Synthesized GNPs were single crystals with planar width of 80-500 nm and thickness of 10-40 nm, exhibiting strong SPR in the NIR region. Although this method produced GNPs with SPR tunable deep into NIR region, the relatively larger dimensions of GNPs limits their utility in biomedical applications.

Huang et al. in 2005 [42] prepared three different size ranges of triangular and hexagonal GNPs by the thermal reduction of $HAuCl_4$ with trisodium citrate in the presence of CTAB. GNPs with width upto few microns are prepared by changing the reaction temperature. They propose that CTAB:$HAuCl_4$ ratio of 6 forms well-defined GNPs. Ning Gu et al. in 2006 [43] synthesized single-crystalline, regular-edged GNPs through chemical reduction of $HAuCl_4$ by a suitable amount of citrate at room temperature, without additional capping agents or surfactants. Hexagonal GNPs with few triangular GNPs were formed at suitable sodium citrate:$HAuCl_4$ molar ratio accompanied by low reaction temperature. But the yield of GNPs was quite low.

Wang et al. in 2005 [44] have synthesized single-crystalline GNPs by polyol process. GNPs were produced by heating a concentrated aqueous solution of polyethylenimine and $HAuCl_4$ at 100 °C. GNPs in the size range of 40 µm were produced which is not use full for biomedical applications like hyperthermia. Wang et al. in 2007 [45] prepared single-crystalline GNPs using $HAuCl_4$ and serum albumin protein (BSA) at room temperature. BSA acts as reducing and shape directing agent leading to the anisotropic growth of Au (0) into plate-like structures. GNPs in a size range of few nanometers to 100 µm were prepared with broad size distribution.

Lee et al. in 2009 [46] synthesized GNPs (icosahedra) by heating an aqueous solution of amphiphilic block copolymer, pluronic-123, $HAuCl_4$ and sodium chloride at 60 °C. GNPs were accompanied by large fraction of irregular shaped icosahedral nanoparticles which are extremely difficult to isolate from GNRs.

Shi et al. in 2010 [47] modified polyol process using binary surfactant system. They prepared hexagonal, triangular and truncated triangular GNPs in the size range from few nanometers to tens of micrometer by thermal reduction of $HAuCl_4$ in a binary surfactant mixture of Poly(vinylpyrrolidone) (PVP) and CTAB in the presence of ethylene glycol. GNPs yield is high but size limits its applicability again in optical hyperthermia due to very broad size distribution.

Park et al. in 2014 [48] synthesized hexagonal, triangular, spherical and rod shaped nanoparticles by carefully controlling the reaction kinetics using iodide ions. They demonstrated that GNRs formed in the absence of iodide ions. In the presence of iodide ions

spherical nanoparticles, triangular and hexagonal plates have been formed. Control over morphology of nanoparticles is quite poor and secondary methods are required for isolation of nanoparticles with various shapes.

Zhang et al. in 2014 [49] introduced the seedless synthesis of triangular GNPs with high morphological yield (>90%). They have demonstrated that iodide ions might have dual functionality in the formation of GNPs. It selectively binds to the Au {111} facets and remove other less stable shape through oxidative etching by forming tri-iodide ions (I^{3-}), thus facilitating the formation of nuclei with dominant planar structure.

Ni et al. in 2016 have [50] demonstrated reproducible production of micron sized single crystalline GNPs via seedless synthesis at 85 ºC. GNPs formed here were polydisperse with a broad SPR band centered at 520 nm to 1000 nm.

2.4 TUNABILITY OF GNRs AND GNPs

El-Sayed et al. in 2003 [27] introduced binary-surfactant system of CTAB and benzyledimethylhexadecylammonium bromide (BDAC) to increase the aspect ratio GNRs. GNRs with aspect ratio upto 10 and LSPR band tunable upto 1100 nm was successfully synthesized by varying the Ag^{+} ions and successive addition of secondary growth solution to the as-synthesized GNRs. This method is quite time consuming as it requires successive additions of secondary growth solution to increase the aspect ratio GNRs. The polydispersity of GNRs was also high.

Mosquera et al. in 2008 [51] synthesized GNPs using amphiphilic polyethylene oxide-polystyrene oxide block copolymers as both reductant and stabilizing agents. Varying the copolymer concentration and reaction temperature allows the tuning of surface plasmon band of GNPs from 850 nm to 1100 nm.

Effect of pH on the tunability of GNRs' aspect ratio was studied by several groups. Murray et al. in 2012 [52] have tuned the LSPR band of GNRs from 627 to 1246 nm by using aromatic additives and reducing the concentration of CTAB surfactant to ~0.05 M as opposed to 0.1 M in seed-mediated protocols. Huang et al. in 2013 [53] have reported a systematic approach for the synthesis of ultralong GNRs and nanowires by using seed-mediated method. They have investigated the effect of pH of the growth solution on the

dimensions of nanorods. GNRs and nanowires with average lengths from 580 to 2850 nm were prepared.

Tracy et al. in 2013 [54] discuss the role of continuous addition of ascorbic acid to the stirring solution of GNRs. Slow addition of AA during the secondary growth provides improved control over the AR and size of GNRs. Their results indicate that LSPR band can be tuned between 700 and 880 nm during secondary growth by adjusting the rate of AA addition. Zubarev et al. in 2013 [55] have used hydroquinone in place of AA to tune LSPR band of GNRs in seed-mediated synthesis. LSPR bands of GNRs can be tuned up to 1230 nm with high degree of purity and reliability by using hydroquinone. These GNRs could not be used in medical applications due to high toxicity of hydroquinone. Liang et al. in 2014 [56] synthesized GNRs with a LSPR band larger than 1400 nm by seedless growth method. They have replaced AA with weaker reducing agent, paraoxydibenzene. Paradioxybenzene helps in increasing the aspect ratio and yield of GNRs. Tremiliosi-Filho et al. in 2015 [57] have tuned the LSPR band of GNRs from 620 to 1200 nm by varying the reaction conditions by seedless method by using glycerol as reducing agents. The aspect ratio and yield of GNRs is dependent on the pH and temperature of the reactants. High aspect ratio GNRs were prepared when pH was less than11.

Murray et al. in 2013 [58] have reported the synthesis of thin (width <25 nm), thickness (>30 nm) GNRs with tunable LSPR band by using seeded growth at reduced CTAB concentrations (0.037 M). The CTAB−NaOL binary surfactant system overcomes the difficulty of thickening of GNRs often associated with single-component CTAB based system. Khlebtsov et al. in 2014 [59] have introduced controlled overgrowth of GNRs in binary surfactant system of NaOL-CTAB. By controlling the GNRs as seeds to the molar ratio of gold in the growth solution it is possible to tune the length and LSPR band of overgrown nanoparticles in wide range.

Gobin et al. in 2012 [60] have tuned the SPR band of GNPs in single-step reaction of $HAuCl_4$ and $Na_2S_2O_3$. They have demonstrated that their plasmon resonance bands are is controllable with increasing molar ratios of $HAuCl_4/Na_2S_2O_3$. Zhau et al in 2015 [61] have tuned plasmon resonance bands of GNPs by oxidative etching of gold by O_3 gas. By controlling the experimental parameters like concentration of O_3, exposure duration,

concentration of CTAB in suspensions and the reaction temperature, GNPs with plasmon bands tunable from 790 nm to 1004 nm can be synthesized.

2.5 STABILITY OF GNRs and GNPs

Anisotropic gold nanoparticles undergo shape deformation, which results into decrease in their aspect ratio. SPR band corresponding to the longer wavelength shifts towards shorter wavelength. For biomedical applications, gold nanoparticles need to be stabilized against aggregation and shape deformation of the nanoparticles [62]. This section reviews literature which is focused at enhancement of shelf-life and colloidal stability of GNRs and GNPs.

Tae et al. in 2007 [63] have used binary surfactant system consisting of CTAB and Pluronic F-127 for the synthesis of stable GNRs. This binary surfactant system limits the blue-shift of the plasmon resonance bands of GNRs when stored. Hafner et al. in 2009 [64] have studied the effect of CTAB surfactant on the stability of GNRs. The ratio of CTAB to nanorod concentration is a critical parameter to maintain the stability of GNRs. Murphy et al. in 2010 [65] have synthesized GNRs by using seed-mediated approach with CTAB. The CTAB bilayers were exchanged with 11-(acryloyloxy) undecyltrimethyl ammonium bromide (p-CTAB). They have observed improvement in the stability of GNRs after ligand exchange.

Yang et al. in 2010 [66] investigated the stability of the GNRs in aqueous medium. They have found that LSPR band of the GNRs gradually shifts to shorter wavelength due to decrease in their aspect ratios. They have demonstrated that this shape deformation can be inhibited by reducing the concentration of CTAB or coating them with poly(sodium styrenesulfonate).

Hamad-Schifferli et al. in 2012 [67] have investigated the stability of GNRs coated with amphiphilic ligands. An aggregation index based on the LSPR peak broadening was used to measure the stability of the GNRs as a function of the number of washes, pH, ionic concentration and temperature. The aggregation index was also used to measure the stability of the GNRs under ultrafast laser irradiation and in the presence of proteins commonly used in cell culture. Difference in GNRs stability has been observed, which may be due to differences in the physical and chemical properties of the amphiphilic ligands.

Tebbe et al. in 2015 [68] investigated the stability of GNRs by ligand exchange of CTAB with bovine serum albumin (BSA). BSA-coated GNRs have improved colloidal stability. Haider et al. in 2016 [69] have encapsulated GNRs with mesoporous silica shell to improve their colloidal stability. These GNRs were stable in water for more than 5 months.

2.6 BIOCOMPATIBILITY OF GNRs AND GNPs

Evolution of biocompatibility of gold nanoparticles is essential before they are being used for biomedical applications. Various research groups have investigated the cytotoxicity of gold nanoparticles [70-73]. Toxicity of gold nanoparticles depends on the size, shape, and surface chemistry of nanoparticles.

Takahashi et al. 2006 [70], have improved the biocompatibility of GNRs by replacing CTAB from the surface of GNRs with biocompatible monomers like PEG or phospholipids. Takahashi et al. extracted the CTAB from aqueous solution of GNRs using a chloroform phase that contained phosphatidylcholine. This surface ligand replacement did not induce particle aggregation but did enhance the biocompatibility of the GNRs as compared to CTAB-capped nanoparticles.

Niidome et al. in 2006 [71] developed a technique to modify toxic CTAB capped GNRs with polyethyleneglycol (PEG). PEG-modification was achieved by adding mPEG-SH in the CTAB solution and excess CTAB was removed by dialysis. PEG-modified GNRs have neutral surface and little cytotoxicity *in-vitro*.

Chen et al. in 2006 [72] investigated the cytotoxicity of surface functionalized GNRs by MTT assays on the fibroblast and HeLa cell lines. They found that surface functionalized GNRs are readily internalized by these cells. Polarity on the surface of GNRs strongly affects the biocompatibility of GNRs. The positive amino group on the surface of nanorod was less cytotoxic as compared to negatively charged carboxylic acid group capped GNRs.

Chandra Ray et al. in 2008 [73] have reported the cytotoxicity of gold nanoparticles of various sizes and shapes using MTT assays. They have demonstrated that spherical gold nanoparticles are less toxic as compared to GNRs. This might be due to the difference in the coating of these two nanostructures. Kong et al. in 2008 [74] have evaluated toxicity of the GNRs coated with CTAB and polyethylene glycol (PEG). They have concluded that CTAB

capped GNRs were more toxic as compared to PEG-coated GNRs even at low concentration (0.5 nM). This might be because of presence CTAB residues in the solution. Hauck et al. in 2008 [75] have reported coating of CTAB stabilized capped GNRs with polyelectrolyte. This secondary coating significantly reduce the toxicity of GNRs by hindering desorption of CTAB from the surface of nanorods. In a similar study, Alkilany and Murphy [76] have presented desorption of CTAB from the surface of GNRs by free radical polymerization and thus improve the biocompatibility of GNRs.

Leeuwen et al. in 2010 [77] evaluated cellular response of polystyrene sulfonate (PSS) or polyethylene glycol (PEG) treated GNRs. Mitochondrial activity of GNRs on mouse myoblast (C2C12) and Human Leukemia (HL60) cell lines were evaluated using MTS assay. They found that PEGylated-GNRs have better biocompatibility as compared to PSS-coated-GNRs, which show considerable cytotoxicity. Electron microscopy displayed no cellular uptake of PEGylated-GNRs compared to their PSS counterparts.

Chen et al. in 2012 [78] have investigated the cytotoxicity of GNRs on human HEp-2 and canine MDCK cells. Effect of encapsulation, charge on nanorod's surface, their size and shape on the toxicity of GNRs were evaluated. CTAB-encapsulated GNRs have higher toxicity as compared to GNRs coated with polymers and citrate stabilized gold nanospheres. They also pointed out that the toxicity of CTAB-encapsulated GNRs was due to the CTAB which was on the surface of GNRs and was not due to free CTAB in the solution. Both positive and negative charges on the surface of polymer-coated GNRs have shown similar levels of cytotoxicity. They also could not find any correlation between cytotoxicity of GNRs and their aspect ratios.

Chen et al. in 2013[79] have examined the effect of surface chemistry on the interaction of GNRs and cell membranes and the toxicity arising from them in a serum-free cell culture system. They have observed that polyelectrolyte-coated GNRs have better biocompatibity than CTAB-capped GNRs. They have concluded that the nature of surface molecules, especially their packing structure on the surface of GNRs rather than the surface charge plays a vital role in determining the cytotoxicity of nanostructures.

In this study Wang et al. in 2014 [80] have evaluated cellular uptake and cytotoxicity of GNRs with various surface coatings, including organic CTAB, poly(sodium 4-

styrenesulfonate) (PSS), and poly(ethylene glycol) (PEG), and inorganic mesoporous silica ($mSiO_2$), dense silica ($dSiO_2$) and titanium dioxide (TiO_2). CTAB, PSS, and $mSiO_2$ coated GNRs exhibit notable cytotoxicity, while PEG, $dSiO_2$, and TiO_2 coated GNRs do not induce cell injury. $mSiO_2$, $dSiO_2$, and TiO_2 coated GNRs show significantly higher cellular uptake than the PSS and PEG coated GNRs.

Gooding et al. in 2015 [81] developed one-step surface functionalization method that involves the use of Tween 20 to stabilize GNRs, bis(p-sulfonatophenyl)phenylphosphine (BSPP) to activate the GNR surface for the subsequent PEGylation, and NaCl to etch silver from the GNRs. This method allows complete removal of the surface bound CTAB and active surface silver from the GNRs. These GNRs have significantly lower toxicity as compared to PEGylate GNRs.

Li et al. in 2015 [82] have investigated effect of aspect ratio and surface functionalization of GNRs on their cytotoxicity. Surface modification of CTAB-coated GNRs with polystyrene sulfonate (PSS), polyallylamine hydrochloride (PAH), or both (PSS/PAH) dramatically decreases toxicity of GNRs. CTAB-GNRs with various aspect ratios had similar abilities to induce cell apoptosis. GNRs coated with CTAB/PSS, CTAB/PAH, CTAB/PSS/PAH or CTAB/PAH/PSS displayed lower toxicity and did not induce cell death.

From the literature surveys following gaps in the study have been identified:

Gaps in the Study:

1. GNRs and GNPs with desired optical properties can be prepared either through template synthesis or polyol processes. However, the yield of GNRs and GNPs obtained via these methods is very low. Apart from this, they are costly and involve complex chemistry. To overcome these drawbacks seed mediated synthesis of GNRs was proposed in 2001 followed by seedless synthesis in 2005. Using these techniques good quality GNRs with tunable optical properties have been prepared by many researchers. Most of these reports are confined to GNRs synthesis having SPR in visible region. Limited work has been carried out towards tunability of SPR bands of GNRs and GNPs in NIR region by seed-mediated and seedless methods.

2. GNRs and GNPs prepared by seed-mediated and seedless synthesis show degradation in their optical response over a period of time. Hence, shelf- life of these gold nanostructures is a major concern. Apart from this, the exact mechanism responsible for the decay of plasmonic properties is not known. Very little efforts have been made to enhance the stability of GNRs and GNPs prepared via wet chemical synthesis.
3. For *in-vivo* biomedical applications, biocompatible gold nanoparticles are essential. However limited efforts have been devoted towards the evolution of toxicity of GNRs and GNPs, both *in-vivo* and *in-vitro*. How to improve biocompatibility of these gold nanostructures prepared via seed-mediated and seedless synthesis is a major challenge and need of the day to devise successful plasmonic photothermal therapy using these gold nanostructures.

Based on these gaps, following objectives have been proposed for the doctoral thesis:

Objectives:

1. Synthesis of NIR responsive gold nanostructures with tunable aspect ratio.
2. Investigations of as-synthesized gold nanostructures by UV-visible and photon correlation spectroscopy, transmission electron microscopy, etc.
3. Investigation of the stability of biocompatible gold nanostructures and development of synthesis protocols to enhance the shelf life of gold nanostructures.

References:

1. S.P. Fricke, *Gold Bull.*, **1996**, 29, 2, 53-60.
2. M. Faraday, *Phil. Trans. R. Soc. Lond*., **1857**, 147, 145-181.
3. C.W. Bodemer, *Northwest Med*., **1972**, 71, 12, 888.
4. S. Eustisa, M.A. El-Sayed, *Chem. Soc. Rev*., **2006**, 35, 209-217.
5. B.V. Enustun, J. Turkevich, *J. Am. Chem. Soc*., **1963**, 85, 3317–3328.
6. G. Frens, *Nature*, **1973**, 241, 20-22.
7. A. Henglein, M. Giersig, *J. Phys. Chem. B*, **1999**, 103, 9533–9539.
8. S. Link, M.A. El-Sayed, *J. Phys. Chem. B*, **1999**, 103, 4212–4217.
9. M.B. Mohamed, K.Z. Ismail, S. Link, M.A. El-Sayed, *J. Phys. Chem. B*, **1998**, 102, 9370–9374.
10. Z. Liu, Z. Shen, T. Zhu, S. Hou, L. Ying, *Langmuir*, **2000**, 16, 3569–3573.
11. M.H. Magnusson, K. Deppert, J.O. Malm, J.O. Bovin, L. Samuelson, *J. Nanopart. Res.*, **1999**, 1, 243–251.
12. J.L. Westa, N.J. Halas, *Curr. Opin. Biotechnol*., **2000**, 11, 215-217.
13. R.A. Sperling, P.R. Gil, F. Zhang, M. Zanellaa, W.J. Parak, *Chem. Soc. Rev*., **2008**, 37, 9, 1896-1908.
14. W. Cai, T. Gao, H. Hong, J. Sun, *Nanotechnol. Sci. Appl*., **2008**, 1, 17–32.
15. N.R. Jana, L.A. Gearheart, C.J. Murphy, *Adv. Mater*., **2001**, 13, 1389-1393.
16. X. Huang X, P.K. Jain, I.H. El-Sayed, M.A. El-Sayed, *Nanomedicine (Lond)*, **2007**, 2, 681-93.
17. D. Khang, J. Carpenter, Y.W. Chun, R. Pareta, T.J. Webster, *Biomed Microdevices*, **2010**, 12, 575-587.
18. M. Tsuji, M. Hashimoto, Y. Nishizawa, T. Tsuji, *Chemistry Letters*, **2003**, 32, 1114-1115.
19. M.K. Chow, C. Zukoski, *J. Colloid Interface Sci.*, **1994**, 165, 97-109.
20. A.M. Alkilany, C.J. Murphy, *J. Nanopart. Res.*, **2010**, 12, 2313–2333.
21. Y. Ying, S.S. Chang , C.L. Lee, C.R.C. Wang, *J. Phys. Chem. B*, **1997**, 101, 6661–6664.
22. P. Zijlstra, C. Bullen, J.W.M. Chon, M. Gu, *J. Phys. Chem. B*, **2006**, 110, 19315–19318.
23. V.M. Cepak, C.R. Martin, *J. Phys. Chem. B*, **1998**, 102, 9985–9990.
24. N.R. Jana, L. Gearheart, C.J. Murphy, *J. Phys. Chem. B*, **2001**, 105, 4065-4037.
25. B.D. Busbee, S.O. Obare, C.J. Murphy**,** *Adv. Mater.*, **2003**, 15, 414-416.
26. F. Kim, J. He, Song, P. Yang, *J. Am. Chem. Soc*., **2002**, 124, 14316–14317.
27. B. Nikoobakht, M.A. El-Sayed, *Chem. Mater*., **2003**, 15, 1957-1962.
28. A. Gole, C.J. Murphy, *Chem. Mater*., **2004**, 16, 3633–3640.
29. T.K. Sau, C.J. Murphy, *Langmuir*, **2004**, 20, 6414-6420.
30. Z.C. Xu, C.M. Shen, C.W. Xiao, et al., *Nanotechnology*, **2007**, 18, 115608- 115612.
31. X.C. Jiang, M.P. Pileni, *Colloids Surf. A Physicochem. Eng. Asp.*, **2007**, 295, 228-232.
32. J. Watt, B.G. Hance, R.S. Anderson, D.L. Huber, *Chem. Mater*., **2015**, 27, 6442–6449.
33. M.R.K. Ali, B. Snyder, M.A. El-Sayed, *Langmuir*, **2012**, 28, 9807–9815.
34. S.K. Kang, Y. Kim, M.S. Hahn, I. Choi, J. Lee., J. Yi, *Curr. Appl. Phys.*, **2006**, 6, 114-120.
35. H.Y. Wu, W.L. Huang, M.H. Huang, *Cryst. Growth Des.*, **2007**, 7, 831–835.

36. N. Tiwari, S. Kalele, S.K. Kulkarni, *Plasmonics*, **2007**, 2, 231–236.
37. W.M. Park, Y.S. Huh, W.H. Hong, *Curr. Appl. Phys*., **2009**, 9, 140-143.
38. M. Grzelczak, A.S. Iglesias, B.R. González, R.A. Puebla, J.P. Juste, L.M. Liz-Marzán, *Adv. Funct. Mater*., **2008**, 18, 3780–3786.
39. X. Ye, Y. Gao, J. Chen, D.C. Reifsnyder, C. Zheng, C.B. Murray, *Nano Lett*., **2013**, 13, 2163–2171.
40. Y. Shao, Y. Jin, S. Dong, *Chem. Commun*., **2004,** 0, 1104-1105.
41. C.S. Ah, Y.J. Yun, H. J. Park, W.J. Kim, D. H. Ha, W.S. Yun, *Chem. Mater*., **2005**, 17, 5558–5561.
42. H.C. Chu, C.H. Kuo, M.H. Huang, *Inorg. Chem*., **2006**, 45, 808–813.
43. L. Huang, Z.R. Guo, M. Wang, N. Gu, *Chin. Chem. Lett.*, **2006**, 17, 1405-1408.
44. X. Sun, S. Dong, E. Wang, *Langmuir*, **2005**, 21, 4710–4712.
45. J. Xie, J.Y. Lee, D. I.C. Wang, J. *Phys. Chem. C*, **2007**, 111, 10226–10232.
46. J. Xie, J.Y. Lee, D.I. Wang, Y.P. Ting, *Small*, **2007**, 3, 672-82.
47. C. Wang, C. Kan, J. Zhu, X. Zeng, X. Wang, H. Li, D. Shi, *J. Nanomater*., **2010**, 2010, 969030, 1-9.
48. S. Hong, Acapulco, A.I. Jesus, S. Akshay et al., *Bull. Korean Chem. Soc*., **2014**, 35, 1737-1742.
49. L. Chen, F. Ji, Y. Xu, L. He, Y. Mi, F. Bao, B. Sun, X. Zhang, Q. Zhang, *Nano Lett*., **2014**, 14, 7201–7206.
50. S. Chen, P.X. Yue, L. Junfei, X. Song, H. Weihui, O. Li, L.W. Ni, *Nano Micro Lett.*, **2016**, 8, 328–335.
51. S.G. López, E. Castro, P. Taboada, V. Mosquera, *Langmuir*, **2008**, 24, 13186–13196.
52. X. Ye, L. Jin, H. Caglayan, J. Chen, G. Xing, C. Zheng, V.D.-Nguyen, Y. Kang, N. Engheta, C.R. Kagan, C.B. Murray, *ACS Nano*, **2012**, 6, 2804–2817.
53. Y.N. Wang, W.T. Wei, C.W. Yang, M.H. Huang, *Langmuir*, **2013**, 29, 10491–10497.
54. K.A. Kozek, K.M. Kozek, W.-C. Wu, S.R. Mishra, J.B. Tracy, *Chem. Mater*., **2013**, 25, 4537–4544.
55. L. Vigderman, E.R. Zubarev, *Chem. Mater*., **2013**, 25, 1450–1457.
56. X. Xu, Y. Zhao, X. Xue, S. Huo, F. Chen, G. Zou, X.J. Liang, *J. Mater. Chem. A*, **2014**, 2, 3528-3535.
57. R. Parveen, J.F. Gomes, S. Ullah, J.J.S. Acuña, G. Tremiliosi-Filho, *J. Nanopart. Res*., **2015**, 17, 418.
58. X. Ye, C. Zheng, J. Chen, Y. Gao, C.B. Murray, *Nano Lett*., **2013**, 13, 765–771.
59. B.N. Khlebtsov, V.A. Khanadeev, J. Ye, G.B. Sukhorukov, N.G. Khlebtsov, *Langmuir*, **2014**, 30, 1696–1703.
60. G. Zhang, J.B. Jasinski, J.L. Howell, D. Patel, D.P. Stephens, A.M Gobin et al. *Nanoscale Res. Lett*., **2012**, 7, 337.
61. X. Jiang, R. Liu, P. Tang, W. Li, H. Zhong, Z. Zhou, J. Zhou, *RSC Adv*., **2015**, 5, 80709-80718.

62. K.T. James, M.G. O'Toole, D.N. Patel, G. Zhang, A.M. Gobin, R.S. Keynton, *RSC Adv.*, **2015**, 5, 12498-12505.
63. M. Iqbal, Y. Chung, G. Tae, *J. Mater. Chem*., **2007**, 17, 335-342.
64. B.C. Rostro-Kohanloo, L.R. Bickford, C.M. Payne, E.S. Day, L.J. Anderson, M. Zhong, S. Lee, K.M. Mayer, T. Zal, L. Adam, C.P. Dinney, R.A. Drezek, J.L. West, J.H. Hafner, *Nanotechnology*, **2009**, 28, 434005.
65. A.M. Alkilany, P.K. Nagaria, M.D. Wyatt, C. J. Murphy, *Langmuir*, **2010**, 26, 12, 9328–9333.
66. R. Zou, Q. Zhang, Q. Zhao, F. Peng, H. Wang, H. Yu, J. Yang, *Colloids Surf A Physicochem Eng Asp*., **2010**, 372, 177-181.
67. J.C.Y. Kah, A. Zubieta, R.A. Saavedra, K. Hamad-Schifferli, *Langmuir*, **2012**, 28, 8834–8844.
68. M. Tebbe, C. Kuttner, M. Männel, A. Fery, M. Chanana, *ACS Appl. Mater. Interfaces*, **2015**, 7, 5984–5991.
69. I. Haidar, G. Lévi, L. Mouton, J. Aubard, J. Grand, S. Lau-Truong, D.R. Neuville, N. Félidj, L. Boubekeur-Lecaque, *Phys. Chem. Chem. Phys*., **2016**, 30, 32272-32280.
70. H. Takahashi, Y. Niidome, T. Niidome, K. Kaneko, H. Kawasaki, S. Yamada, *Langmuir*, **2006**, 22, 2–5.
71. T. Niidome, M. Yamagata, Y. Okamoto, Y. Akiyama, H. Takahashi, T. Kawano, Y. Katayama, Y. Niidome, *J. Control. Release*, **2006**, 114, 343–347.
72. C.W. Kuo, J.J. Lai Lai, P. Chen, *MRS Online Proceedings Library*, **2006**, 951, 0951-E12-25.
73. S. Wang, W. Lu, O. Tovmachenko, U. S. Rai, H. Yu, P. C. Ray, *Chem. Phys. Lett.* **2008,** 463, 145–149.
74. I.P. Lau, H. Chen, J. Wang, H.C. Ong, K.C. Leung, H.P. Ho, S.K. Kong, *Nanotoxicology*, **2012,** 6, 847-56.
75. T.S. Hauck, A.A. Ghazani, W.C.W. Chan, *Small*, **2008**, 4, 153–159.
76. A.M. Alkilany, C.J. Murphy, *Langmuir*, **2009**, 25, 13874–13879.
77. R.G. Rayavarapu, W. Petersen, L. Hartsuiker, P. Chin, H. Janssen, F.W. Leeuwen, C. Otto, S. Manohar, T.G. Leeuwen, *Nanotechnology*, **2010**, 9, 145101.
78. Y. Zhang, D. Xu, W. Li, J. Yu, Y. Chen, *J. Nanomater*., **2012**, 375496, 1-7.
79. L. Wang, X. Jiang, Y. Ji, R. Bai, Y. Zhao, X. Wu, C. Chen, *Nanoscale*, **2013**, 5, 8384-91.
80. X.M. Zhu, C. Fang, H. Jia, Y. Huang, C.H. Cheng, C.H. Ko, Z. Chen, J. Wang, Y.X. Wang, *Nanoscale*, **2014**, 6, 11462-72.
81. K. Liu, Y. Zheng, X. Lu, T. Tha, N. A. Lee, U. Bach, J.J. Gooding, *Langmuir*, **2015**, 31, 4973–4980.
82. J. Wan, J. H. Wang, T. Liu, Z. Xie, X.-F. Yu, W. Lia, *Sci Rep*., **2015**, 5, 11398.

CHAPTER 3

SYNTHESIS AND CHARACTERIZATIONS OF GOLD NANOSTRUCTURES

3.1 INTRODUCTION

Development of consistent protocols for synthesis of materials at nanoscale is an important aspect of nanotechnology. Through careful control of experimental parameters, different nanoparticle shapes can be prepared. Use of anisotropic gold nanoparticles in biomedical imaging and therapy applications have renowned interest in size and shape controlled wet-chemical synthesis of gold nanostructures [1]. The property that governs their use in these applications is the localized surface plasmon resonance [1]. This property of metal nanoparticles is tunable. It depends on the physical size, size distribution, shape and surface passivation of nanostructures [1, 2]. These features of nanomaterials can be controlled by choosing an appropriate technique for nanoparticles synthesis and optimizing reaction parameters by fine tuning synthesis variables [2]. This chapter describes development of protocols for wet-chemical synthesis of gold nanorods (GNRs) and gold nanoplates (GNPs) with desired physical, chemical, structural, optical and surface properties.

Synthesis of GNRs by seed-mediated and seedless methods in the presence of rod-directing surfactant is a promising approach to achieve moderate quality GNRs without deteriorating their physical and surface properties [2-4]. This method has an advantage of yielding GNRs with desired optical bands in the visible and near IR region [4]. In the first part of this chapter, synthesis of GNRs is carried out by seed-mediated method using cetyltrimethylammonium bromide (CTAB) as rod-directing and stabilizing surfactant [4]. It is a two-step process. In the first step, CTAB stabilized seeds are prepared by reducing $HAuCl_4$ with strong reducing agent ($NaBH_4$). In the second step, GNRs are grown in the growth medium containing reagents (CTAB, $HAuCl_4$, $AgNO_3$, ascorbic acid) and gold seeds. Effect of concentration of stabilizing cum growth directing agents and kinetic parameters like concentration of gold salt, reducing ability of reducing agent, effect of $AgNO_3$ and aging of initially prepared gold seeds on the nanorod quantity and quality is evaluated in terms of changes in the size, size distribution, aspect ratio and morphology.

Seedless synthesis of GNRs is a single-step process [5]. In this method $NaBH_4$ is directly added to the growth solution. It is believed that $NaBH_4$ addition in the growth solution results in the formation of small seeds which then acted as nucleation centers for the anisotropic growth of GNRs [5, 6]. Thus formation of seed and growth of GNRs takes place under ambient conditions simultaneously and batch to batch variation caused by the temporal instability of the seeds in seed-mediated method is avoided here. In this chapter GNRs are also prepared by the seedless approach. Effect of $NaBH_4$ on the quality and quantity of GNRs synthesized by the seedless approach has also been evaluated by utilizing the optimized growth parameters obtained from the seed-mediated synthesis of GNRs.

Apart from nanorods, other anisotropic plasmonic nanostructures are also gaining increasing interest due to size and shape control tunability of their plasmon resonance band into the NIR region [7, 8]. Amongst them, pluronic F-127 stabilized gold nanoplates (GNPs) could be potential alternatives to CTAB stabilized GNRs due to their improved biocompatibility and tunability of surface plasmon bands to the near-infrared region of the electromagnetic spectrum [9]. GNPs are largely undermined because of the difficulty in reproducible synthesis of high-quality and stable GNPs in literature. The second most important aspect dealt-with in this chapter is the development of protocols for the synthesis of plasmonic GNPs. In this study, we have designed and executed seed-mediated and seedless synthesis protocols for GNPs. CTAB is replaced with biocompatible pluronic F-127 which simultaneously acts as reducing, growth directing and stabilizing agent [10].

Freshly prepared gold nanostructures are characterized by measuring their size and size distribution with photon correlation spectroscopy (PCS), plasmonic properties by UV-Vis-NIR spectroscopy and morphological studies through Transmission Electron Microscopy (TEM). From the detailed investigation of as-synthesized nanoparticles by various characterization techniques, optimized conditions are being laid down for the synthesis of high yield, water dispersible GNRs and GNPs that are suitable as photothermal agents in plasmonic photothermal therapy.

3.2 SYNTHESIS OF GOLD NANORODS (GNRs)

3.2.1 Seed-Mediated Synthesis of GNRs

Detailed protocol followed for the synthesis of GNRs by seed-mediated method is explained in **Annexure-I** section **A1**. Pre-synthesized gold seeds (~3-4 nm) were used for the synthesis of GNRs [4]. The seeds were formed by the reduction of Au(III) with a strong reducing agent ($NaBH_4$). The reduction of Au(II) into Au(0) by $NaBH_4$ results in fast nucleation and subsequent growth leading to the formation of spherical gold seeds. These seeds are then combined with aqueous solution of Au(III) that is stabilized with excess surfactant (CTAB). Subsequently, the rod formation is facilitated by reduction of Au(III) with a weak reducing agent (ascorbic acid). GNR growth does not take place in the absence of gold seeds as seeds act as sites for nucleation [11]. CTAB forms rod shape micelles above the critical micelle concentration (~ 1.0 mM) [12]. It gets adsorbed as-bilayer on the surface of the GNRs and directs the growth by preferentially binding to the crystal faces along the length of the nanorods [13, 14].

By controlling the growth conditions in aqueous medium, it is possible to synthesize GNRs with tunable aspect ratios. $AgNO_3$ helps in regulating the growth of the nanoparticles along various crystallographic planes and role of $AgNO_3$ in the synthesis of GNRs has been well documented [2, 4]. Ascorbic acid acts as a week reducing agent and it cannot reduce gold salt if seeds are not present in the growth medium [15]. To understand the effects of reactants and kinetic variables on the size and shape of gold nanostructures, a sequential seed-mediated growth procedure was followed (**Fig. 3.1**). Detailed protocols followed for the synthesis of GNRs are documented in **Annexure-I** section **A1**.

3.2.2 Sequential Growth Process

3.2.2.1 Effect of Surfactant

The role of surfactant in GNRs growth is critical as both the size and the shape of the nano particles are controlled by surfactant type and their relative concentration viz-a-viz metal salt. The choice of CTAB as a surfactant for the preparation of GNRs in this study is inspired from the existing literature [3-5]. CTAB is known to form rod-shape micelles at suitable concentration. Because of this CTAB is widely used for the synthesis of GNRs. In literature,

it was proposed that the rod-like micelles formed by the CTAB provides soft template for the nanorod growth [4]. In recent literature many researchers have proposed that surfactant monomer adsorption on preferential facets restrict the growth along the diameter and promotes growth along the length, resulting in the formation of anisotropic rod-like structure [13].

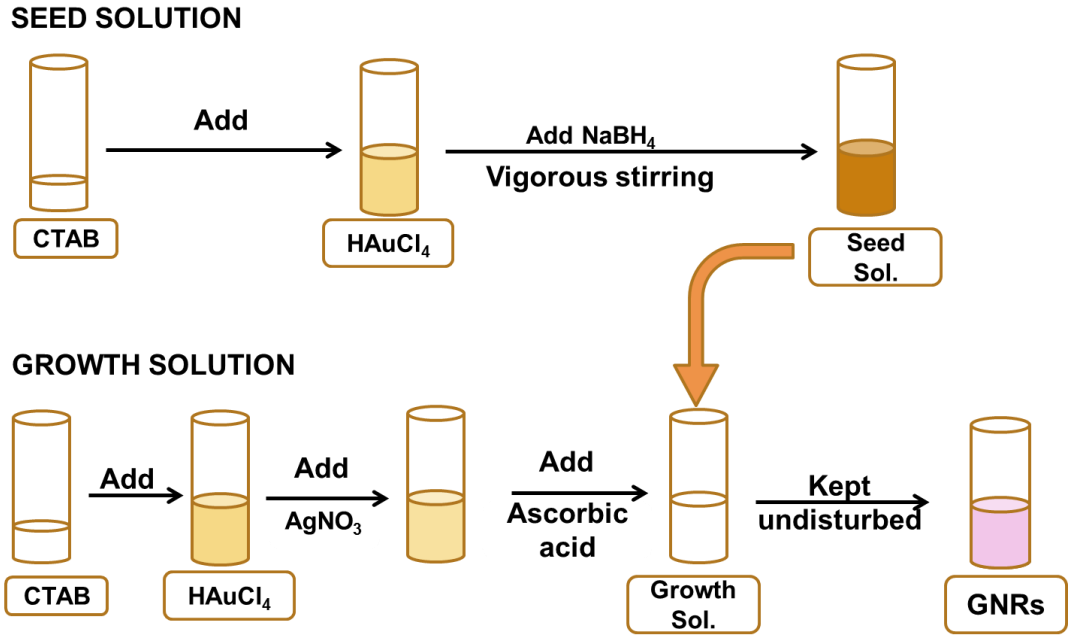

Fig. 3.1 Schematic diagram representing seed-mediated synthesis of GNRs.

Concentration of CTAB determines the shape of the nanostructures. If the concentration of CTAB is below its CMC (1.0 mM), the reduction of gold salt results in the formation of isotropic spherical nanoparticles [16]. Below CMC, the counter ion has minute effect on the structure of the adsorbed layer [16]. Above CMC, anisotropic shape develops as the major product. Above CMC, the surface excess concentration of CTAB is 60% more, making the structure of the adsorbed surfactant as densely packed "wormlike micelle" [16]. CTAB forms a bilayer on surface of growing nanoparticle. This selective adsorption of CTAB on the surface of growing nanoparticles promotes the directional growth of nanoparticles resulting into the rod shape.

To understand the effect of concentration of CTAB on the size and shape of nanoparticles, CTAB concentration is varied from 0.01 M to 0.2 M in the synthesis protocol presented in **Fig 3.1** and explained in **Annexure-I** section **A1**. To evaluate the effect of

CTAB concentration on the size and shape and hence on the plasmonic properties of as-synthesized nanoparticles, UV-Visible spectroscopy of as-synthesized gold nanoparticles was recorded (**Fig. 3.2**). Two plasmon bands are observed in the UV-Visible spectrum of each sample, indication the formation of anisotropic nanoparticles. Size and size distribution of gold nanoparticles obtained from transmission electron microscopy and photon correlation spectroscopy are shown in **Fig. 3.3, 3.4** and **3.6** respectively.

High aspect ratio GNRs have been prepared with 0.01 M CTAB at 0 ºC [17]. However, CTAB precipitates under these conditions. CTAB crystallizes below 25 °C [18]. CTAB exhibits triple point at 0.1 M and at 25 °C where crystals, individually dissolved molecules, and spherical micelles coexist. Koeppl et al. reported formation of spherical gold nanoparticles at 33 °C with 0.01 M CTAB [19]. Increase in the CTAB concentration from 0.1 M to 0.25 M did not lead to any significant change in the aspect ratio or yield of gold nanoparticles [19]. In this study, CTAB concentration of 0.01 M at temperatures above 27 ºC, results in the formation of anisotropic GNRs. This is evidenced from two plasmon bands centered at 532 nm and 711 nm in the UV-Visible spectra of GNRs corresponding to the TSPR and LSPR bands, respectively (**Fig 3.2 (a)**). Rod like morphology is also observed in the TEM micrograph of GNRs when prepared with 0.01 M CTAB (**Fig. 3.3**).

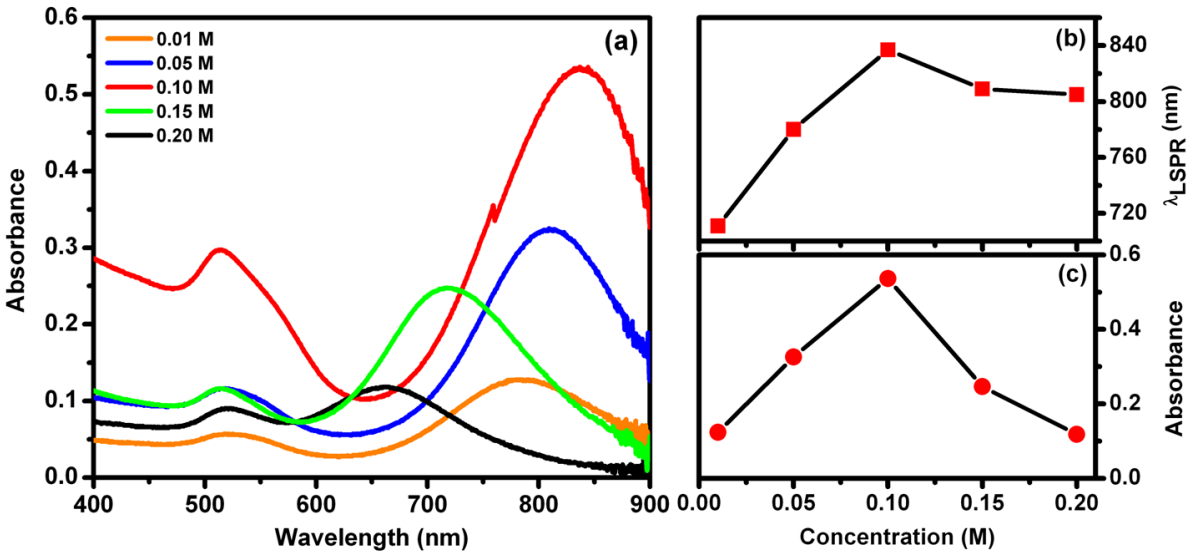

Fig. 3.2 (a) UV-Visible spectra of GNRs synthesized with 0.01-0.2 M CTAB. (b) Variation in the LSPR band position and (c) corresponding absorbance as a function of CTAB concentration. Trend lines are drawn for clear viewing.

With increase in CTAB concentration, LSPR band red shifts with corresponding increase in the absorbance. At 0.10 M CTAB both the LSPR band position and its absorbance are highest (837 nm and 0.54, respectively). Further increase in CTAB concentration, lead to the blue shift of LSPR band with the decrease in its absorption maximum (**Fig. 3.2 (b, c)**). To understand the effect of CTAB concentration on the physical size and morphology of gold nanoparticles, transmission electron microscopy is used. **Fig 3.3** shows TEM images of gold nanoparticles prepared with different CTAB concentrations.

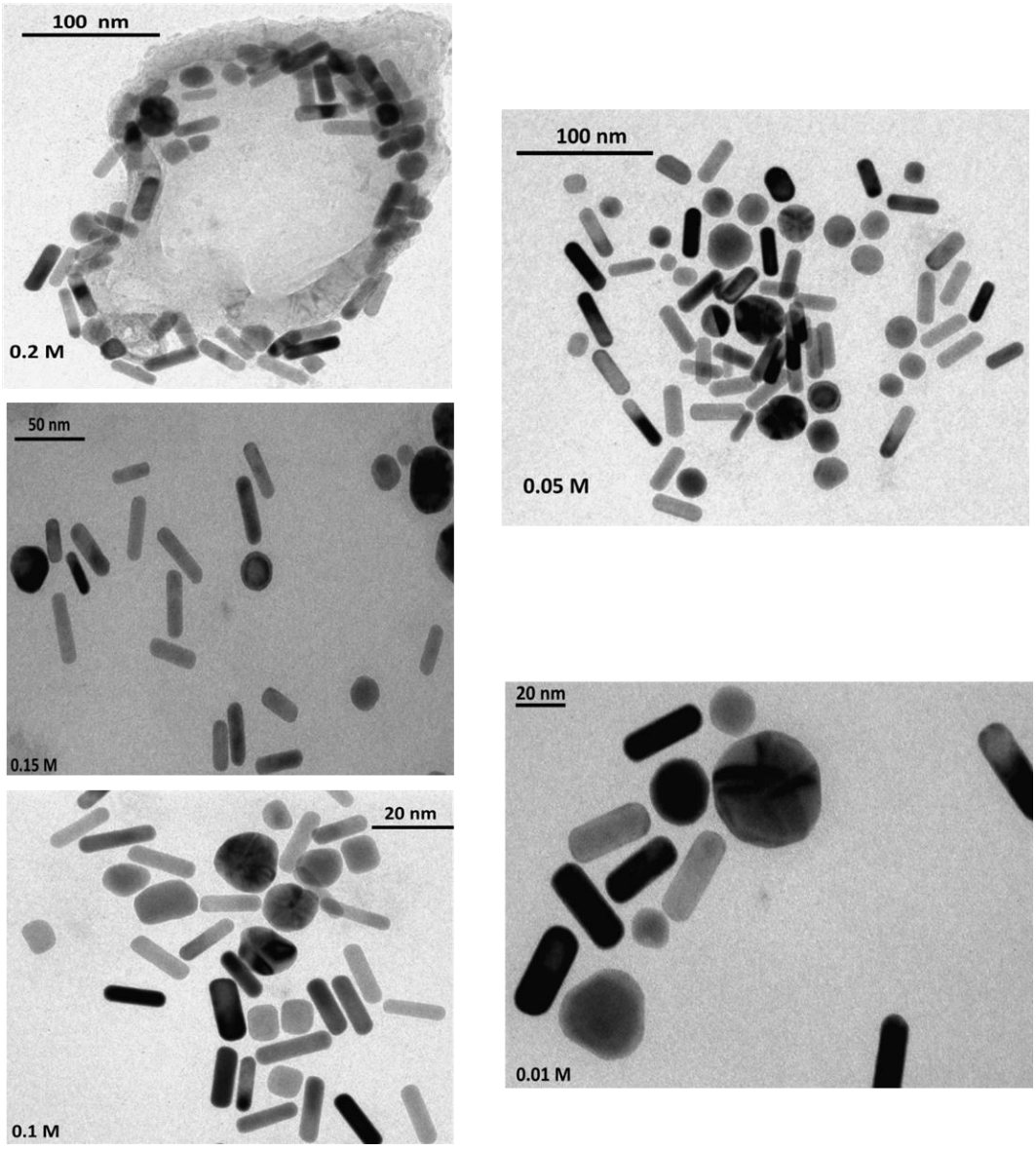

Fig. 3.3 TEM micrographs of as-synthesized gold nanoparticles prepared with 0.01-0.2 M CTAB. Rods are the major product with presence of few spherical and cubical shape nanoparticles as by product.

In each micrograph, anisotropic rod like structures is visible as major product with the presence of few isotropic gold spheres as byproduct. The size distribution histograms (**Fig. 3.4**) were prepared by measuring the length and the width of the nanorods from TEM micrographs presented in **Fig. 3.3**. Histograms were fitted with the lognormal particle size distribution function [2],

$$P(D) = \frac{1}{(D\sigma\sqrt{2\pi})} \exp[-\frac{(\ln(\frac{D}{D_o}))^2}{2\sigma^2}] \qquad 3.1$$

Where σ is the standard deviation, D is the particle diameter and ln D_o is the mean of ln D.

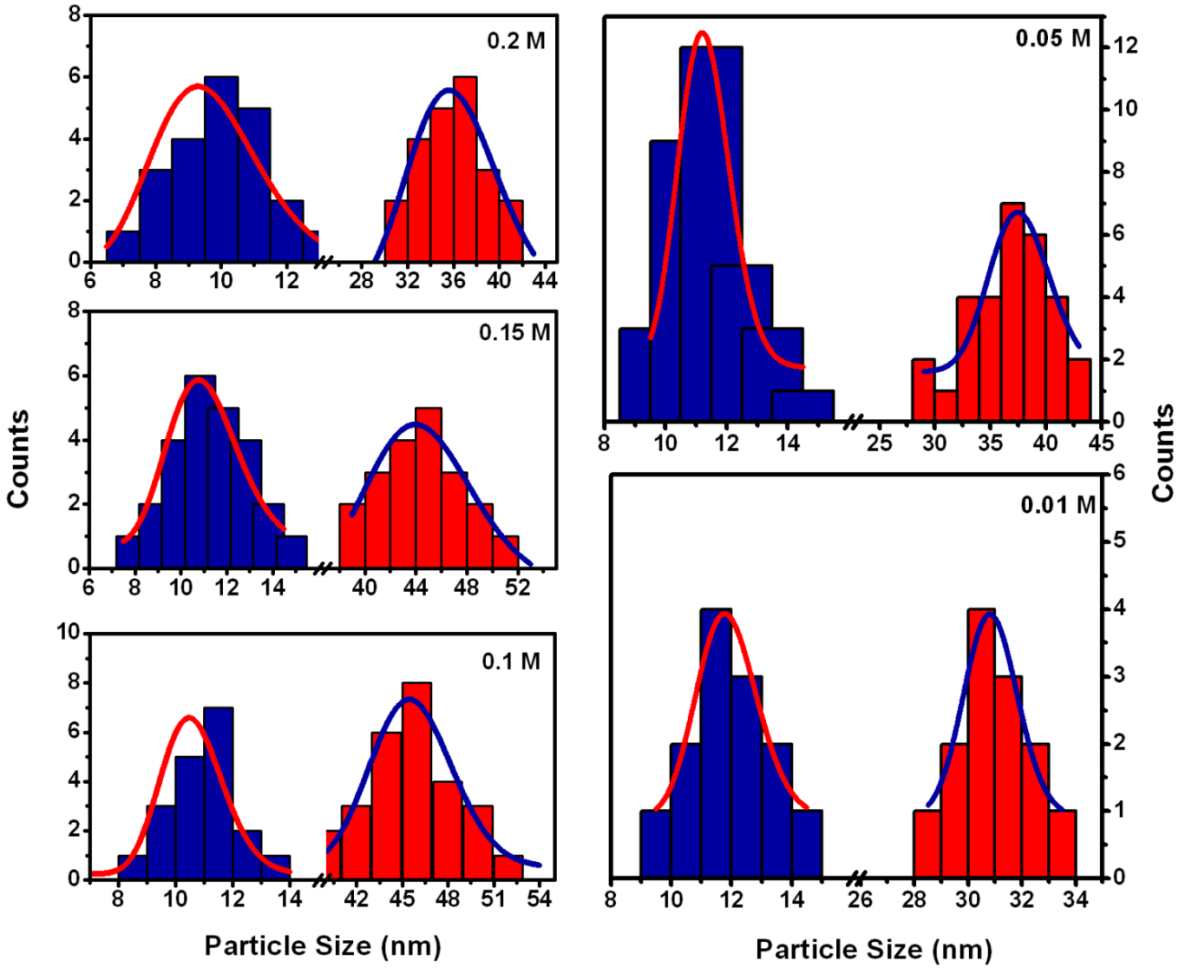

Fig. 3.4 Size distribution histograms of GNRs obtained from transmission electron microscopy. Histograms are fitted with the lognormal particle size distribution.

The average physical sizes obtained from the fits along with their aspect ratios are plotted as a function of CTAB concentration in **Fig. 3.5 (a, b)**. Aspect ratio of GNRs can also be estimated from the discrete dipole approximation (DDA) [2],

$$\lambda_{LSPR} = 96AR + 418 \quad (3.2)$$

where, AR is the aspect ratio of GNRs. Aspect ratio of GNRs obtained from this approximation is also plotted in **Fig. 3.5 (b)** and results are summarized in **Table 3.1**. The aspect ratios determined from the DDA calculations and from the TEM images do not match. This is due to the fact that DDA calculations were performed on UV-Visible spectra of as-synthesized GNRs while TEM microscopy was done on the centrifuged and purified samples of GNRs.

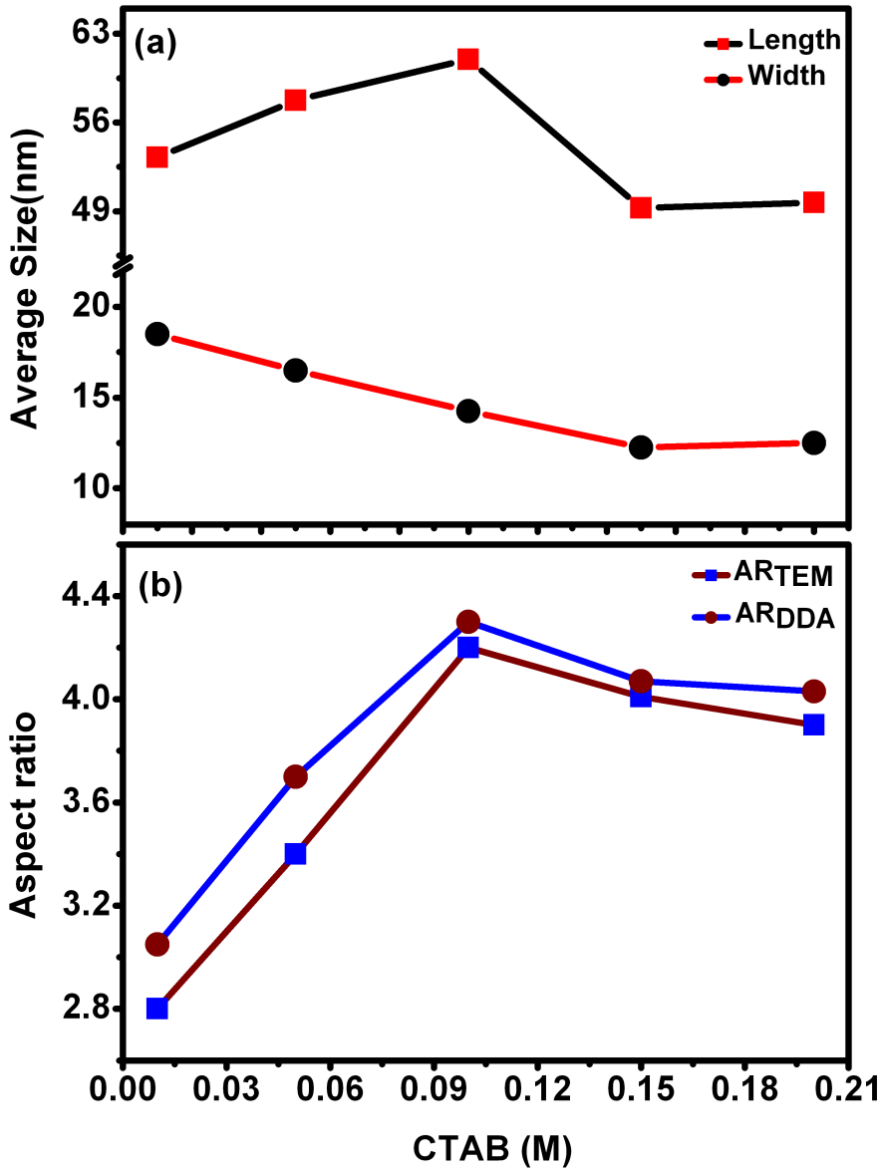

Fig. 3.5 Variation in the (a) physical size and (b) aspect ratio of GNRs as a function of CTAB concentration. AR_{TEM} is the aspect ratio determined from TEM and AR_{DDA} is the aspect ratio obtained from DDA calculations. Trend lines are drawn for clear viewing.

Table 3.1 Average length (D_{LSPR}), width (D_{TSPR}) approximation and aspect ratio (A.R.) of GNRs obtained from TEM micrographs and aspect ratios calculated from DDA.

CTAB (M)	D_{LSPR} (nm)	D_{TSPR} (nm)	$A.R._{TEM}$	$A.R._{DDA}$
0.01	53.25	18.50	2.80	3.05
0.05	57.57	16.50	3.40	3.70
0.10	**60.97**	**14.25**	**4.20**	**4.30**
0.15	49.26	12.25	4.01	4.07
0.20	49.70	12.51	3.90	4.03

The hydrodynamic size distributions of GNRs dispersed in DI water are also determined by photon-correlation spectroscopy. Size distribution histograms are fitted with lognormal particle size distribution function and the mean hydrodynamic size corresponding to the length and the width of GNRs are determined **(Fig. 3.6)**. Results are summarized in **Table 3.2**. Hydrodynamic size corresponding to the length increases when the concentration of CTAB increases from 0.01 M to 0.1 M and decreases when the CTAB concentration is >0.1 M (**Table 3.2**). Hydrodynamic size of GNRs corresponding to the length is maximum at 0.1 M CTAB. Hydrodynamic size of GNRs corresponding to the width decreases continuously upto 0.15 M and then increases slightly at 0.2 M concentration of CTAB. The mean hydrodynamic size obtained for each concentration of CTAB is greater than that of its physical size. This is quite obvious as hydrodynamic size also take the CTAB bilayer into the consideration while the TEM considers only the bare nanoparticles.

Table 3.2 Hydrodynamic size of length (D_{LSPR}), width (D_{TSPR}) and aspect ratios of GNRs synthesized at different molar concentrations of CTAB.

CTAB (M)	D_{LSPR} (nm)	D_{TSPR} (nm)	Aspect ratio
0.01	52.25	18.30	2.8
0.05	57.75	16.15	3.5
0.10	60.97	14.83	4.1
0.15	49.26	11.93	4.1
0.20	48.71	13.12	3.7

It is observed that the rod formation did not occur at low CTAB concentrations assuming that the equilibrium constant in these cases is too low for an effective adsorption of CTAB at the crystal faces [16]. On the other hand, at higher CTAB concentration the formation of cylindrical micelles might compete with the CTAB adsorption at the crystal

facets, i.e. fewer number of CTAB molecules are available for the adsorption on the nanoparticles surface which then could lead to isotropic spherical particle growth [19].

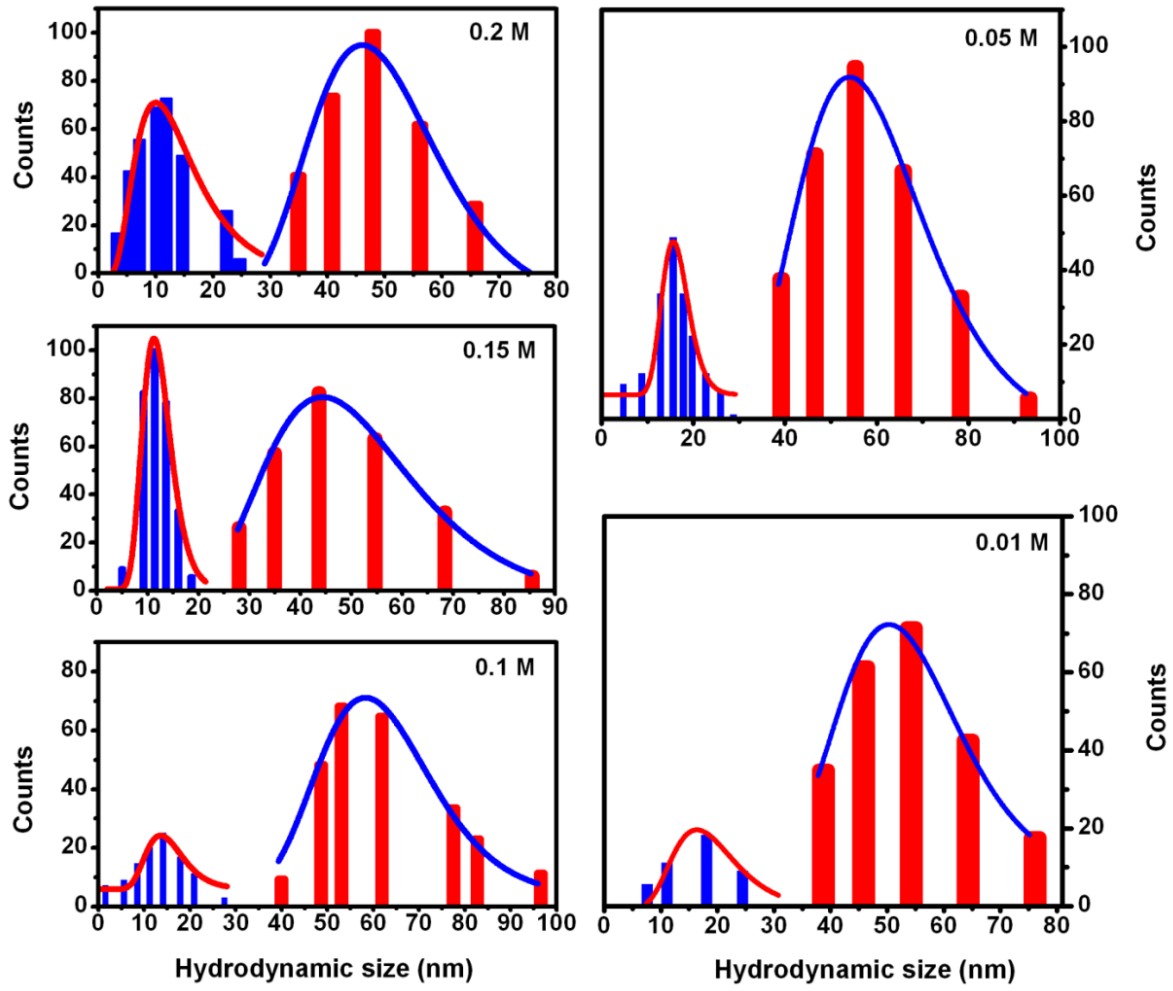

Fig 3.6 Hydrodynamic size distribution fitted with lognormal particle size distribution function of histograms of GNRs prepared at different CTAB concentrations.

3.2.2.2 The Gold Precursor

Tetrachloroauric acid ($HAuCl_4$) is generally used as a gold source for GNRs synthesis [4-6]. It passes through three different oxidation states during the synthesis: Au(III) in the precursor, Au(I) as an intermediate, and Au(0) in the nanoparticles [20]. Au(III) forms a square-planar complex in its d^8 electronic state. From the Ligand Field Theory, the binding of Au(III) with halide ions follows the series $I^- > Br^- > Cl^-$. Consequently, bromide ions replace the four chloride ions from $AuCl_4^-$ in the presence of CTAB as [21]

$$[AuCl_4]^- \leftrightarrow [AuCl_3Br]^- \leftrightarrow [AuCl_2Br_2]^- \leftrightarrow [AuClBr_3]^- \leftrightarrow [AuBr_4]^- \quad (3.3)$$

This replacement is revealed by a color change from pale-yellow to dark orange. $AuBr_4^-$ ion forms an ion pair with the quaternary ammonium surfactant monomers. These monomers require a surfactant concentration with a 60:1 ratio to ensure dissolution in water [22]. Exchange of ligands from $AuCl_4^-$ to $AuBr_4^-$ and the formation of $AuBr_4^-CTA^+$ complex influences the redox potential [22]. Variation in the redox potential affects the growth kinetics. It is important to ensure that the gold salt has been completely dissolved and ligand exchange complete. Additionally, equilibrium is essential to be maintained amongst all the three oxidation states of Au, which can be pushed toward coproportionation or disproportionation reactions, depending on the relative stability of each species as [21]

$$Au^{3+} + 2\,[Au^0] \leftrightarrow 3Au^+ \quad (3.4)$$

In the growth solution, the most stable species are Au(I); meaning that the equilibrium is placed toward the coproportionation between Au(III) and Au(0), i.e., Au nanorods (or other Au nanoparticles) will be oxidized in the presence of Au(III) [21, 22]. In this scenario, a central role is played by the reducing agent which will be discussed later in this chapter.

To understand the effect of gold precursor concentration on the quality and quantity of GNRs, $HAuCl_4$ concentration was varied from 0.1 mM to 2 mM while keeping the CTAB concentration constant at 0.1 M. Rest of the parameters i.e. $AgNO_3$, ascorbic acid and seed concentration were also kept constant. The experimental protocol is otherwise same as explained in **Annexure-I** (section **A1**).

It is observed that rod dimensions strongly depend on the total amount of gold ions (Au^+) present in the solution. The correlation between GNRs dimensions, their yield and Au^{3+} ion concentration can be obtained from UV-Visible spectroscopy (**Fig. 3.7**) and transmission electron microscopy (**Fig. 3.8**) of as-synthesized GNRs. Formation of rod-shaped particles also depends on the $HAuCl_4$ concentration. $HAuCl_4$ concentration was varied from 0.1 mM to 2.0 mM. Well-defined nanorods are formed for 0.5 mM and 1.0 mM of $HAuCl_4$. For 2.0 mM $HAuCl_4$, very few nanorods are formed (**Fig. 3.8**). The color of the growth solution was also fade yellow at this concentration. On adding seed solution it took

longer than normal for the growth of GNRs. Thicker GNRs are formed and aspect ratio of GNRs is also low (**Table 3.3**). The roles of the gold precursor source and the weak reducing agent (ascorbic acid (AA)) are intertwined [23]. Ascorbic acid reduces the gold ions which then crystalize on the rod tips leading to growth [21]. Too much concentration of reduced gold Au^0 can overpower this process leading to other shapes, while too little reduced gold allows the "catalyst" silver to dominate, limiting the growth of the rods along the long axis [23].

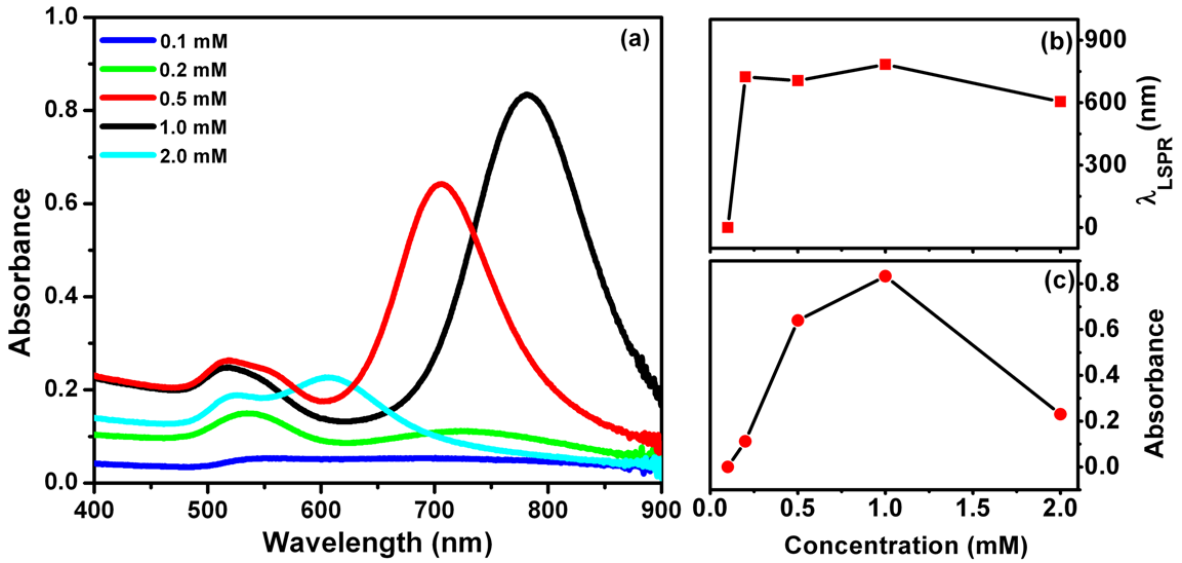

Fig. 3.7 (a) UV-Visible spectra of GNRs synthesized with 0.1–2.0 mM $HAuCl_4$. Variation in the (b) LSPR band position (c) corresponding absorbance as a function of $HAuCl_4$ concentration. Trend lines are drawn for clear viewing.

Fig. 3.7 (b) and (c) shows the effect of $HAuCl_4$ concentration on the LSPR band position and corresponding absorbance. GNRs synthesized with 1.0 mM $HAuCl_4$ have highest red-shift of LSPR band with maximum absorbance (**Fig. 3.7**). Aspect ratio at this concentration is also maximum (**Table 3.3**). The GNRs yield also increases with increase in $HAuCl_4$ concentration and it is highest for 1mM of $HAuCl_4$ as evidenced from the absorbance maximum of LSPR band (**Fig. 3.7 (c)**). Spectral bands corresponding to 0.1 and 0.2 mM concentrations show very weak absorption signals in their UV-Visible-NIR spectra. Very few rod-shaped nanoparticles might have been formed at these concentrations of $HAuCl_4$. Thus, 1.0 mM $HAuCl_4$ may be the optimum concentration for the synthesis of GNRs with well-defined morphology and better yield.

Effect of $HAuCl_4$ concentration on the morphology of gold nanoparticles synthesized with 0.1-2.0 mM $HAuCl_4$ is shown in **Fig. 3.8**. Well-defined GNRs are formed with 1.0 mM $HAuCl_4$. Only few GNRs are formed at 0.2 mM $HAuCl_4$. No GNRs are observed in the TEM image at 0.1 mM $HAuCl_4$. Higher concentration of $HAuCl_4$ (2.0 mM) yield GNRs with short aspect ratio. Size distribution histograms of as-synthesized GNRs fitted with the lognormal particle size distribution function are shown in **Fig. 3.9**. Size distribution histograms of GNRs corresponding to 0.1 mM $HAuCl_4$ could not be recorded due to very low concentration of nanoparticles. Hence size-distribution histogram corresponding to this concentration is not shown in **Fig. 3.9**.

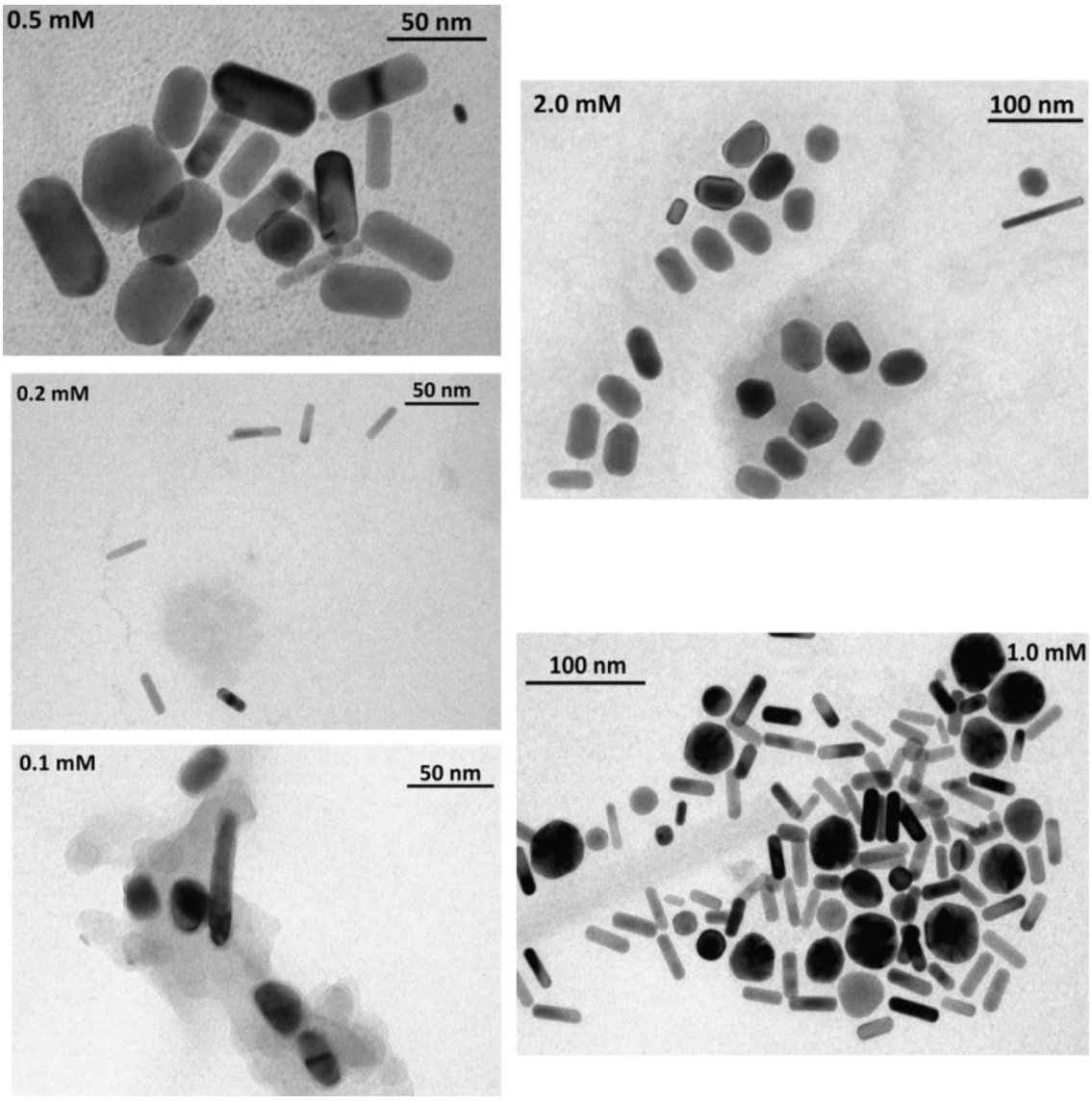

Fig. 3.8 TEM micrographs of GNRs synthesized at different concentrations of $HAuCl_4$.

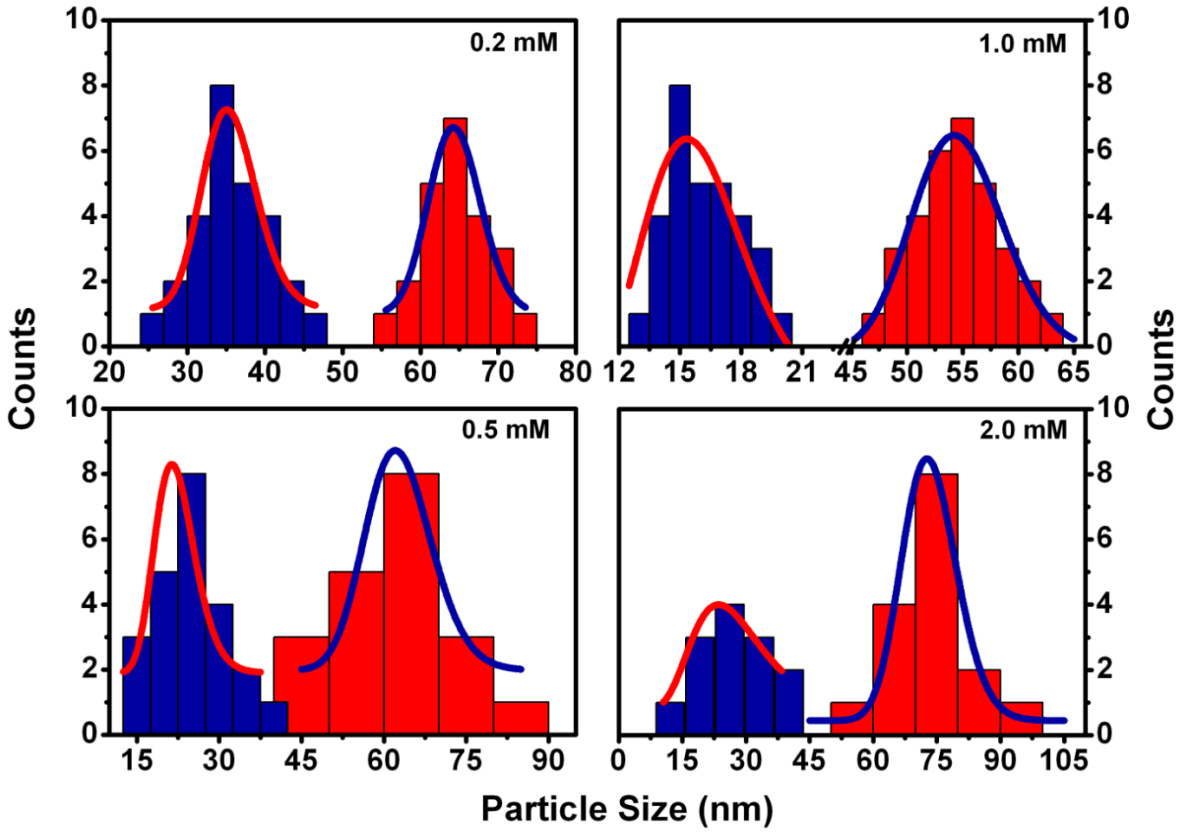

Fig. 3.9 Size distribution histograms fitted with lognormal particle size distribution of GNRs prepared with different concentration of $HAuCl_4$ obtained from TEM.

The average physical size obtained from the fit along with their aspect ratios are plotted as a function of $HAuCl_4$ concentration in **Fig. 3.10**. Aspect ratios of GNRs are also calculated from discrete dipole approximation (DDA). Aspect ratios obtained from TEM and DDA calculations are plotted in **Fig. 3.10 (b)**.

The hydrodynamic size distribution histograms of GNRs fitted with lognormal particle size distribution synthesized with different concentration of $HAuCl_4$ is shown in **Fig. 3.11**. Multimodal size distributions are observed corresponding to the length and the width of GNRs. Average hydrodynamic size corresponding to length and width of GNRs are summarized in **Table 3.4**.

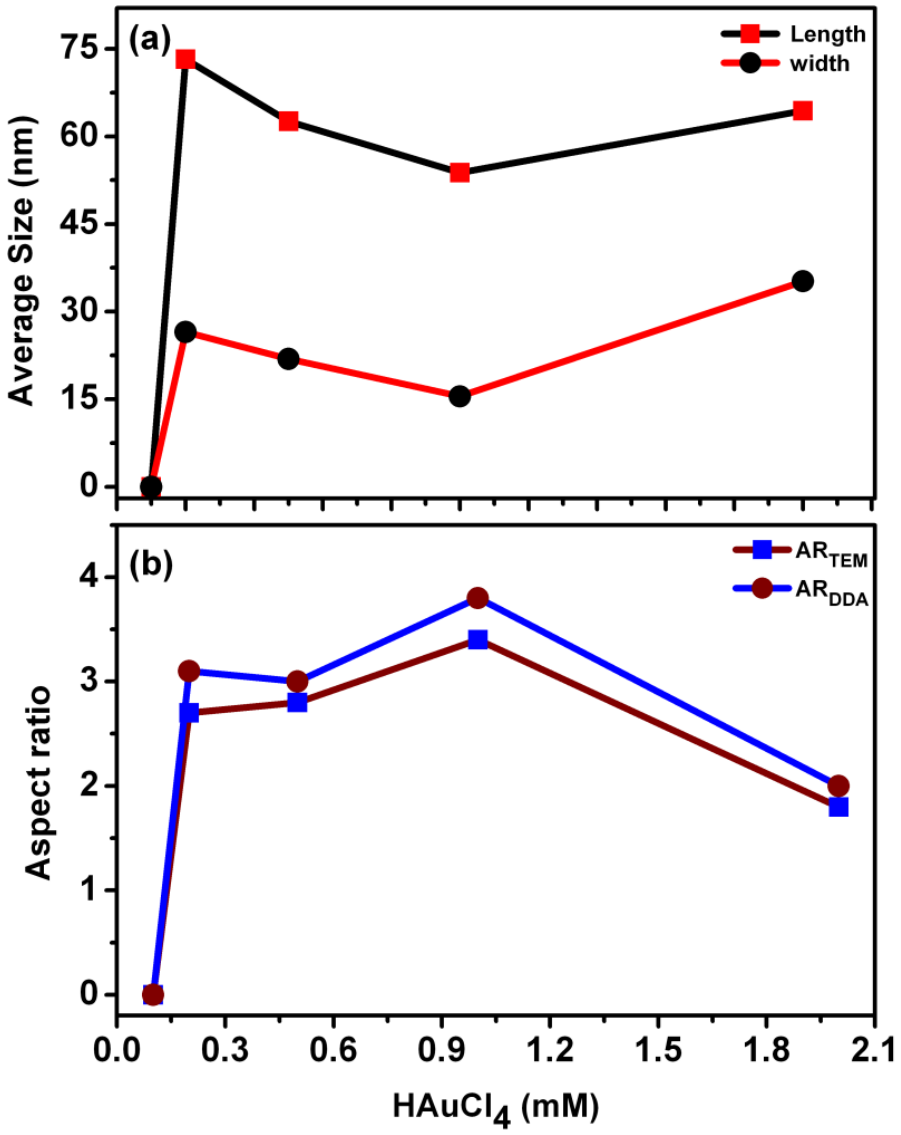

Fig. 3.10 Variation in the (a) size and (b) aspect ratio of GNRs. AR_{TEM} is the aspect ratio determined from TEM and AR_{DDA} is the aspect ratio obtained from DDA calculations. Trend lines are drawn for clear viewing.

Table 3.3 Average length (D_{LSPR}), width (D_{TSPR}) and aspect ratio ($A.R._{TEM}$) of GNRs obtained from TEM micrographs. $A.R._{DDA}$ is the aspect ratio calculated from DDA calculations.

$HAuCl_4$ (mM)	**D_{LSPR} (nm)**	**D_{TSPR} (nm)**	**$A.R._{TEM}$**	**$A.R._{DDA}$**
0.1	00.0	00.0	0.0	0.0
0.2	73.2	26.5	2.7	3.1
0.5	62.6	21.9	2.8	3.0
1.0	**53.8**	**15.5**	**3.4**	**3.8**
2.0	64.4	35.2	1.8	2.0

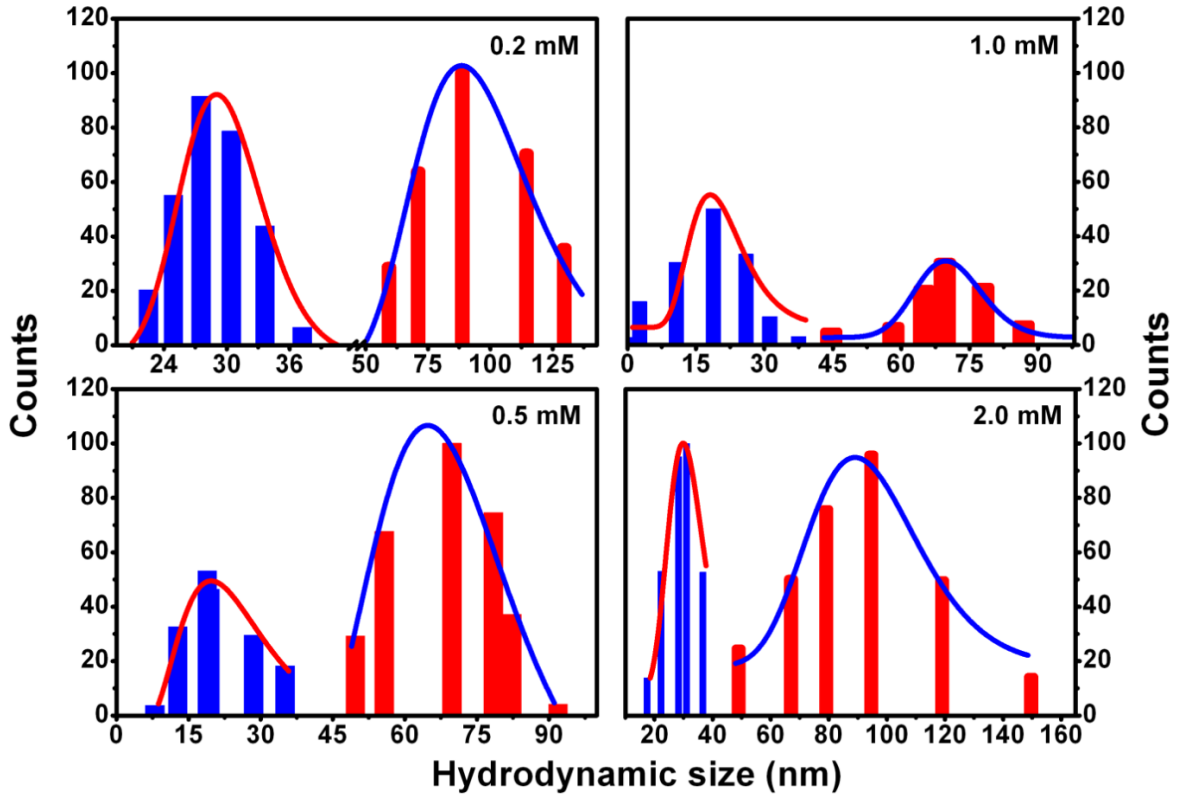

Fig. 3.11 Hydrodynamic size distribution histogram of GNRs fitted with lognormal particle size distributions which are prepared with 0.1-2.0 mM $HAuCl_4$.

Table 3.4 Hydrodynamic size of GNRs synthesized with 0.1-2.0 mM $HAuCl_4$.

$HAuCl_4$ (mM)	D_{LSPR} (nm)	D_{TSPR} (nm)
0.1	-	-
0.2	89.2	29.3
0.5	64.7	20.1
1.0	70.1	19.8
2.0	92.4	28.7

3.2.2.3 The Reducing Agent: Ascorbic Acid

Growth of GNRs in the seed-mediated method occurs when Au(III) is reduced to Au(0) primarily by weak reducing agent and secondarily by Au seeds [23]. Ascorbic acid (AA) is used as weak reducing agent so that reduction of gold salt proceeds slowly. Slower growth rates are desirable for anisotropic growths of nanoparticles [24]. To understand the effect of type of reducing agent, AA was replaced by various other reducing agents in literature [24, 25]. The most persistent choice is still the ascorbic acid. $NaBH_4$ − the strong reducing agent

is also used for the synthesis of gold seeds. On replacing AA with $NaBH_4$ in the growth solution, it reduces the Au(III) and forms deep red color colloid on adding gold seeds, thus resulting in the formation of spherical gold nanoparticles. This is also evident from a single SPR peak (black line) shouldered at 520 nm in the UV visible spectrum of these nanoparticles (**Fig. 3.12**).

When AA alone is used as reducing agent without the addition of seeds no color change was observed in the growth solution for 24 h. The solution remained colorless and no signature of nanoparticles formation was observed in the UV-Visible-NIR spectrum. These nanoparticles have an identical UV-Visible-NIR spectra to that observed for gold seeds (redline). It is only when the seeds are added to the growth solution, formation of nanorods takes place (blue line) (**Fig. 3.12**). Formation of GNRs can also be confirmed from two plasmon resonance bands in the UV-Visible-NIR spectrum of these nanoparticles. Thus it is concluded that weak reducing agent AA is essential for the anisotropic growth in the form of GNRs.

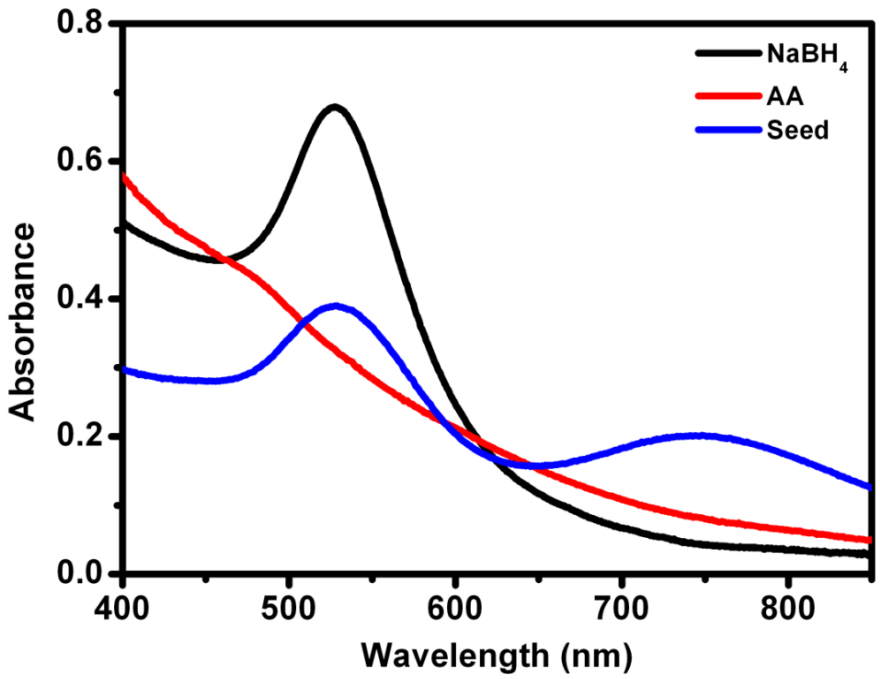

Fig. 3.12 UV-Visible spectra of gold nanoparticles prepared with $NaBH_4$, AA and gold seeds.

The growth solution containing ($HAuCl_4$ + $AgNO_3$ + CTAB) is of deep orange color prior to the addition of AA. This color is because of the metal-to-ligand charge-transfer

bands with maxima at 255, 294, 381, 452, and 546 nm [26]. These bands are observed due to the absorption by $[AuBr_4]^-$ ions formed as a result of ligand substitution of $[AuCl_4]^-$ in the presence of Br^- ions [26, 27]

$$[AuCl_4]^- + 4Br^- \rightarrow [AuBr_4]^- + 4Cl^- \qquad 3.5$$

When AA is added to the growth solution, the orange color of the solution disappears. The disappearance of the orange color is due to the reduction of $[AuBr_4]^-$ to Au^0,

First reduction: $Au^{3+} \rightarrow Au^{1+}$

$$CTA^-AuBr_4 + C_6H_8O_6 \rightarrow CTA^-AuBr_2 + C_6H_6O_6 + 2H^+ + 2Br^- \qquad 3.6$$

Second reduction: $Au^{1+} \rightarrow Au^0$

$$2\,CTA^-AuBr_2 + C_6H_8O_6 \rightarrow 2Au^0 + C_6H_6O_6 + 2CTA^+ + 2H^+ + 4Br^- \qquad 3.7$$

The first reduction is confined in the metallomicelles. The second reduction begins only after the seed is added. The overall reaction is

$$2CTA^-AuBr_4 + 3C_6H_8O_6 \rightarrow 2Au^0 + 3C_6H_6O_6 + 2CTA^+ + 6H^+ + 8Br^- \qquad 3.8$$

As discussed in the previous section, the roles of Au^+ and AA in the growth solution are intertwined. Effect of the concentration of AA on the optical bands of GNRs has been studied. The molar ratio of Au^+: AA was changed from 0.9 to 1.5.

When the molar ratio of AA to gold ions (1:0.9) is less than the stoichiometric ratio (1:1), unreduced Au^+ remain in the growth solution after the growth stops [28]. It is evident from the light yellow color of the growth solution. Growth in this case did not complete because of the presence of unreduced gold salt in the solution. No prominent peak in the UV-Visible-NIR spectrum was observed in this case (**Fig. 3.13**). When the molar ratio was at 1:1; the solution becomes colorless on addition of AA, indicating 1:1 is the minimum molar ratio of Au^+: AA for complete reduction of Au.

Further increase in the molar ratio of Au^+: AA results in red-shift of LSPR band (**Fig. 3.13**). When this ratio is increased beyond 1:1.1 the LSPR band starts shifting towards the smaller wavelengths. This initial red-shift can be related to the apparent increase in length of GNRs resulting in the increase in their aspect ratios. Later the growth along the diameter

overtook the growth along the length resulting in the decrease in the aspect ratio of GNRs. Reduction of Au also depends on the concentration of the reducing agent. As the amount of AA increases, the rate of reduction of gold ions also increases [24]. Because of this, before the surfactants can confine the growth direction the reduction of Au^{3+} to Au^{0} takes place leading to isotropic growth in the form of spheres.

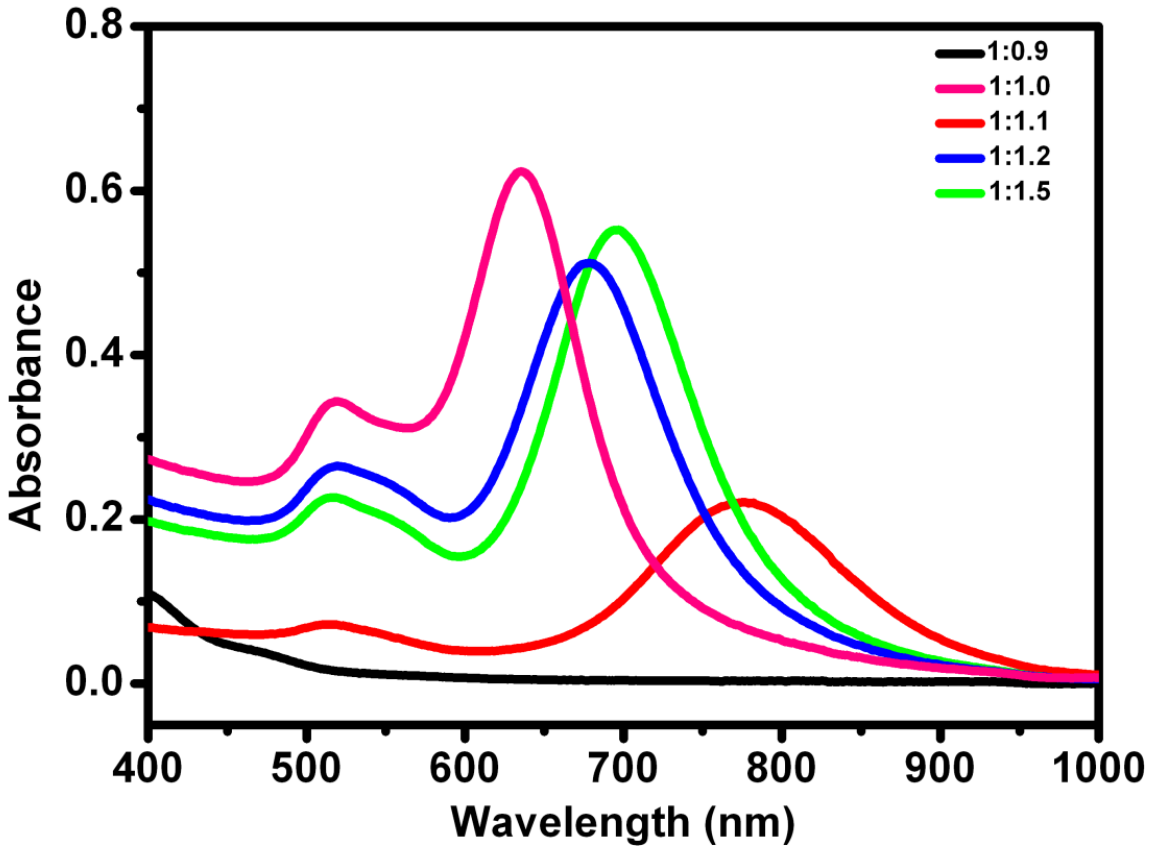

Fig. 3.13 UV-Visible-NIR spectra of GNRs prepared at 1:0.9-1:1.5 molar ratios of Au^{+}: AA.

The hydrodynamic size distribution histograms of GNRs fitted with lognormal particle size distribution synthesized with different molar ratio of Au^{+}: AA is shown in **Fig. 3.14**. The average hydrodynamic size corresponding to the length and the width of GNRs are summarized in **Table 3.5**. Bimodal particle size distribution is observed for molar ratios ≥ 1.1 indicating the formation of anisotropic nanoparticles. No particle size distribution is obtained in photon correlation spectroscopy of gold nanoparticles corresponding to 1:0.9 molar ratio of Au^{+}: AA. It is because of the lack of formation of nanoparticles at this concentration.

Table 3.5 Hydrodynamic size (D_{LSPR}-length and D_{TSPR}-width) of GNRs synthesized at 1:0.9-1:1.5 molar ratios of Au^{+}: AA.

Au^{+}: AA	D_{LSPR} (nm)	D_{TSPR} (nm)
1:0.90	-	-
1:1.00	36.9	169.3
1:1.10	13.4	41.6
1:1.20	24.2	94.0
1:1.50	9.60	37.5

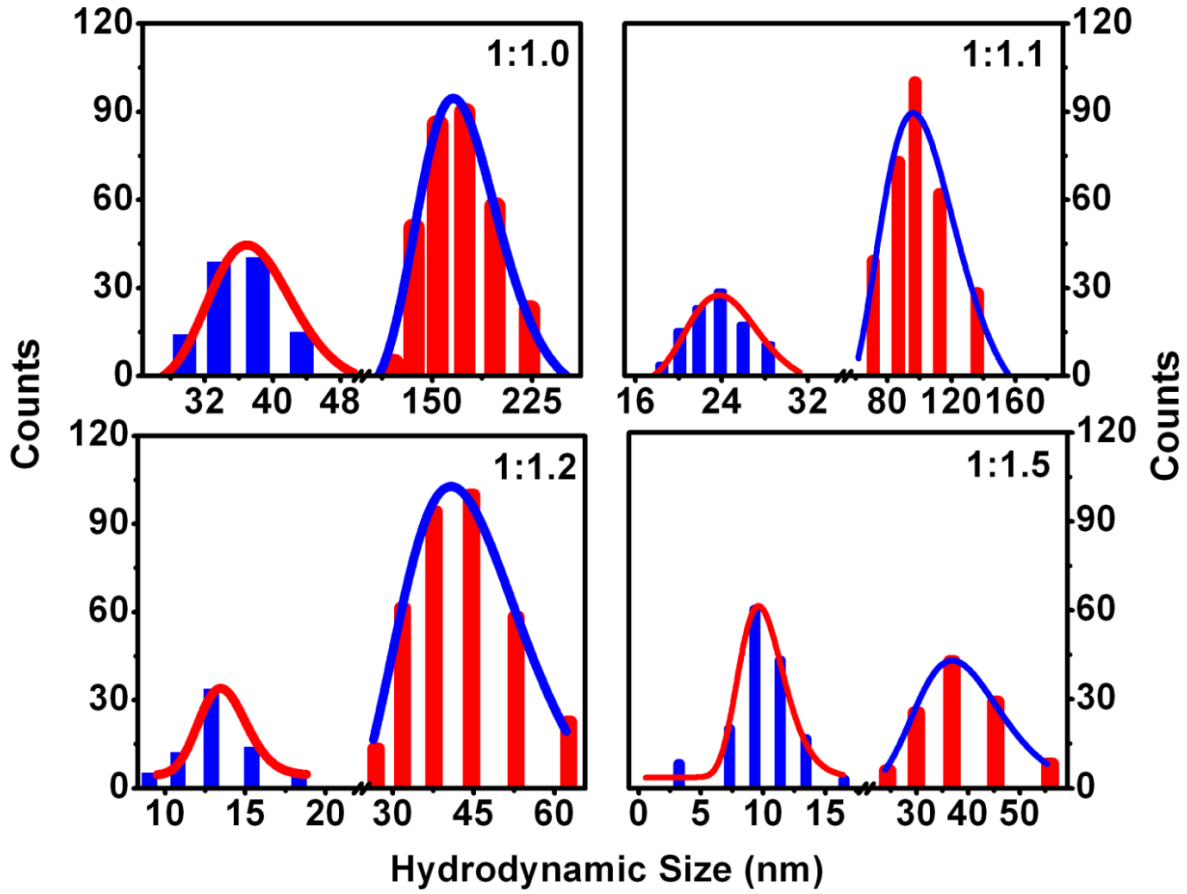

Fig. 3.14 Hydrodynamic size distribution histograms of GNRs fitted with lognormal particle size distribution synthesized with 1:0.9-1:1.5 molar ratio of Au^{+}: AA.

3.2.2.4 Silver Ions

The importance of silver (Ag) ions in GNRs synthesis came from the electrochemical and photochemical synthesis whereby it was noticed that by increasing the silver-ion concentration there is an increase in the aspect ratio of GNRs [29, 30]. In seed-mediated

synthesis, silver nitrate is introduced in the gold solution before the seed addition to facilitate the rod formation and to tune the aspect ratio as well [30].

It was found that addition of $AgNO_3$ influences the yield and the aspect ratio of GNRs [29]. To understand the role of silver in GNRs elongation we have synthesized gold nanoparticles under identical conditions (as explained in **Annexure-I** section **A1**) with 0-1000 µL of 4 mM $AgNO_3$. When no silver (0 µL) was added into the growth solution, only spherical nanoparticles are formed as the end product. This is evident from the single plasmon resonance peak in the UV-Visible-NIR spectra (**Fig 3.15 (a)**). Gold nanoparticles formed in the presence of silver show two plasmon bands. The LSPR band red-shifts with increase in the $AgNO_3$ volume from 70-300 µL. Further increase in the silver ions above 300 µL results in the blue shift of LSPR band signaling the decrease in the aspect ratio of GNRs (**Fig 3.15 (a)**). This blue shift continues till LSPR and TSPR bands merges with each other indicating the shift in the morphology from anisotropic rods to isotropic spheres. The negative effect of silver ions on the growth of GNRs at higher concentrations may be because of their interaction with the bromide counter ions of the surfactant monomer [4]. Change in the LSPR band position with the volume of $AgNO_3$ is shown in **Fig. 3.15 (b)**.

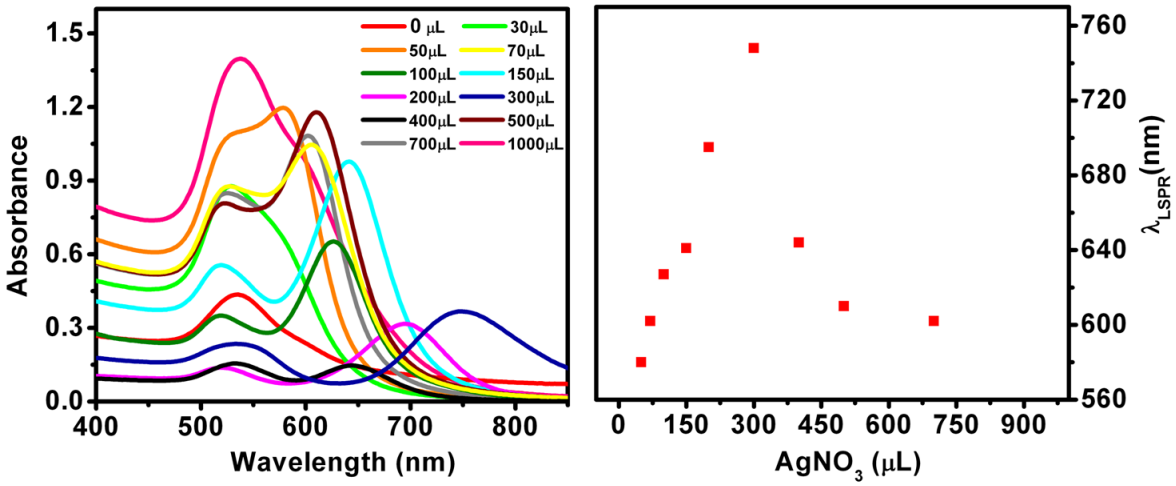

Fig 3.15 (a) UV-Visible spectra of GNRs prepared by varying $AgNO_3$ volume (0 µL-1000 µL). (b) Variations in LSPR band position as a function of $AgNO_3$ volume.

The hydrodynamic size distribution of GNRs was determined by the photon-correlation spectroscopy. Size distribution histograms were fitted with lognormal particle size distribution function and the mean hydrodynamic size of the particles were determined **(Fig. 3.16)**. Results are summarized in **Table 3.6**.

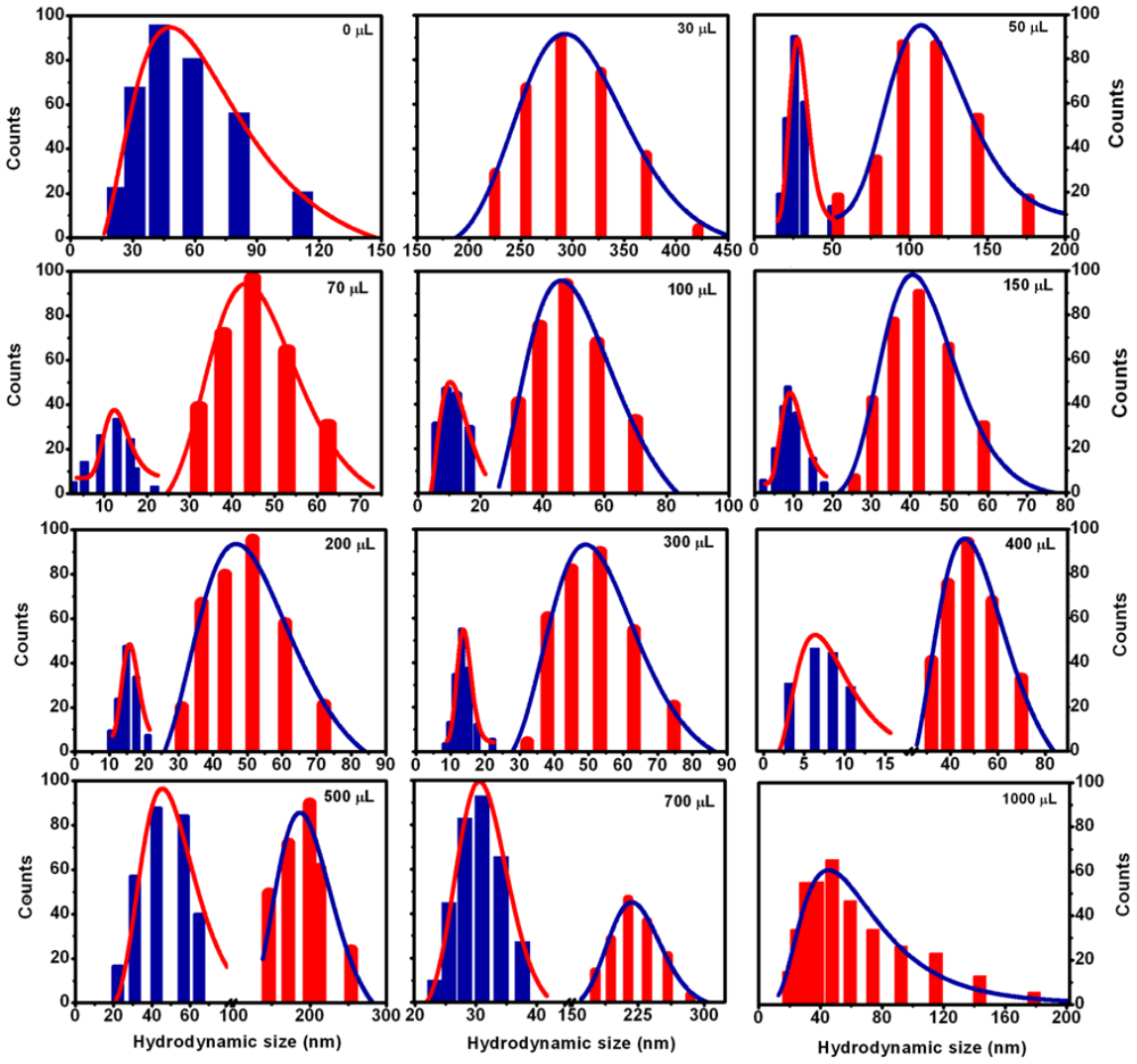

Fig. 3.16 Hydrodynamic particle size distributions of GNRs (prepared with 0-1000 µL $AgNO_3$) obtained from photon co-relation spectroscopy. Each histogram is fitted with lognormal particle size distribution function

Single size distribution is observed for samples that are prepared without $AgNO_3$ (0 µL) indicating the formation of sphere like symmetric nanoparticles. This observation is consistent with the presence of single plasmon peak in the UV-Visible-NIR spectroscopy. Single size distribution is also observed for gold nanoparticles prepared with 30 µL of $AgNO_3$. The mean hydrodynamic diameter of these gold nanoparticles is large (304.5 nm). It means that $AgNO_3$ at lower volume resulted in the growth of spherical nanoparticles. On addition of $AgNO_3$ volume ≥ 50 µL; anisotropic nanoparticles are formed. Bimodal size distribution is observed in the histogram of these nanoparticles. When $AgNO_3$ volume increases beyond 700 µL, a single size

distribution is again observed which corresponds to the spherical shape gold nanoparticles **(Fig. 3.16)**.

3.2.2.5 The Seed: Effect of Seed Aging

The aging of gold seeds before adding it into growth solution strongly affect the morphology and hence the plasmonic properties of gold nanoparticles. To evaluate the effect of aging of gold seed, gold nanoparticles are prepared under identical conditions (as explained in **Annexure-I** section **A1**) with gold seeds aged for 0-72 h. The UV-Visible-NIR spectra of the aged seeds indicate the change in seed size with aging (**Fig. 3.17 (a)**).

Table 3.6 Hydrodynamic size of (D_{LSPR}-length; D_{TSPR}-diameters) gold nanoparticles synthesized with 0-1000 µL $AgNO_3$.

$AgNO_3$ (µL)	**D_{LSPR} (nm)**	**D_{TSPR} (nm)**
0	48.4	-
30	293.3	-
50	27.3	108.2
70	12.0	43.2
100	11.2	46.3
150	09.6	40.9
200	15.3	46.1
300	14.2	49.1
400	06.6	95.5
500	45.4	187.4
700	30.7	219.9
1000	47.7	-

UV-Visible spectra of gold nanoparticles prepared with aged gold seeds are shown in **Fig 3.17 (b)**. Two distinct plasmon bands are observed here confirming the formation of GNRs. No significant effect of aging of gold seeds on the TSPR band position was observed. The LSPR band of GNRs undergoes a blue shift with increase in the seed aging. When seeds are aged for 72 h; only one plasmon resonance band is observed indicating the formation of spherical nanoparticles. Increase in the intensity of SPR band at 520 nm of gold seeds (**Fig. 3.17(a)**) indicates the growth of the spherical gold seeds. When the seed is aged for 72 h, this growth saturates. After 72 h of aging, the seed solution only contains spherical gold nanoparticles. These spherical nanoparticles when used as seeds, does not form any nanorods, Instead, spherical gold nanoparticles further grow

because of the ripening. This result indicates that only freshly prepared gold seeds should be used for the synthesis of GNRs.

To understand the effect of seed aging on the size and shape of GNRs, photon correlation spectroscopy was also used. **Fig. 3.18** shows the effect of seed aging on the size distribution of as-synthesized gold nanoparticles. Two distinct size distributions are observed corresponding to the short and long axis of GNRs when seeds were aged for 0-48 h. This bimodal hydrodynamic size distribution of gold nanoparticles further confirms that the synthesized nanoparticles have asymmetric morphology like rods. Results of PCS measurements are summarized in **Table 3.7**. A single size distribution is observed for gold nanoparticles prepared with seeds aged for 72 h; indicating the formation of spherical gold nanoparticles. This observation is consistent with the UV-Visible-NIR spectroscopy results (**Fig 3.17**).

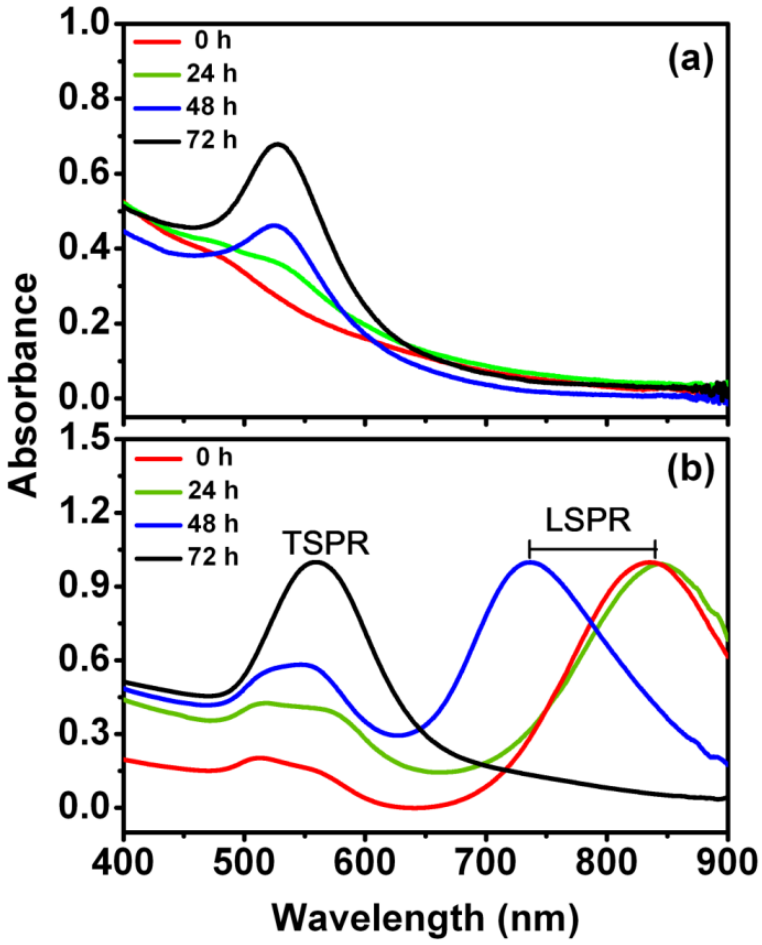

Fig. 3.17 UV-Visible spectra of (a) gold seeds aged for 0-72 h and (b) GNRs prepared with seeds aged for 0-72 h.

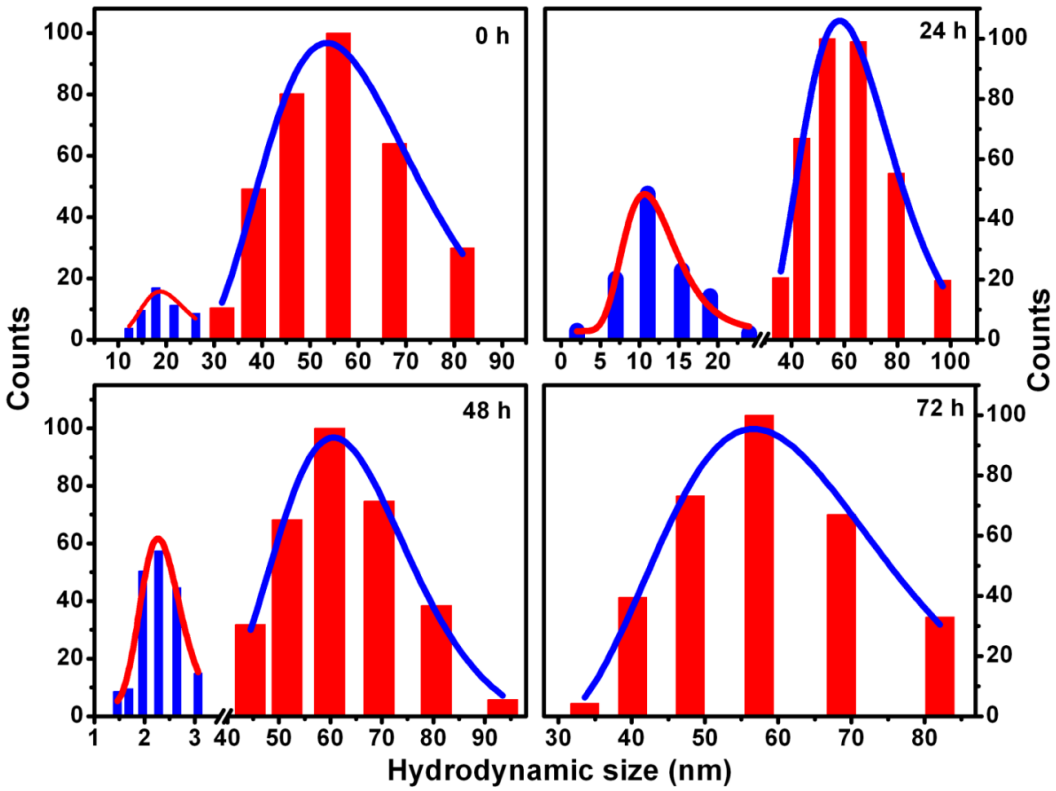

Fig. 3.18 Hydrodynamic particle size distributions of GNRs (prepared with gold seeds aged for 0-72 h) obtained from photon co-relation spectroscopy. Each histogram is fitted with lognormal particle size distribution function.

Table 3.7 Hydrodynamic size (D_{LSPR}-length; D_{TSPR}-diameters) of GNRs synthesized with gold seeds aged for 0-72 h.

Aging time (h)	**D_{LSPR} (nm)**	**D_{TSPR} (nm)**
0	18.7	53.2
24	11.6	58.4
48	07.8	60.1
72	57.4	-

3.2.3 Seedless Synthesis of GNRs

As the name suggests, seedless synthesis of GNRs is carried out without adding any seeds during the synthesis. In seedless synthesis technique the nucleation and the growth is coupled into a single step, with anisotropic growth occurring at the very beginning [5]. In this a method, GNRs are synthesized by adding $NaBH_4$ directly in to the growth solution containing gold precursor, silver ions, surfactant and the reducing agent [5, 31]. It is well-

known that $NaBH_4$ is a very strong reducing agent and can directly reduce Au(III) into Au(0) [32]. Addition of $NaBH_4$ into the growth solution is expected to form very small gold seeds, which are simultaneously used for the growth of GNRs in the seedless synthesis. It requires fewer synthesis steps and batch to batch variation caused by the temporal instability of the seeds in seeded approach can also be avoided. Amount of $NaBH_4$ added to the growth plays the similar role as that of seeds added to the growth solution in the seeded growth of GNRs.

The flow diagram for the seedless synthesis of GNRs is shown in **Fig. 3.19**. Protocols followed for the seedless synthesis of GNRs are summarized in **Annexure-I** section **A2**. To understand the effect of $NaBH_4$ on the synthesis of GNRs via seedless approach, optimized growth parameters obtained from seed-mediated synthesis of GNRs were used. To investigate the effect of $NaBH_4$ on the morphology of gold nanoparticles, volume of $NaBH_4$ (0.01 M) was varied from 1 µL to 100 µL.

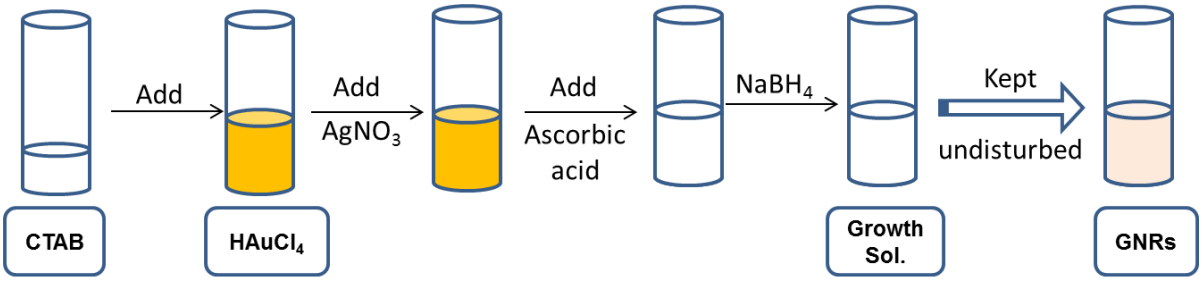

Fig. 3.19 Flow diagram of synthesis protocol followed for the preparation of GNRs by seedless synthesis.

UV-visible-NIR spectra of GNRs prepared with different volumes of $NaBH_4$ are shown in **Fig. 3.20**. Irrespective of the $NaBH_4$ volume, two surface plasmon bands are observed. LSPR band lies between 700 nm to 850 nm when $NaBH_4$ volume is 1-20 µL. It blue shifts when $NaBH_4$ volume is > 20 µL. No significant effect on TSPR band of GNRs is observed for $NaBH_4$ upto 50 µL. On addition of 100 µL $NaBH_4$; the growth solution immediately turned pink and then to ruby-red within 10-15 min. LSPR band disappeared and only single SPR band shouldered at 520 nm is observed (**Fig. 3.20**). This indicates that only spherical nanoparticles are formed when $NaBH_4$ volume is 100 µL.

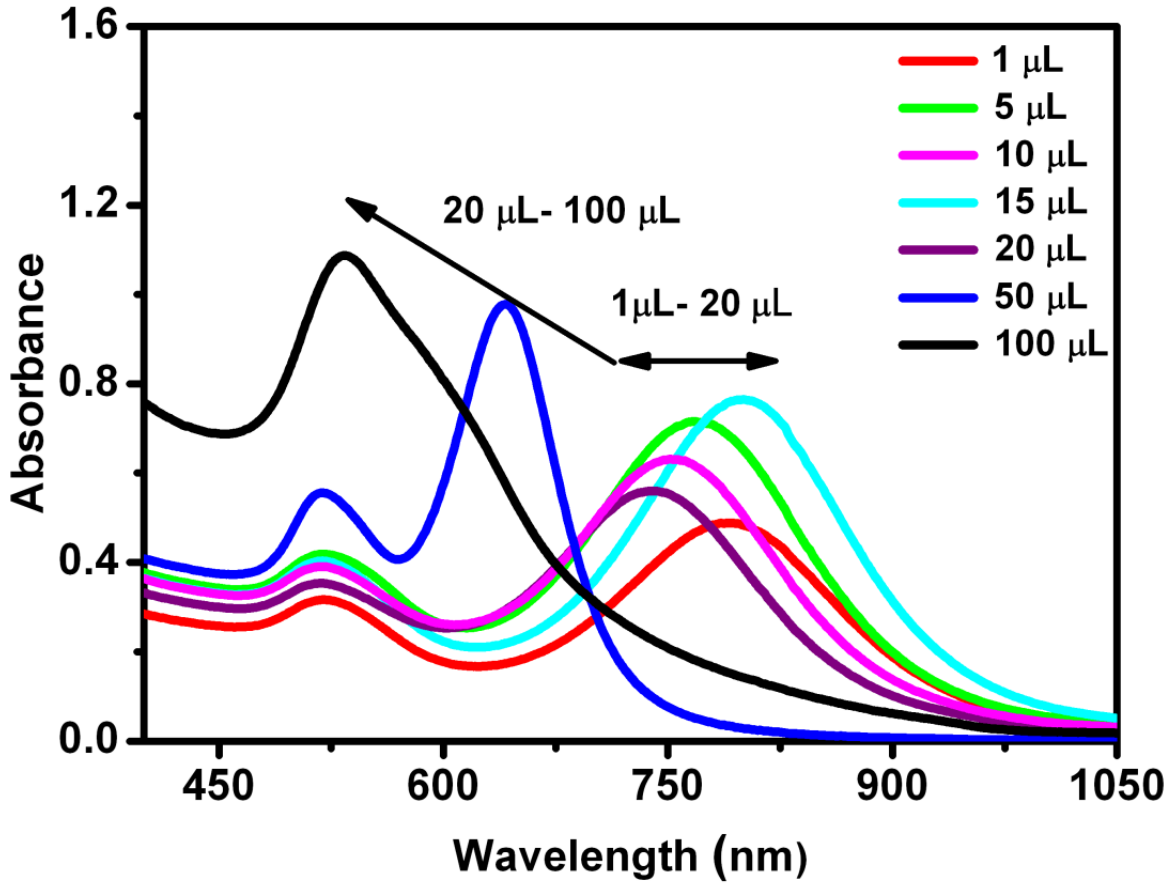

Fig. 3.20 UV-Visible spectra of GNRs prepared by seedless method with 1-100 µL $NaBH_4$.

TEM micrographs corresponding to gold nanoparticles prepared with 15 µL and 100 µL $NaBH_4$ were shown in (**Fig. 3.21**). TEM micrographs confirm the rod-like morphology of nanoparticles synthesized with 15 µL $NaBH_4$ (**Fig. 3.21 (a)**). This is consistent with the bimodal particle sized distribution obtained in photon-correlation spectroscopy (**Fig. 3.22**). TEM micrographs also confirm the formation of spherical nanoparticles (**Fig 3.21 (b)**) when 100 µL $NaBH_4$ is added to the growth solution as indicated by single SPR band in UV-Visible-NIR spectroscopy (**Fig. 3.20**). Formation of spherical gold nanoparticles is also evident from by the single particle size distribution observed in photon-correlation spectroscopy (**Fig 3.22)**. The variation in the hydrodynamic size of gold nanoparticles prepared with 1-100 µL $NaBH_4$ are summarized in **Table 3.8**.

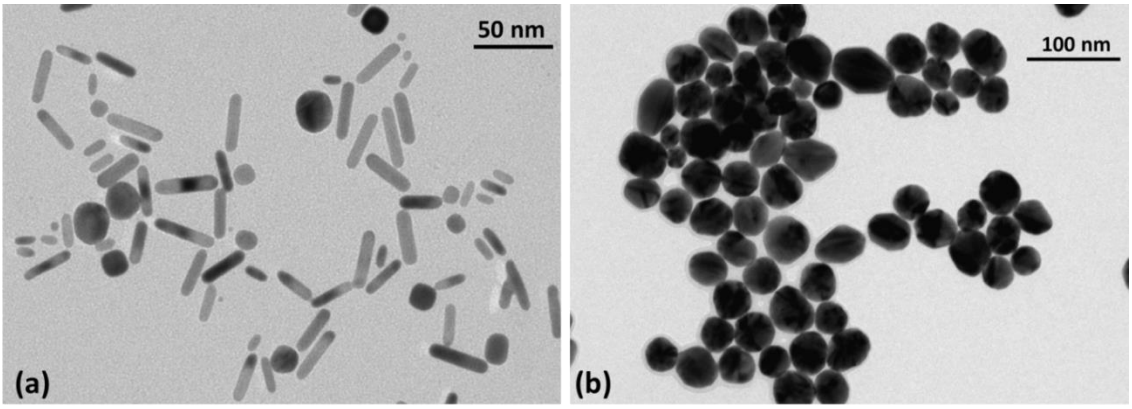

Fig. 3.21 TEM micrographs of gold nanoparticles prepared using (a) 15 µL and (b) 100 µL $NaBH_4$.

Table 3.8 Hydrodynamic size (D_{LSPR}-length; D_{TSPR}-diameter) of GNRs prepared with 1-100 µL $NaBH_4$.

$NaBH_4$ (µL)	**D_{LSPR} (nm)**	**D_{TSPR} (nm)**
1	28.2	202.7
5	22.6	180.9
10	30.0	228.0
15	25.3	195.8
20	37.1	206.1
50	22.4	174.9
100	118.5	-

3.2.4 Growth Mechanism of GNRs

Zipping Mechanism

The growth of GNRs depends on the crystallographic facets of the gold seed, relative size of the gold seed to the surfactant micelle and kinetics of surfactant adsorption on the facets of growing GNRs [33-35]. Small seed particles have FCC structure with icosahedron, decahedron, cuboctahedron and octahedron morphologies [36, 37]. Further, seeds having {100}/ {110} and {111} facets are necessary for directional growth of GNRs. The smaller seeds exhibiting crystalline facets enriched in {100} and {111} lead to nanorod growth [34]. The surface of the rod consists of four large {100} and {110} facets oriented parallel to the rod axis. The ends of the rod have {001} facet and four small {111} facets connecting the {110} and the {001} facets (**Fig 3.23**).

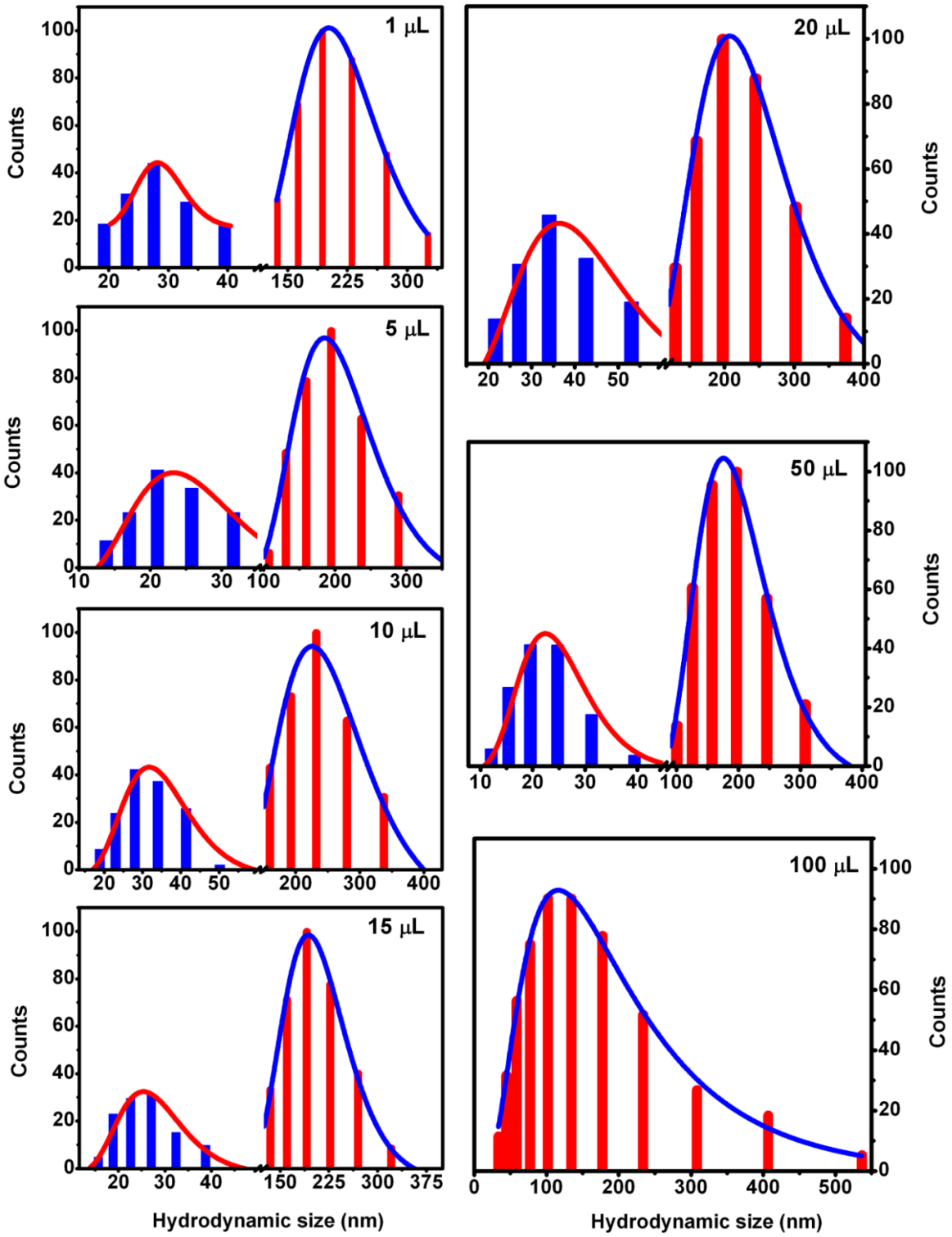

Fig. 3.22 Hydrodynamic particle size distributions of GNRs (prepared with 1-100 µL $NaBH_4$) obtained from photon co-relation spectroscopy. Each histogram is fitted with lognormal particle size distribution function.

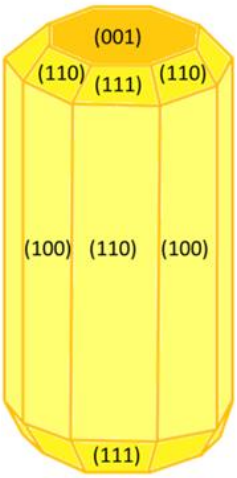

Fig. 3.23 Crystallographic facets of GNR.

According to the proposed zipping mechanism of GNRs growth, Ag^+ cations and $CTA^+–Br^-$ pairs are present in the growth medium [38]. The electrostatic interactions between Ag^+ cations and $CTA^+–Br^-$ pairs lead to the formation of $CTA^+–Br^-–Ag^+$ complex, which preferentially adsorb on the {100}/{110} facets as compared to the {111} facets. This is because of the large energy difference between the facets when considering the adsorption of group of surfactant micelles relative to a single micelle [34]. The surface adsorption energies of CTAB on Au crystal facets increase in the order of {110}, {100} and {111} [34, 35]. As the area of the facet is comparable to the size of a CTAB micelle (~2.9 nm), they adsorb rapidly on the {100} facets than the {111} [34]. Once a {100} facet is confined by CTAB micelle, it becomes an active center to induce aggregation of other micelles, resulting in the formation of a circular band of surfactant groups around the particle surface [39]. Particle growth become anisotropic; i.e. it grows faster along the exposed {111} facets at the bottom and top of the nanorod (**Fig. 3.24**). Thus the nanorods grow along their length, leading to increase in their aspect ratios. Surfactant adsorption along the growing rod side will continue to coalesce to form a dense bilayer [37]. In parallel as the {100} end facet become sufficiently large, the micelle adsorption and bilayer reorganization will take place at the edge of the rod [34]. This results into suppression of width followed by a slowing down in the growth along the length. The overall growth rate also slows down due to the consumption of gold precursor and ascorbic acid in the growth medium. The CTAB micelles will continue to coalesce and rearrange on the GNR surface to form defect free flat bilayers which finally results in smoother faceted GNRs [34].

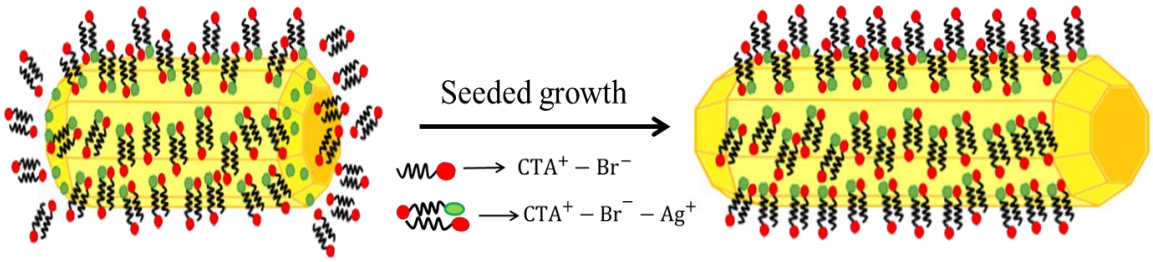

Fig. 3.24 Schematic representation of zipping mechanism responsible for anisotropic nanorod growth.

3.3 SYNTHESIS OF GOLD NANOPLATES (GNPs)

3.3.1 Seed-Mediated Synthesis of GNPs

Synthesis of GNPs was carried out by replacing CTAB surfactant with biocompatible tri-block copolymer, pluronic F-127. Pluronic F-127 acts as reducing, growth directing and stabilizing agent [10]. Pluronic F-127 possesses excellent biocompatibility [40]. It binds to the surface of metal nanoparticles and forms a film by hydrophobic interactions through polypropylene oxide block of the copolymer and controls the growth of GNPs [41].

Seed-mediated synthesis designed for GNRs in the previous sections is employed in this study, too. In a typical synthesis of GNPs, molar concentrations and volumetric ratios of all the ingredients (gold source, $AgNO_3$, ascorbic acid, seed) were optimized from those used in the synthesis of GNRs using CTAB. The only difference is the type of surfactant used. CTAB is replaced by equimolar concentration of pluronic F-127. Protocols followed for the seed-mediated synthesis of GNPs are summarized in **Annexure-I** section **A3**.

UV-Visible-NIR spectra of as-synthesized GNPs are shown in **Fig. 3.25 (**red line**)**. Two distinct plasmon resonance bands are observed indicating the growth of anisotropic nanostructures of gold [35]. The first plasmon band at 526 nm corresponds to out-of-plane and second plasmon band at 810 nm corresponds to in-plane oscillations of electrons in GNPs. Black line in **Fig. 3.25** indicates the UV-Visible-NIR spectra of gold seeds. A shoulder centered at 510 nm is a typical character of small Au seeds. Anisotropic morphology of as-synthesized GNPs is further confirmed by photon-correlation spectroscopy (**Fig. 3.26)**. Two distinct size distributions are observed. The mean hydrodynamic size of

GNPs along their short axis is 15.1 nm and along their long axis is 73.9 nm. TEM images of these nanoparticles confirm their plate-like morphology (**Fig. 3.27**).

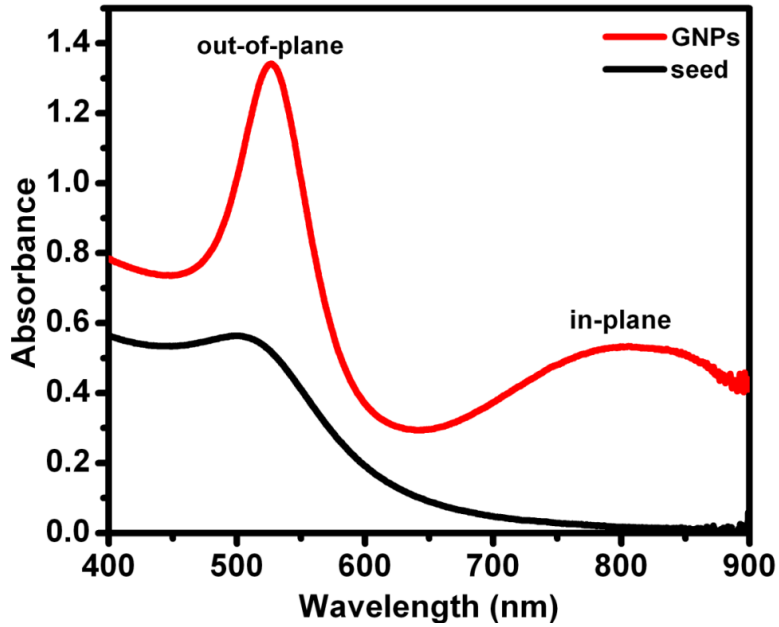

Fig. 3.25 UV-Vis-NIR spectra of gold seeds and gold nanoparticles. Two distinct plasmon bands centered at 526 nm and 810 nm corresponds to the out-of-plane and in-plane oscillations indicating the formation of anisotropic GNPs.

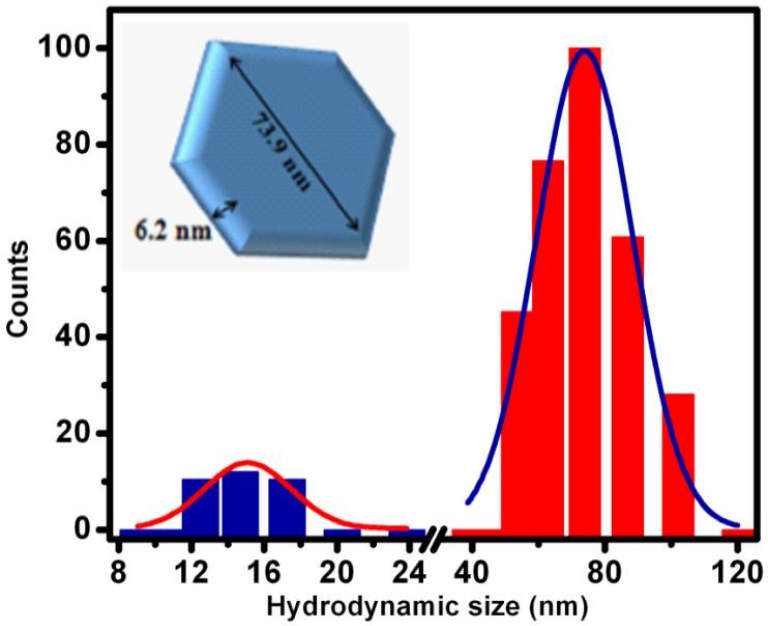

Fig. 3.26 Hydrodynamic particle size distribution fitted with log normal particle size distribution of GNPs.

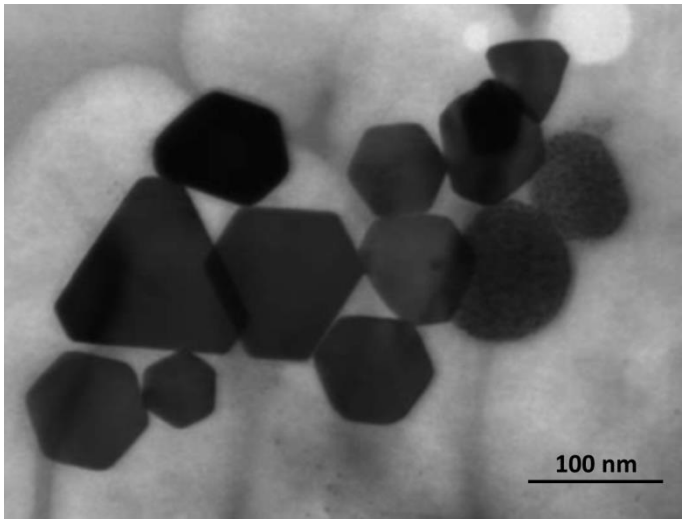

Fig. 3.27 Representative TEM micrograph of GNPs prepared with 1 mM pluronic F-127. Well faceted hexagonal plates, triangular plates and truncated triangles are observed whose size ranges from 46.5 nm to 108 nm.

3.3.2 Growth Mechanism of GNPs

The growth mechanism of anisotropic gold nanostructures, specifically GNPs is of great concern as very limited information is available about this aspect. The growth mechanism of GNPs with pluronic as shape directing agents is yet to be established. The role of 'seeds' and the capping agents in the growth of gold nanoparticles is discussed in literature [34]. Many groups [4, 6, 10] have shown that by using growing seeds in solutions containing surfactant micelles, nanoparticles with well-defined shapes could be obtained. The growth rate of nanoparticles is often controlled kinetically rather than thermodynamically by different sticking probabilities of atoms on different crystallographic facets [42]. Being of lowest surface energy, the (111) face of the FCC metal has the lowest sticking probability as compared to other faces (γ (110) > γ (100) > γ (111)) [43]. Thus FCC metal has the highest energy to nucleate and grow into the nanoparticles with their surfaces bounded by (111) facets in wet chemical synthesis [43].

At a specific pluronic F-127/$HAuCl_4$ molar ratio, the hydrophobic polypropylene oxide (PPO) preferentially adsorbed on {111} planes of FCC Au nuclei, inhibiting the growth on {111} crystallographic planes, and promotes anisotropic growth along the {110} facets [44]. Under ideal conditions, the nuclei grow uniformly along the six <110> directions if the growth environment is uniform, resulting in the formation of hexagonal plate

surrounded by three pairs of {110} lateral faces (**Fig. 3.28**). However, due to local fluctuations in the growth medium, the crystal growth deviate from uniform growth along <110> direction. Therefore, triangular and truncated triangular (**Fig. 3.28**) plates will be formed if the nuclei are grown along <110> directions at different rates [45]. TEM images of hexagonal nanoplates, triangular nanoplates and truncated triangular nanoplates are also shown in **Fig. 3.27**.

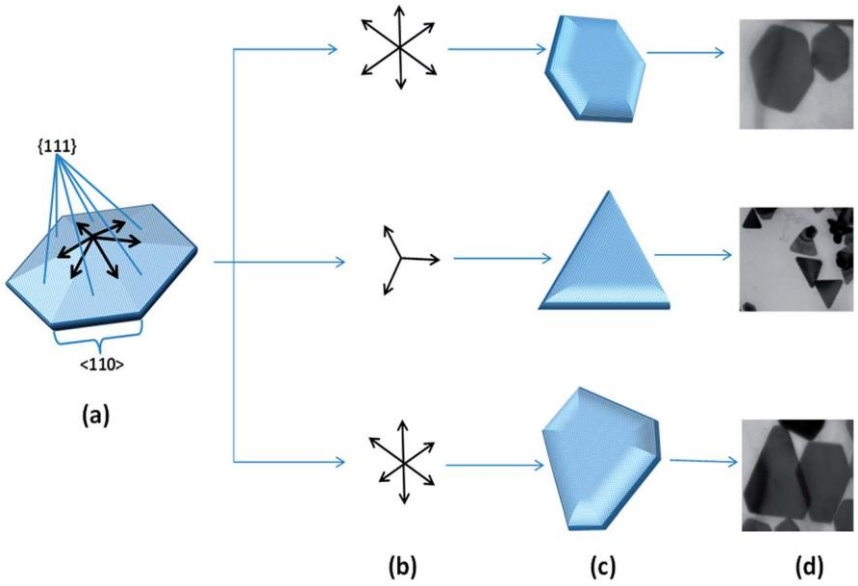

Fig. 3.28 Schematic illustration of proposed growth mechanism of GNPs: (a) crystallographic facets with basal {111} plane and <110> side facet, (b) the formation of hexagonal plate, triangular plate and truncated triangular plate like structures along the <110> directions, (c) the expected particles shapes and (d) representative TEM images of hexagonal nanoparticles, triangular nanoparticles, and truncated triangular nanoparticles.

3.3.3 Seedless Synthesis of GNPs

Unlike seedless synthesis of GNRs, seedless synthesis of GNPs was also carried out by carefully varying the $NaBH_4$ concentration in the growth solution. To investigate the effect of $NaBH_4$ on the plasmonic properties and morphology of GNPs, volume of $NaBH_4$ (0.01 M) was varied from 1 µL to 100 µL. Rest of the experimental conditions were kept unchanged as per seedless synthesis of GNRs. Protocols followed for the seedless synthesis of GNPs are summarized in **Annexure-I** section **A4**.

UV-Visible-NIR spectra of as-synthesized GNPs are shown in **Fig. 3.29**. Depending on the synthesis protocols two or more plasmon bands are expected for GNPs. Single SPR

band is observed in the UV-Visible-NIR spectra of the gold nanoparticles. It is centered at 520 nm for 1, 5, 20, 50 and 100 µL $NaBH_4$. This indicates that only spherical nanoparticles are formed in these cases. An additional broad band centered between 750 nm to 1100 nm is only observed in samples prepared with 10 µL and 15 µL $NaBH_4$. Two distinct plasmon resonance bands indicate the growth of anisotropic nanostructures of gold [35]. The first plasmon band at 526 nm corresponds to out-of-plane and second broad plasmon band corresponds to in-plane oscillations of electrons in nanoplates.

Anisotropic characteristics of as-synthesized GNPs corresponding to 10 µL and 15 µL $NaBH_4$ are further confirmed by their photon-correlation spectroscopy (**Fig. 3.31**). Two distinct size distributions are observed which are corresponds to the different diffusion coefficients of GNPs along their long and short axis. These bimodal hydrodynamic size distributions of GNPs further support our claim in UV-Vis-NIR spectroscopy that as-synthesized gold nanoparticles have plate like asymmetric morphology. TEM micrograph of gold nanoparticles prepared with 15 µL $NaBH_4$ show plate-like morphology (**Fig. 3.30**). Large number of spherical nanoparticles is also formed along with GNPs.

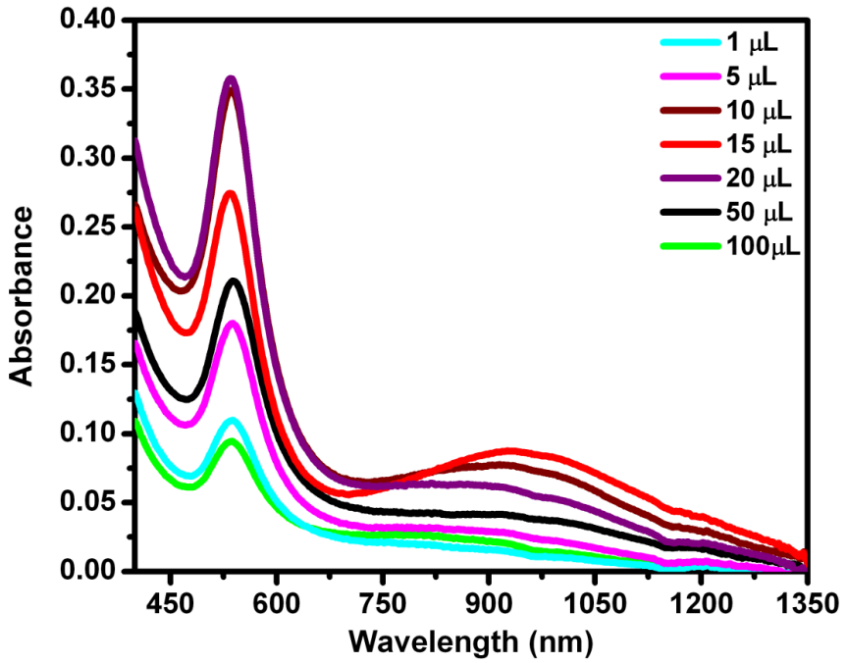

Fig. 3.29 UV-Visible-NIR spectra of GNPs prepared with 1-100 µL $NaBH_4$.

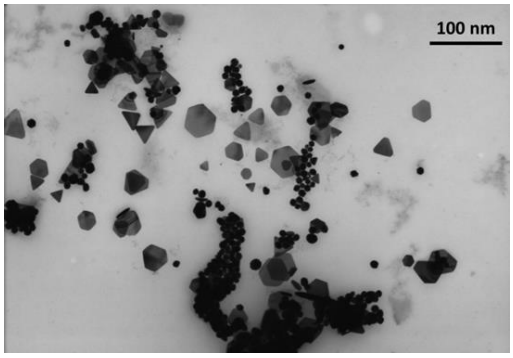

Fig. 3.30 TEM micrograph of gold nanoparticles prepared with 15 µL $NaBH_4$ by seedless approach.

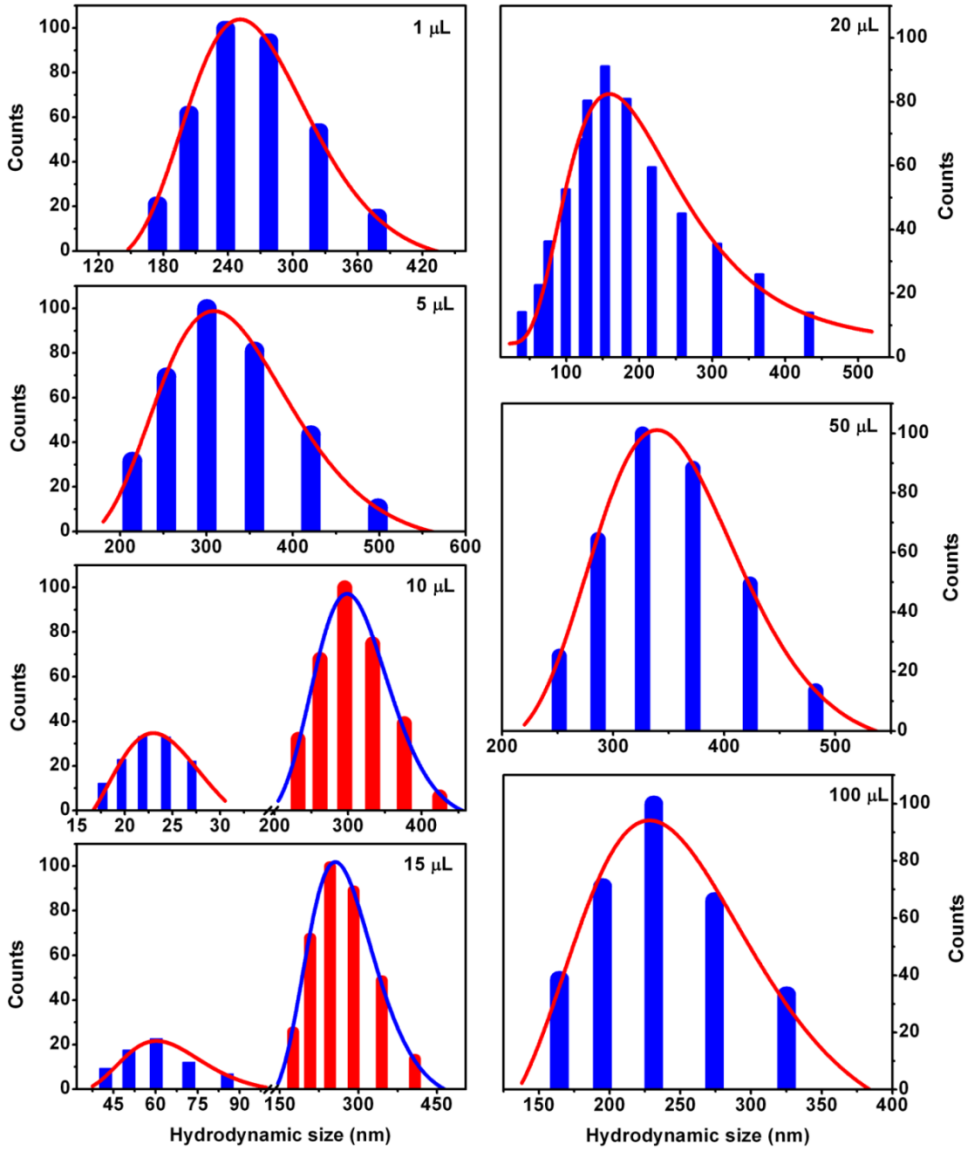

Fig. 3.31 Hydrodynamic particle size distributions of GNPs obtained from photon co-relation spectroscopy. Each histogram is fitted with lognormal particle size distribution function.

References:

1. X. Huang, S. Neretina, M.A. El-Sayed, *Adv. Mater*., **2009**, 21, 4880–4910.
2. J. P´erez-Juste, I. Pastoriza-Santos, L.M. Liz-Marz´an, P. Mulvaney, *Coord. Chem. Rev.*, **2005**, 249, 1870–1901.
3. N.R. Jana, L. Gearheart, C.J. Murphy, *J. Phys. Chem. B*, **2001**, 105, 4065-4067.
4. B. Nikoobakht, M.A. El-Sayed, *Chem. Mater.*, **2003**, 15, 1957-1962.
5. X. Xu, Y. Zhao, X. Xue, S. Huo, F. Chen, G. Zou, X.-J. Liang, *J. Mater. Chem. A*, **2014**, 2, 3528–3535.
6. N.R. Jana, *Small*, **2005**, 1, 875-882.
7. L.J. Sherry, R. Jin, C.A. Mirkin, G.C. Schatz, R.P.V. Duyne, *Nano Lett*., **2006**, 6, 2060–2065.
8. J.E. Millstone, S.J. Hurst, G.S. M´etraux, J.I. Cutler, C.A. Mirkin, *Small*, **2009**, 5, 646–664.
9. Y. Lin, A. Paschalis, *J. Phys. Chem. B*, **2002**, 106, 10834–10844.
10. T. Sakai, P. Alexandridis, *Langmuir*, **2004**, 20, 8426–8430.
11. K.R. Brown, D.G. Walter, M. Natan, *J. Chem. Mater*., **2000**, 12, 306-313.
12. S. Bakshi, I. Kaur, *Colloid Polym. Sci.*, **2003**, 281, 928-934.
13. B. Nikoobakht, M.A. El-Sayed, *Langmuir*, **2001**, 17, 6368-6374.
14. O.R. Miranda, N.R. Dollahon, T.S. Ahmadi, *Cryst. Growth Des.*, **2006**, 6, 2747–2753.
15. N.R. Jana, L. Gearheart, C.J. Murphy, *Langmuir*, **2001**, 17, 6782-6786.
16. S.B. Velegol, B.D. Fleming, S. Biggs, E.J. Wanless, R.D. Tilton, *Langmuir*, **2000**, 16, 2548-2556.
17. S.K. Kang, S. Chah, C.Y. Yun, J. Yi, *Korean J. Chem. Eng*., **2003**, 20, 1145-1148.
18. G. Montalvo, M. Valiente, E. Rodenas, *J. Colloid Interface Sci*., **1995**, 172, 494-501.
19. S. Koeppl, C. Solenthaler, W. Caseri, R. Spolenak, *J. Nanomater*., **2011**, 515049, 1-13.
20. J.A. Edgar, A.M. McDonagh, M.B. Cortie, *ACS Nano*, **2012**, 6, 1116−1125.
21. L. Scarabelli, A.S.-Iglesias, J.P.-Juste, L.M. Liz-Marzán, *J. Phys. Chem. Lett*., **2015**, 6, 4270–4279.
22. J.R.-Fernández, J.P.-Juste, P. Mulvaney, L.M. Liz-Marzán, *J. Phys. Chem. B*, **2005**, 109, 14257−14261.
23. C.J. Ward, R. Tronndorf, A.S. Eustes, M.L. Auad, E.W. Davis, *J. Nanomater.*, **2014**, 765618, 1-7.
24. L. Vigderman, E.R. Zubarev, *Chem. Mater*., **2013**, 25, 1450−1457.
25. J.D.S. Newman, G. J. Blanchard, *Langmuir*, **2006**, 22, 5882−5887.
26. W.A.E. McBryde, J.H. Yoe, *Anal. Chem*., **1948**, 20, 1094-1099.
27. J. Heintzenberg, *Aerosol Sci Technol*., **1994**, 21, 46-48.
28. L. Gou, C.J. Murphy, *Chem. Mater*., **2005**, 17, 3668–3672.
29. Y. Ying, S.-S. Chang, C.-L. Lee, C.R.C. Wang, *J. Phys. Chem. B*, **1997**, 101, 6661–6664.
30. F. Kim, J.H. Song, P. Yang, *J. Am. Chem. Soc.*, **2002**, 124, 14316–14317.
31. B.K. Jena, C.R. Raj, *Chem. Mater*., **2008**, 20, 3546–3548.
32. M.R.K. Ali, B. Snyder, M.A. El-Sayed, *Langmuir*, **2012**, 9807–9815.
33. R. Becker, B. Liedberg, P.O. Kall, *J. Colloid Interface Sci.*, **2010**, 343, 25-30.

34. K. Park, L.F. Drummy, R.C. Wadams, H. Koerner, D. Nepal, L. Fabris, R.A. Vaia, *Chem. Mater*., **2013**, 25, 555-563.
35. E.S. Pagac, D.C. Prieve, R.D. Tilton, *Langmuir*, **1998**, 14, 2333-2342.
36. M. Grzelczak, J. Pe´rez-Juste, P. Mulvaney, L.M. Liz-Marza´n, *Chem. Soc. Rev*., **2008**, 37, 1783-1791.
37. Y. Wang, S. Teitel, C. Dellago, *Nano Lett*., **2005**, 5, 2174-2178.
38. F. Hubert, F. Testard, A. Thill, Q. Kong, O. Tache, O. Spalla, *Cryst. Growth Des*., **2012**, 12, 1548-1555.
39. G. Grochola, I.K. Snook, S.P.J. Russo, *Chem. Phys*., **2007**, 127, 194707-194713.
40. L. Yang, P. Alexandridis, *Curr. Opin. Colloid Interface Sci*., **2000**, 5, 132–143.
41. T.I. Abdullin, O.V. Bondar, Y.G. Shtyrlin, M. Kahraman, M. Culha, *Langmuir*, **2010**, 26, 5153–5159.
42. N.R. Jana, L. Gearheart, C.J. Murphy, *Adv. Mater*., **2001**, 13, 1389–1393.
43. J.M. Zhang, F. Ma, K.W. Xu, *Appl. Surf. Sci*., **2004**, 229, 34–42.
44. J. Feng, R.B. Pandey, R.J. Berry, B.L. farmer, R.R. Naik, H. Heinz, *Soft Matter*, **2011**, 7, 2113–2120.
45. C. Kan, X. Zhu, G. Wang, *J. Phys. Chem. B*, **2006**, 110, 4651–4656.

CHAPTER 4

TUNABILITY OF GOLD NANOSTRUCTURES

4.1 INTRODUCTION

Gold nanostructures can be used in applications like bio-imaging, chemical sensing, plasmon resonance spectroscopy, photonics, optoelectronics, therapeutics and diagnosis etc. due to their tuneable plasmonic properties [1, 2]. The extent to which the surface plasmon resonance (SPR) of gold nanostructures can be tuned depends on the size and shape of the nanoparticles as well as on the dielectric constant of the medium [2-4]. SPR band of gold nanostructures red shifts into the NIR region when their aspect ratio increases beyond one [5]. For *in-vivo* biomedical applications, metal nanoparticles with SPR band in the NIR region (750−1300 nm) are desirable as the body tissues, blood and water are transparent to IR radiations [1-3]. They absorb heavily in the visible region of electromagnetic spectrum.

Tunability of plasmonic properties of gold nanostructures can be obtained by various means both in the seed-mediated and seedless growth approaches. Murphy and co-workers and El-Sayed and co-workers have pioneered a seed-mediated method for the synthesis of GNRs by using CTAB as growth directing agent [6, 7]. Several modifications in this protocol have been proposed by various groups to tailor their LSPR band [8, 9]. GNRs with tuneable LSPR band can be prepared either with co-surfactants or by following three-step seeded growth in silver-free system [6, 7]. Although seed-mediated method is simple and economical and produces GNRs with smooth morphology; it has several limitations: (i) Reproducibility is poor [10, 11], (ii) ripening of seeds over extended period does not form GNRs [11], (iii) aspect ratio of GNRs is low (between 2-5) with LSPR band < 850 nm in single surfactant system [6], (iv) poor quality and low yield in multi-surfactant system (formation of dog-bone or dumbbell shaped nanoparticles) [12, 13], etc.

To control the growth of GNRs, variety of additives such as acetone [12], Na_2S [14], hydrochloric acid [15], nitric acid [11], cyclohexane [12], iodide ions [16], copper ions [17], bromide ions [18], etc. have been introduced into the growth solution to regulate the aspect ratio and tune the LSPR band of GNRs. These approaches led to the formation of GNRs with corrugated surfaces. Several other strategies like replacing H_2O with D_2O and ascorbic acid

with hydroquinone [19], use of aromatic additives [20] and binary surfactant mixtures [21] have also been found effective in tuning the LSPR band of GNRs.

Recently, a seedless growth technique has been developed where the nucleation and growth stages are coupled and proceeds simultaneously [22]. In this method, GNRs are synthesized by directly adding $NaBH_4$ in the growth solution containing gold ion precursor, silver ions, CTAB and ascorbic acid [22]. El. Sayed et al. synthesized small GNRs by optimizing the $NaBH_4$ and CTAB concentrations and pH of the growth solution [23]. Zhang et al. used various phenols as reducing agents and systematically varied the $NaBH_4$ and CTAB concentrations to obtain GNRs with LSPR band tuned from 550 nm to 1000 nm [5]. C. Wang et al. have produced GNRs with miscellaneous shapes like peanut, dog-bone and rectangle outlines and branched multipods with ribbed surface by controlling the pH of the growth solution [8]. Zhu and co-workers used HCl to drive the formation of GNRs with LSPR band tuned upto 1000 nm [24]. They ended with low yield of gold conversion and formation of various other shapes. To the best of our knowledge, role of pH in tuning the LSPR band of GNRs in seedless synthesis involving binary co-surfactant system of BDAC-CTAB have not been investigated. We have designed a pH controlled seedless synthesis of GNRs in BDAC-CTAB co-surfactant system with tuneable LSPR band upto 1300 nm. Systematic study is carried out to understand the role of co-surfactants and pH in the regulation of dimension and thus the plasmonic properties of GNRs synthesized by single-step seedless approach.

Limited reports are available on the tunability of SPR band of GNPs in literature. GNPs have been synthesized with tuneable plasmonic properties. Effect of synthesis method (seeded and seedless) and growth parameters on the dimensional and optical tunability of GNRs and GNPs have been studied in the chapter.

4.2. TUNABILITY OF GNRs

4.2.1. Seed-Mediated Tunability of GNRs Synthesized by BDAC-CTAB Co-Surfactant System

To synthesize GNRs with tuneable LSPR band in the NIR region by seed-mediated method, synthesis protocols developed by El-Sayed et al. [7] is followed. Schematic of flow diagram

of synthesis protocol for seed-mediated synthesis of GNRs with BDAC-CTAB binary co-surfactant is summarized in **Fig. 4.1** and described in **Annexure-I** at **A5**.

UV-Visible-NIR absorption spectra of GNRs synthesized by seed-mediated method using BDAC-CTAB co-surfactant system is shown in **Fig 4.2 (a)**. Each spectrum was recorded after every sequential addition of growth solution. LSPR band of GNRs red shifts by 30-40 nm every time a secondary growth solution was added. The LSPR band of as-synthesized GNRs is 920 nm which red shifted to 1150 nm after 16 successive additions of the secondary growth solution. The growth of GNRs saturates after 16 successive additions of secondary growth solution. No shift in the LSPR band was observed on further addition of secondary growth solution (**Fig. 4.2 (a)**). A representative TEM micrograph of GNRs obtained by seeded growth is shown in **Fig. 4.2 (b)**. Large number of spherical gold nanoparticles was observed along with broad size distribution of nanorods in the TEM micrographs. These results are similar to those reported in literature [4, 5]. Too many steps and laborious separation process makes seeded growth process lengthy and difficult to reproduce.

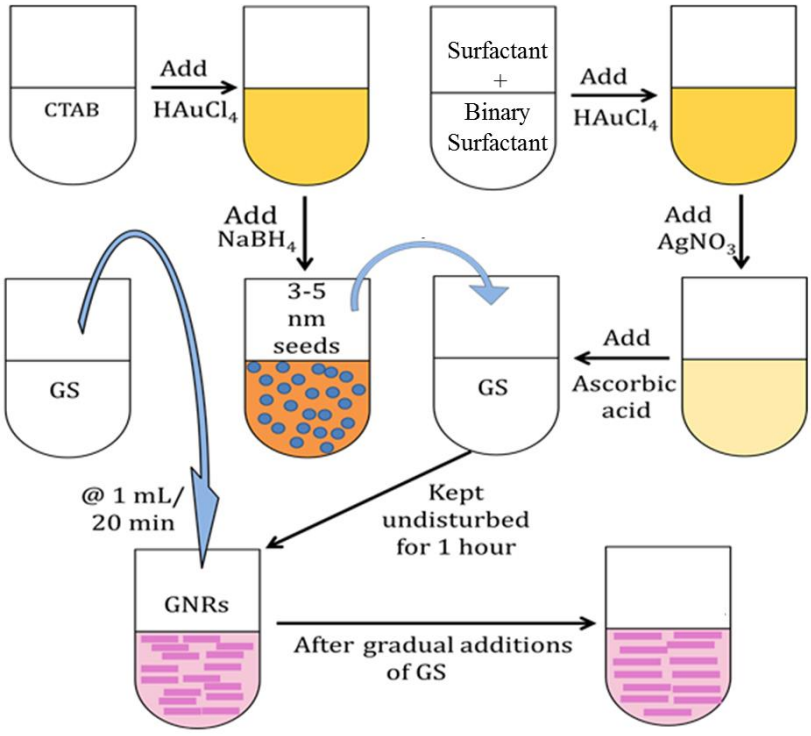

Fig. 4.1 Schematic flow diagram of synthesis protocols for seed-mediated synthesis of GNRs by BDAC-CTAB Co-Surfactant.

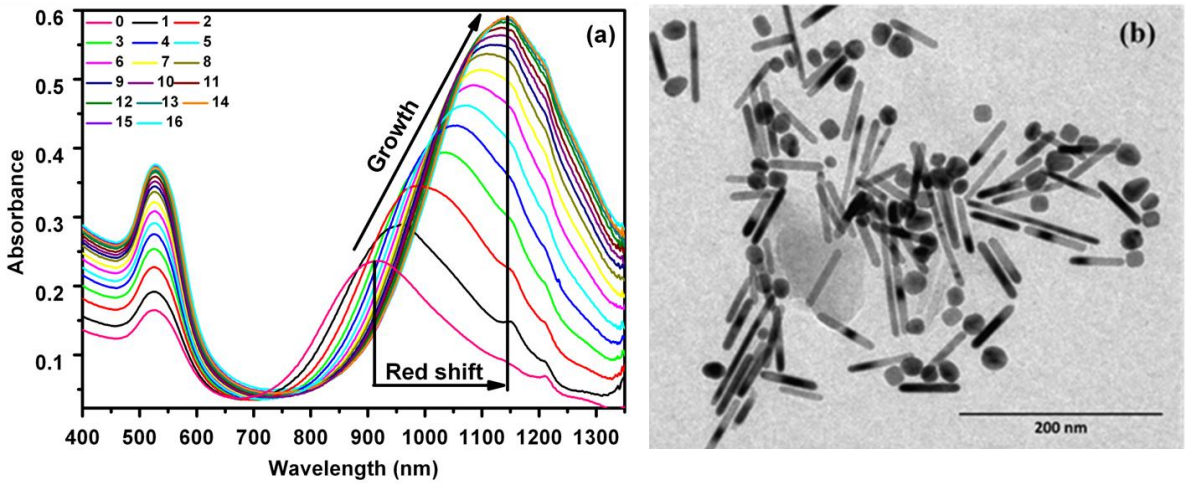

Fig. 4.2 (a) UV-Visible absorption spectra of GNRs synthesized by seed-mediated method by serial addition of secondary growth solution in sixteen steps. (b) TEM micrograph of as-synthesized GNRs prepared by serial addition of secondary growth solution in seed-mediated synthesis.

4.2.2 pH Controlled Tunability of GNRs Synthesized by Seedless Approach Using BDAC-CTAB Co-Surfactant System

To overcome the drawbacks of limited tunability and poor yield of GNRs obtained in seeded growth technique, Min Gu et al. [22] have proposed a seedless method of GNRs synthesis. It is a single-step synthesis process in which LSPR band can be tuned from visible to NIR region with improved yield. It requires fewer synthesis steps and batch to batch variation caused by the temporal instability of the seeds in seeded approach can be avoided. Seedless approach was previously attempted only in CTAB system. We have established here protocols for seedless synthesis of GNRs in BDAC-CTAB binary co-surfactant system. Effect of pH on the optical tunability of LSPR band of GNRs synthesized by seeded growth is known [11, 15]. However, no such study on pH controlled optical tunability of LSPR band of GNRs via seedless synthesis in BDAC-CTAB binary co-surfactant system have been reported so far.

Protocol for pH controlled seedless synthesis of GNRs with BDAC-CTAB binary co-surfactant is summarized in **Fig. 4.3** and described in **Annexure-I** section **A6**. Photographic view of colloidal dispersion of GNRs prepared at different pH is shown in **Fig. 4.4**. The difference in color of the colloids themselves indicates that the synthesized GNRs have different aspect ratios.

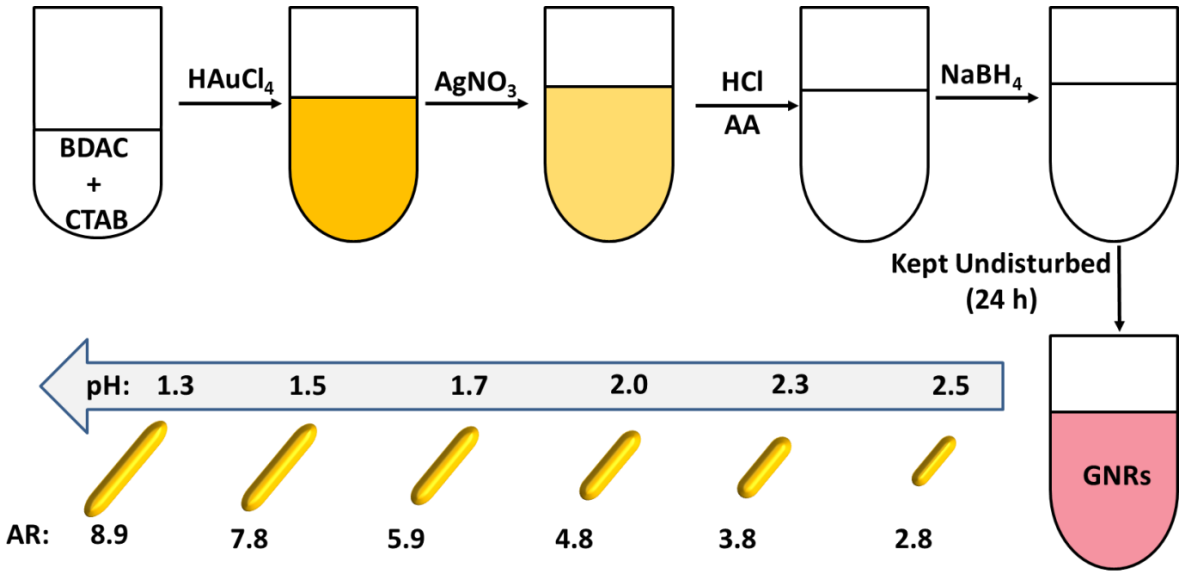

Fig. 4.3 Schematic representation of pH controlled seedless synthesis of GNRs in BDAC-CTAB binary co-surfactant system. GNRs with tuneable aspect ratio from 2.8 to 8.9 were synthesized by regulating the pH of the growth solution from 2.5 to 1.3.

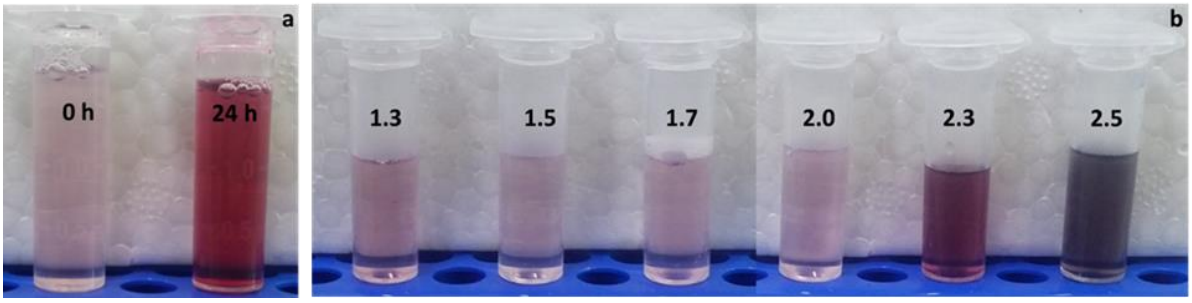

Fig. 4.4 (a) Photographic view of colloidal suspension of GNRs. Colloid color changes from pink to dark red in 24 h, indicating GNRs growth. (b) Photographic view of colloidal suspension of GNRs synthesized at different reaction pH (1.3, 1.5, 1.7, 2.0, 2.3 and 2.5) for comparison they are diluted to same concentration.

The reaction kinetics of GNRs in seedless synthesis was controlled by regulating the pH of the growth solution. Initial pH of the growth solution lies between 3.50-3.70. At this pH, reaction proceeds swiftly on addition of $NaBH_4$; turning the growth solution to light golden brown. Within few minutes it turned dark pink and then to violet in 4-5 h, confirming the formation of gold nanoparticles. UV-Visible-NIR absorption spectra of gold nanoparticles synthesized at pH 1.3-3.5 were shown in **Fig. 4.5**.

A single SPR band at 525 nm was observed in the UV-Visible spectra of gold nanoparticles synthesized at pH 3.5. It is due to the formation of spherical nanoparticles. This is in good agreement with those already reported in the literature [6]. On reducing the pH of

the growth solution from 3.5 to 3.0 (by addition of 1 µL HCl) the color of the growth solution rapidly turned golden brown when $NaBH_4$ was added to it. Solution color then turned to pink in 3-4 h. A single SPR band centred at 525 nm was again observed in the UV-Visible-NIR absorption spectrum of these nanoparticles (**Fig. 4.5**). This suggests that at pH 3.0 also only spherical nanoparticles are formed.

When the reaction pH of the growth solution was reduced to 2.5 (by adding 3 µL HCl), the color of the growth solution changes gradually upon addition of $NaBH_4$, indicating the decrease in the rate of reaction. The UV-Visible-NIR absorption spectrum of as synthesized colloid show two distinct plasmon resonance bands centred at 712 nm and 512 nm (**Fig. 4.5**). Hence, synthesized colloid may contain GNRs, which was confirmed by transmission electron microscopy (**Fig. 4.5**).

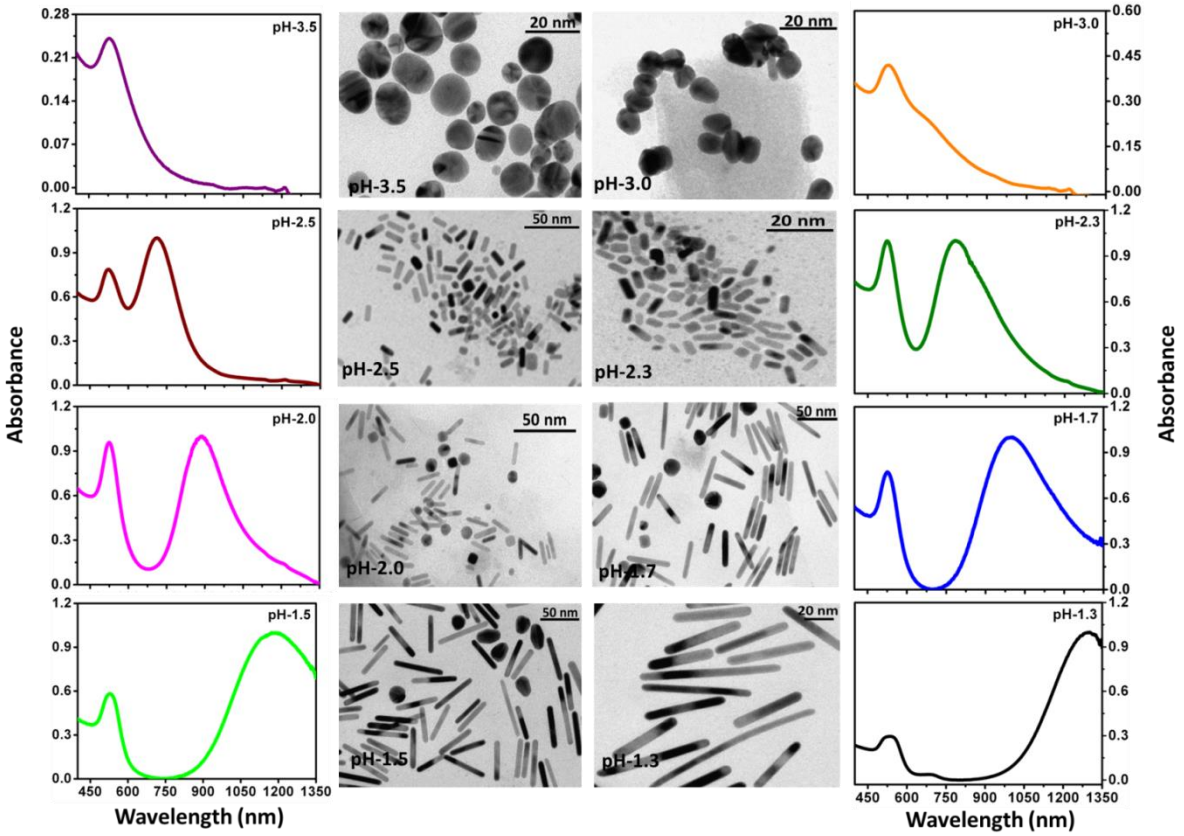

Fig. 4.5 TEM micrographs and corresponding UV-Visible-NIR spectra of GNRs prepared by seedless approach at pH 1.3-3.5.

The average dimensions of GNRs along with their aspect ratios synthesized at pH 1.3-2.5 are reported in **Table 4.1**. Aspect ratio of GNRs can also be estimated from the

discrete dipole approximation (DDA) [25]. Aspect ratio of GNRs obtained from this approximation is also shown in **Table 4.1**. These values are in good agreement with those obtained from TEM microscopy. Both the average length and the aspect ratio of GNRs increase linearly with decrease in the pH of the growth solution (**Fig. 4.6**). GNRs synthesized at pH 1.3 have maximum aspect ratio of 8.9 which is highest amongst the synthesized GNRs. The LSPR band of GNRs shifts from 712 nm (for pH 2.5) to 1295 nm (for 1.3) with increase in the aspect ratio from 2.8 to 8.9. LSPR band could not be increased beyond 1295 by further decreasing the pH of the growth solution. This is due to the gelation of growth solution when pH of the growth solution is reduced below 1.3.

Table 4.1 Effect of pH on the dimension, aspect ratio and LSPR band positions of GNRs synthesized at pH 1.30-2.50.

pH	HCl (µL)	Average length (nm)	Average diameter (nm)	Aspect ratio		λ_{LSPR} (nm)
				TEM	DDA	
1.30	110	66.66±2.41	7.44±0.05	8.9	9.1	1295
1.50	75	60.15±0.32	7.62±0.04	7.8	7.9	1182
1.70	30	47.13±0.41	7.89±0.06	5.9	5.9	992
2.00	10	30.12±0.54	6.20±0.03	4.8	4.9	889
2.30	5	24.21±0.62	6.29±0.02	3.8	3.8	787
2.50	3	15.97±0.35	5.70±0.03	2.8	3.0	712

LSPR band position of GNRs depends on the aspect ratios of nanorods [8], which in turn depends on the growth kinetics in the solution. Growth rate of GNRs synthesized by seedless approach depends on surfactant type, concentration of the reducing agent, reaction temperature and time, pH of the growth solution, etc. [26, 27]. It has been reported in the literature that decreasing the pH reduces the growth rate of GNRs, which is helpful in increasing the aspect ratio of GNRs and in turn tune the LSPR band of GNRs too [27]. The growth of GNRs saturates within 2h when the pH of the growth solution is 2.5 while it takes 14 h for growth to saturate when the pH of the growth solution is 1.5 (**Fig. 4.7**). The saturation time of growth of GNRs as the function of the pH of the growth solution is plotted in **Fig. 4.8**. It is observed that the growth rate of GNRs decreases with the decreases in the pH.

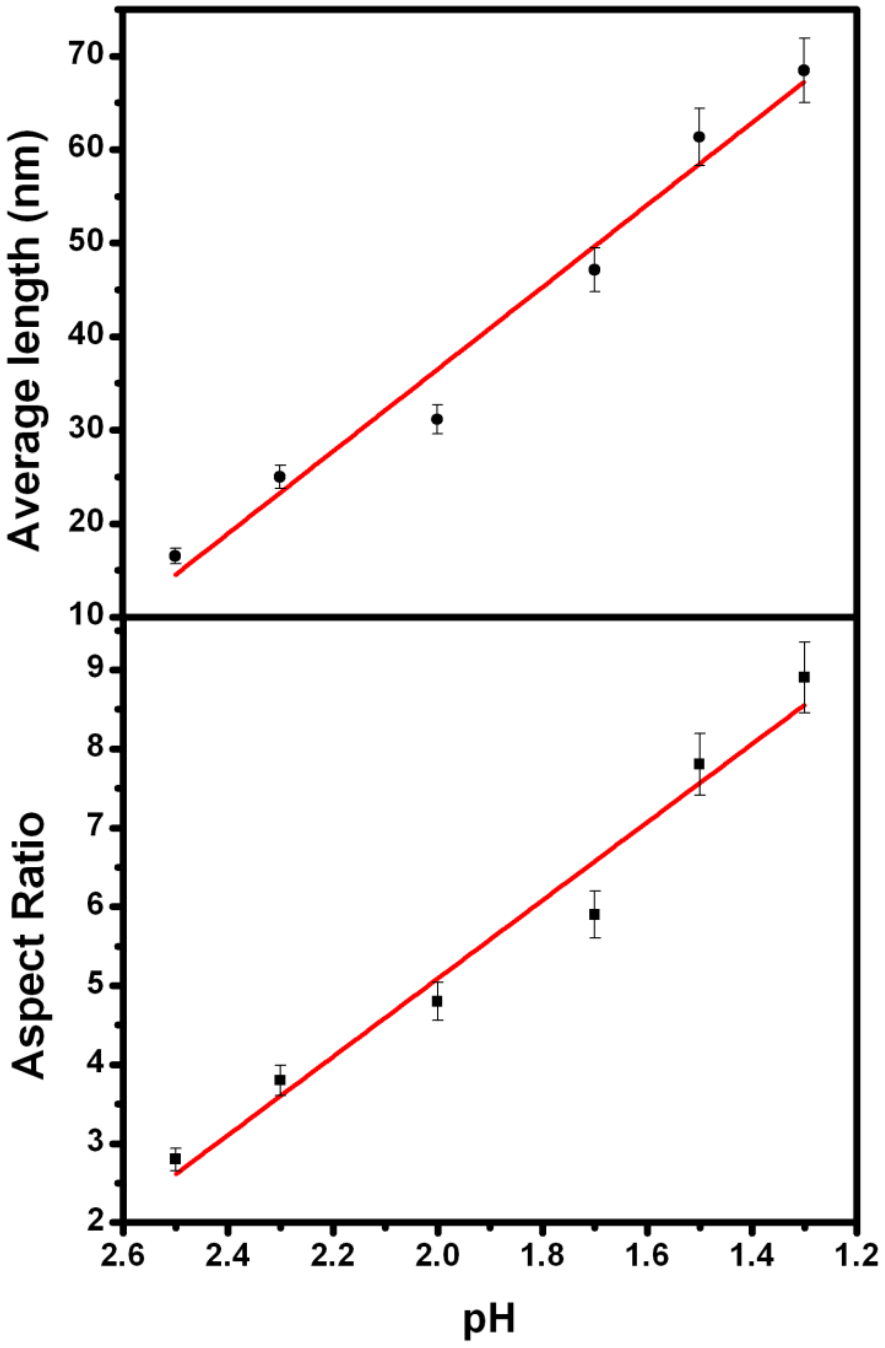

Fig. 4.6 Effect of pH of the growth solution on the average length and average aspect ratios of GNRs synthesized by seedless growth in BDAC-CTAB binary co-surfactant system.

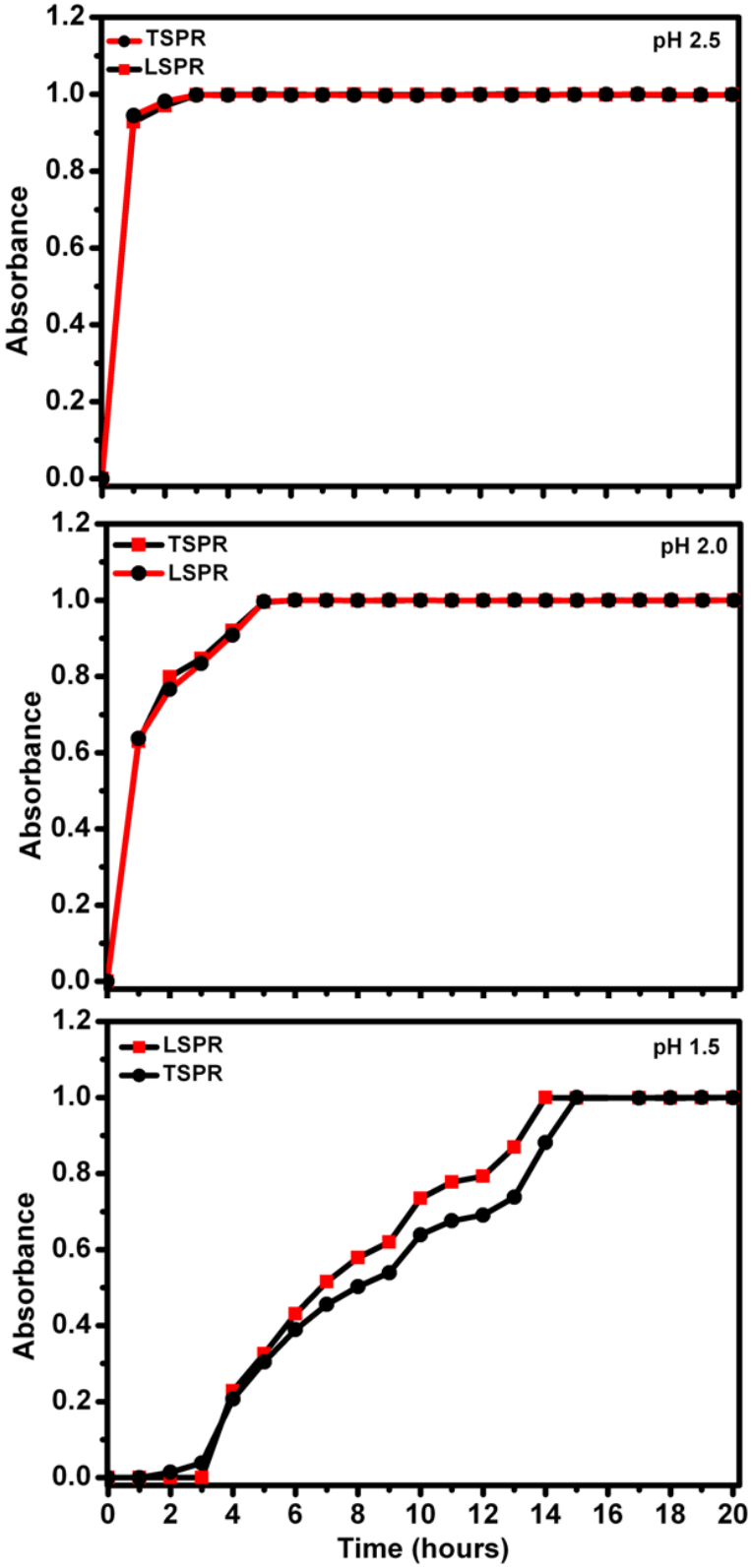

Fig. 4.7 Normalized absorbance vs time for the LSPR and TSPR bands of GNRs synthesized at pH 1.5, 2.0 and 2.5.

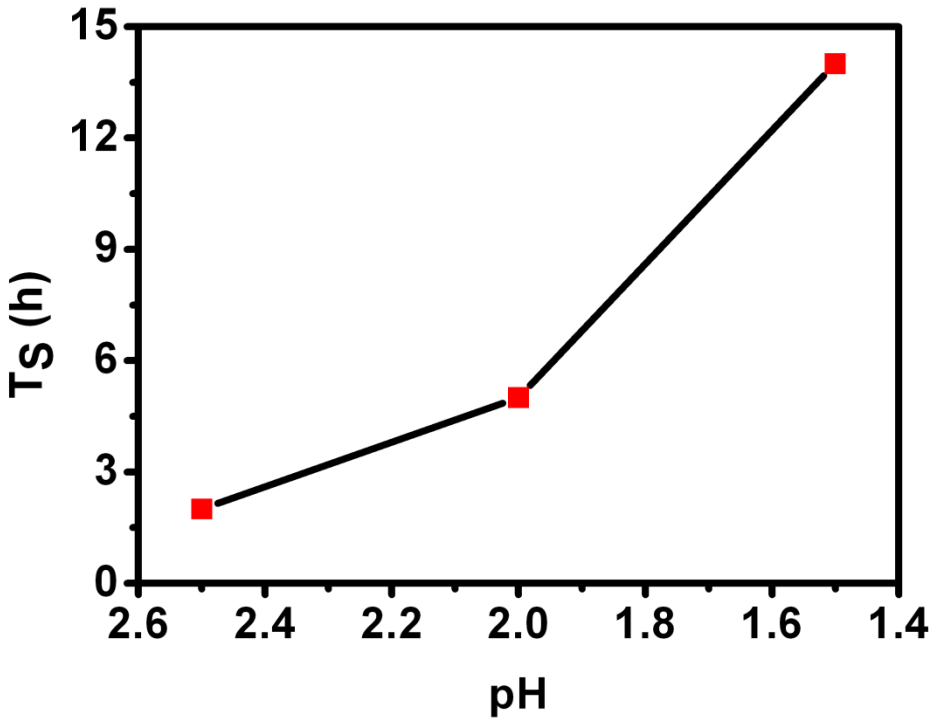

Fig. 4.8 Saturation time of growth (Ts) of GNRs as a function of pH of the growth solution.

4.2.2.1 Effect of $NaBH_4$ on pH Controlled Tunability of GNRs

To understand the influence of $NaBH_4$ on the optical and special tunability of GNRs, they are synthesized by seedless protocols as described earlier with 5, 10 and 15 µL of $NaBH_4$ (**Annexure-I** section **A6**). UV-Visible-NIR absorption spectra of GNRs prepared by pH controlled synthesis with different volume of $NaBH_4$ are shown in **Fig. 4.9**. TSPR band of GNRs is independent of pH of the growth solution and amount of the $NaBH_4$. The co-influence of pH of the growth solution and volume of reducing agent ($NaBH_4$) on the optical tunability of LSPR band of GNRs is summarized in **Table 4.2**. The LSPR band of GNRs strongly depends on the solution pH and volume of the $NaBH_4$. Irrespective of $NaBH_4$ volume the LSPR band of GNRs undergoes red shift with decrease in pH of the growth solution (**Fig. 4.10**). This red shift in the LSPR band position is more prominent with increase in the volume of $NaBH_4$. Small hump at 660 nm was observed at pH 2.5 when 5 µL $NaBH_4$ was added to the growth solution (**Fig. 4.9**). On increasing the amount of $NaBH_4$ to 10 µL, a small hump at ~ 669 nm was observed (**Fig. 4.9**). This hump converts into a well-defined LSPR band cantered at 712 nm when the volume of the $NaBH_4$ is increased to 15 µL.

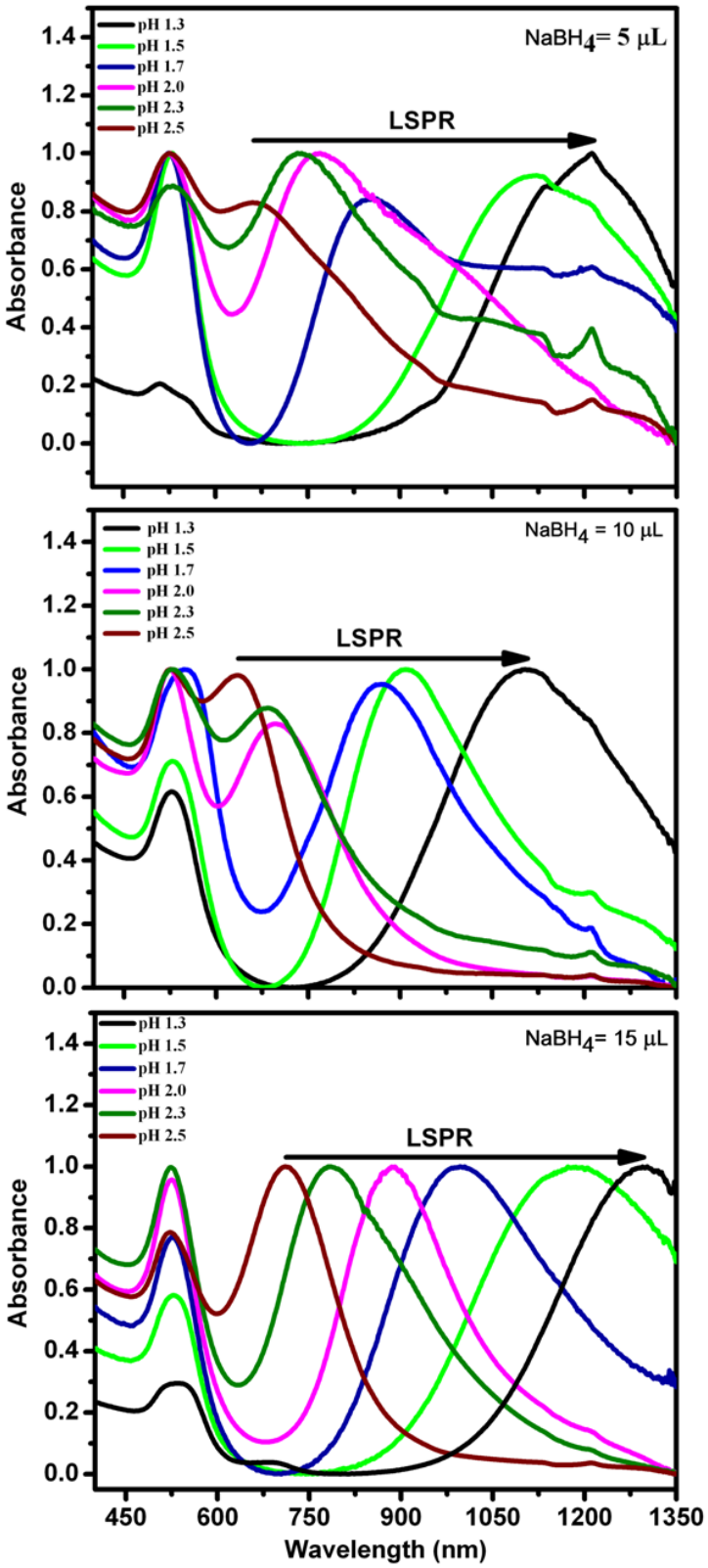

Fig. 4.9 UV-Visible-NIR absorption spectra of GNRs prepared at different pH of the growth solution with 5 µL, 10 µL and 15 µL of $NaBH_4$ in seedless synthesis.

Table 4.2 LSPR band positions of GNRs synthesized at different pH and $NaBH_4$ volumes in seedless synthesis.

$NaBH_4$ (µL) →	5	10	15
pH ↓		λ_{LSPR} (nm)	
1.3	1202	1225	1295
1.5	1117	1141	1182
1.7	855	909	992
2.0	765	869	889
2.3	669	699	787
2.5	660	634	712

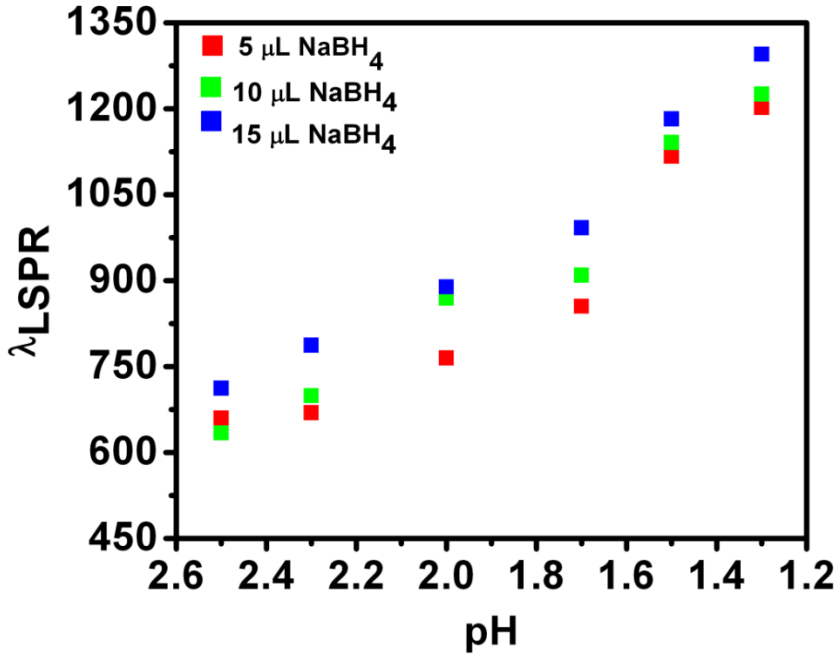

Fig 4.10 Effect of $NaBH_4$ volume on the LSPR band positions of GNRs prepared at different pH of the growth solution in the seedless synthesis.

4.2.2.2 Effect of BDAC and pH on Anisotropic Growth of GNRs

Various mechanisms for the anisotropic growth of gold nanoparticles in CTAB based seeded approach have previously been proposed by different research groups [28, 29]. They are built on three basic approaches. The first approach is silver under-potential deposition (UPD) [28]. In this mechanism, it is assumed that presence of silver ions is responsible for the anisotropic growth. In the second approach, it is proposed that silver forms a complex with Br^- ions (CTA^+-Br^--Ag^+), which is acting as face-specific capping agent, encouraging

the anisotropic growth of GNRs [29]. In the third approach, it is proposed that rod-shaped CTAB-micelles are acting as soft templates, which are directing the anisotropic growth [30].

These proposed mechanisms are in sharp contradiction with each other. There are no consensuses among researches on growth mechanism leading to anisotropic growth of GNRs. Studies suggest that different facets of the Au ions have different affinity for the surfactants [31]. CTAB forms a bilayer on the {110}/{100} facet and sets the {111} facet free for the adsorption of Au/Ag ions present in the growth solution [32]. If silver UPD mechanism is responsible for the anisotropic growth, then why GNRs does not grow to the same extent irrespective of the BDAC/CTAB and pH of the growth solution in seedless approach? CTA^+-Br^--Ag^+ complex acts as a face specific capping agents rather than silver alone in the UPD mechanism encouraging the anisotropic growth, then what could be the role of BDAC micelles in elongation of GNR? Does only CTAB micelle form a soft template or BDAC micelles also play a role in template formation and anisotropic growth of GNRs? It is yet to be established which of the three mechanisms are actually responsible for the anisotropic growth of GNRs. There is a likely possibility that all the three mechanisms coexist and are partially responsible for the growth of GNRs [31].

BDAC is known to facilitate the growth of GNRs with higher aspect ratios [13]. BDAC has smaller micelle aggregation number among surfactants with equivalent alkyl chain lengths [33]. This is because of the bulky polar head group of BDAC, which provides additional hydrophobicity and larger surface area [34-36]. Some studies suggests that BDAC induces faster growth along the length of the GNRs, if it binds preferentially to the ends due to its weaker binding caused by the substitution of a phenyl group instead of methyl group or due to the presence of chloride ions in place of bromide ions as in CTAB [33]. Bakshi et al. observed that the micellar structure of BDAC and CTAB co-surfactants is significantly different from that of CTAB alone [37]. The size of the mixed micelles is much smaller due to the non-polarity introduced in the stern layer by the benzyl ring. They are compact, more hydrophobic and have a greater aggregation number due to the charge neutralization in the stern layer when surfactants of same or different head groups are mixed [37]. After surface passivation due to adsorption of binary surfactants; the probability of ad-atom addition on GNRs surface is quite low [33].

If we recall the anisotropic growth of GNRs in CTAB solution, the contribution of smaller micelles in enhancing the aspect ratio of the GNRs can be interpreted. Anisotropic growth begins only after the isotropic seed exhibits facets large enough to accommodate adsorption of CTAB micelles (~ 6 nm in diameter) [32]. Therefore, it is likely that in the BDAC and CTAB co-surfactant system, the anisotropic growth starts at the very beginning when the size of the seed is smaller than the miceller size of CTAB (6 nm). Mixed micelles adsorb on the transverse {100} and {110} crystalline facets of the seeds thus restricting the growth of the GNRs along these facets. Longitudinal growth is promoted along the {111} crystalline facet. Therefore, increase in the aspect ratio of GNRs in BDAC-CTAB co-surfactant system can be attributed to the better confinement on transverse growth from an earlier stage. The cartoon representation of growth mechanism for the formation of GNRs using BDAC and CTAB is shown in **Fig. 4.11**.

Use of BDAC in the growth solution is also accompanied by decrease in the pH of the growth solution. The role of pH in nanorods elongation is still not well understood. It is known that reaction proceeds slowly if the reaction pH is low [19]. Hence, lowering the pH, the growth rate of GNRs can be reduced, which favours the anisotropic growth [8, 19]. In addition, reducing ability of ascorbic acid depends strongly on the pH of the solution [19]. The reducing ability of ascorbic acid decreases dramatically under strong acidic conditions (pH < 2.5).

Anisotropic growth of GNRs in seedless approach is controlled by two competitive processes; i.e. the seed formation and their growth into anisotropic nanorods. An experiment identical to that explained previously for the seedless synthesis was performed to elucidate the role of pH in nanorods' growth.15 μL $NaBH_4$ was added to each growth solution maintained at pH 2.5, 2.0 and 1.5. These pH values were chosen for the better comparison at higher, intermediate and lower pH conditions. UV-Visible-NIR spectra of the growth solutions were recorded every 2 min after the addition of $NaBH_4$ till the appearance of the second peak (**Fig. 4.12**). Number and rate at which seeds formed was monitored as a function of pH of the growth solution and $NaBH_4$ volume. A significant difference is observed in the UV-visible spectra of seeds grown at pH 2.5, 2.0 and 1.5 with $NaBH_4$ constant at 15 μL. At any given time the absorbance of the seeds is highest for pH 2.5 and is lowest for pH 1.5

indicating that with decrease in the pH the number of seeds formed in the solution also decreases.

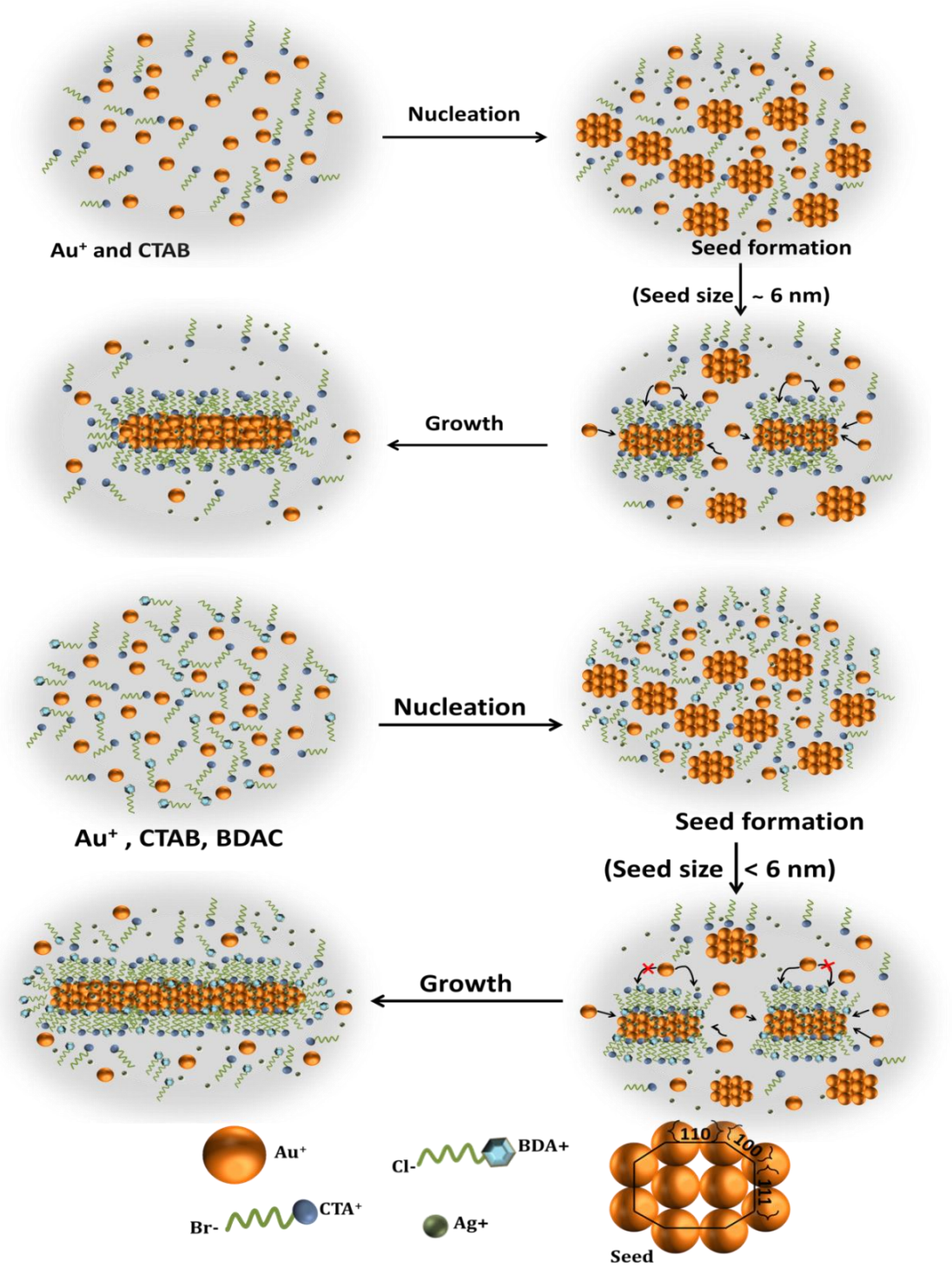

Fig. 4.11 Cartoon representation of growth mechanism of GNR's in BDAC-CTAB binary co-surfactant system.

Not only the number of seeds formed at a time in the solution depends on the pH but also the rate at which these seeds form also depends on it. The growth rate is highest when pH is 2.5 and it decreases with decrease in the pH (**Fig. 4.12 (d)**). The measurement was terminated the moment the LSPR peak corresponding to anisotropic growth appears. The anisotropic growth begins within 35 mins when pH is 2.5, while it is delayed to 88 mins when the pH is 1.5 indicating the delayed onset of growth stage.

The growth rate of GNRs was also monitored in identical experiments in which absorbance of both LSPR and TSPR bands were measured as a function of time. The growth rate of GNRs was slow at pH 1.5 as compared to what it was at pH 2.5 (**Fig. 4.7**). The difference in the growth rate under different pH conditions can also be judged from the changes in the solution color. It took 20 h to transform from colorless to light pink and then to dark red when pH was low (1.5), which immediately turned dark red when pH was high (2.5). The growth rate of GNRs decreases with decrease in pH of the growth solution. At low pH Au(I) was slowly reduced to Au(0), which also helps in selective adsorption of Au atoms to the specific crystal facets of the rod, through the soft template created by BDAC and CTAB micelles. The saturation growth time (T_s) which is the time taken for the GNRs' growth to saturate also increases with decrease in pH (**Fig. 4.8**) also indicating that the growth becomes sluggish with decrease in the pH of the growth solution. To have a relative comparison of the GNRs yield, the absorbance of LSPR band was measured as a function of pH after 20 h (**Fig. 4.13**). At higher pH the absorbance is highest i.e. yield is maximum and at lower pH the absorbance is minimum and hence the GNRs yield too is minimum. Thus lower pH of the growth solution favours the crystallization of GNRs with higher aspect ratio as it reduces the density of seeds formed, the rate at which seeding took place and the rate at which they grow into anisotropic nanorods. Hence, at lower pH few seeds grow into large aspect ratio GNRs while at higher pH, larger number of seeds converts themselves into smaller aspect ratio GNRs.

To further probe the role of $NaBH_4$ in the nucleation and growth of GNRs, identical experiments were performed as explained earlier but this time at constant pH (2.5) of the growth solution and with $NaBH_4$ volume varying from 5 µL to 15 µL. UV-Visible spectra (**Fig. 4.12(e-g)**) was recorded as a function of time to see the influence of $NaBH_4$ volume on the seeding and growth of GNRs. Both the density and rate of seed formation is higher for 15 µL of $NaBH_4$ while it decrease significantly when $NaBH_4$ volume was lowered to 5 µL (**Fig. 4.12(h)**).

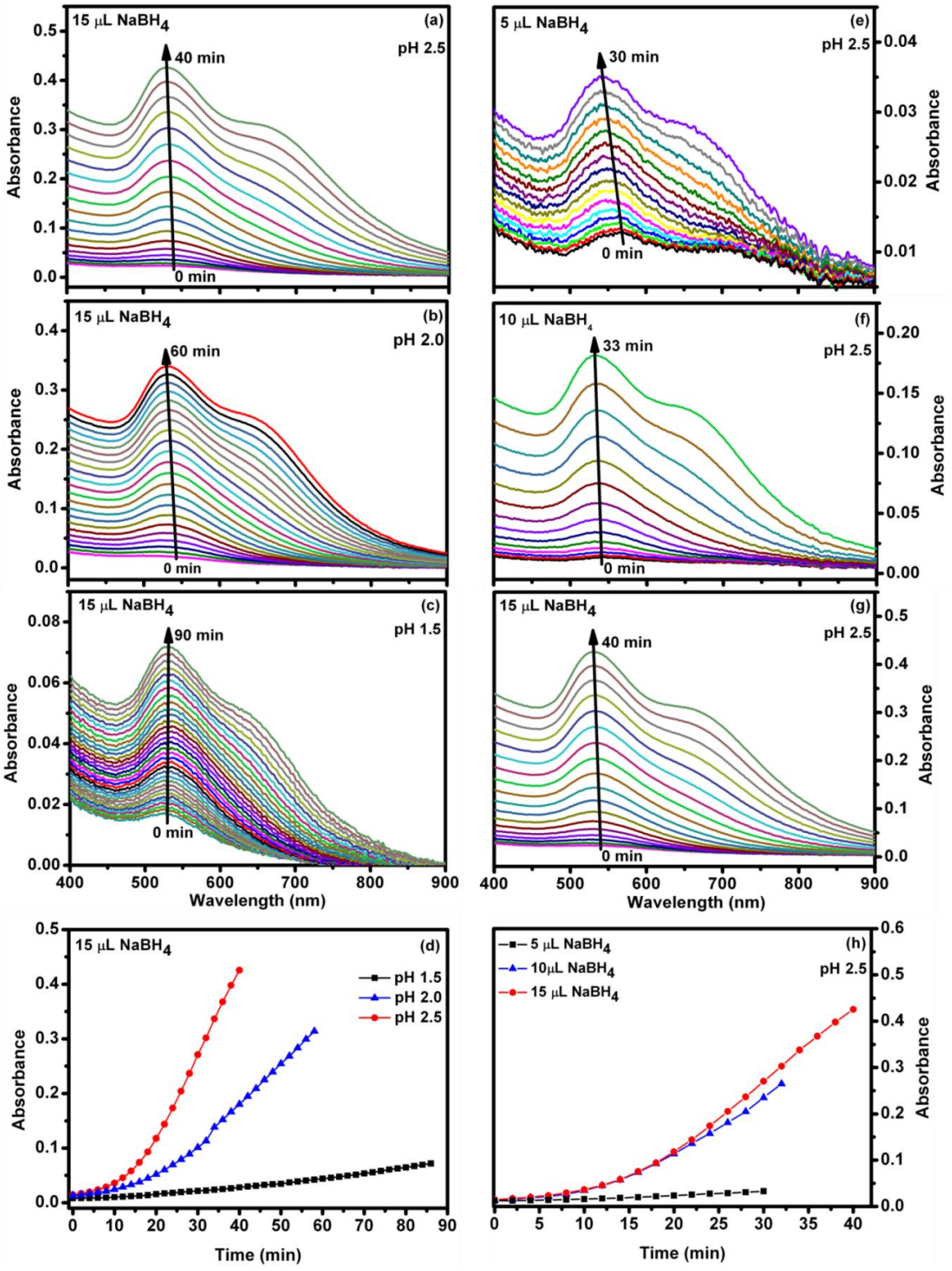

Fig. 4.12 (a, b, c) UV-Visible-NIR spectra of gold seeds as a function of time for pH 1.5, 2.0 and 2.5 at constant $NaBH_4$ concentration of 15 µL; (d) Absorbance vs time plot of gold seeds for pH 1.5, 2.0 and 2.5 at constant $NaBH_4$ volume of 15 µL; (e, f, g) UV-Visible-NIR spectra of gold seeds as a function of time for 5, 10 and 15 µL $NaBH_4$ at constant pH 2.5; (h) Absorbance vs time plot of gold seeds for 5, 10 and 15 µL $NaBH_4$ at constant pH 2.5.

When these seeds were allowed to grow till saturation; their yield increases with the volume of $NaBH_4$ (**Fig. 4.13 (b)**). Hence, it is expected that GNRs grown with higher volume of $NaBH_4$ should have smaller aspect ratio as compared to those GNRs which are prepared with lower $NaBH_4$. Instead what is observed is the precisely opposite of this. The aspect ratio of GNRs increases with increase in $NaBH_4$ volume in the growth solution. On addition of $NaBH_4$, Au(III) gets reduced to Au(I), which is further reduced to the Au(0) during GNR growth by seeds [31, 34]. When 5 µL of $NaBH_4$ is used, it was not sufficient enough to reduce entire Au(III) to Au(0) during the growth stage and hence, GNRs growth remained deficient, which results into fewer GNRs having small aspect ratios. With higher $NaBH_4$ volume; the reduction of Au(I) to Au(0) proceeds without any interruption and thus the number of Au ions in the growth solution available per nanorod increases, which eventually increases the aspect ratio of GNRs.

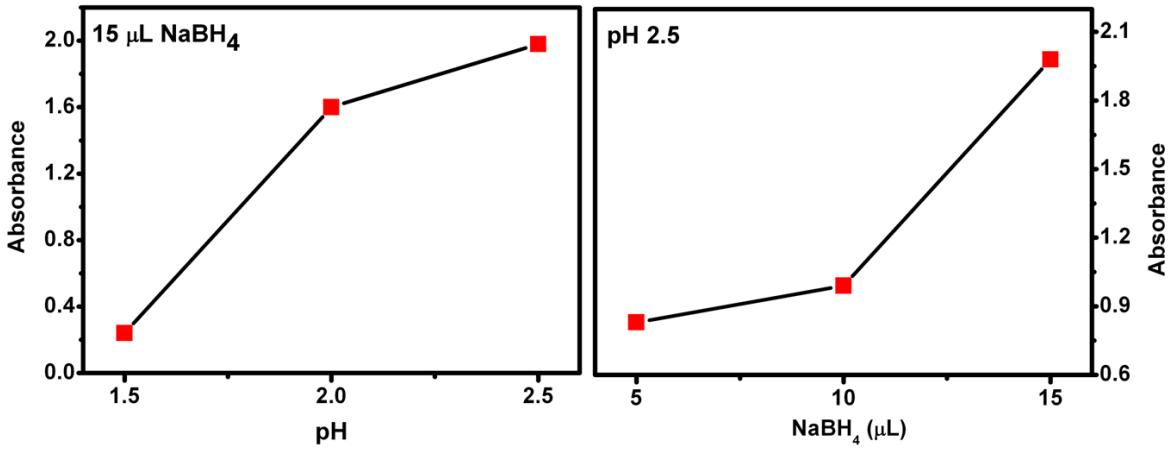

Fig. 4.13 Absorbance of LSPR band after saturation of GNRs growth as a function of pH at constant volume of $NaBH_4$ and volume of $NaBH_4$ at constant pH 2.5.

4.3 TUNABILITY OF GNPs

4.3.1 Seed-Mediated Tunability of GNPs Synthesized By Pluronic F-127

To synthesize GNPs with tuneable SPR band in the NIR region by seed-mediated method, synthesis protocols identical to those followed for GNRs was followed. Detailed protocol followed for the synthesis of GNRs is described in **Annexure-I** at section **A7**.

UV-Visible-NIR absorption spectra of gold nanoparticles synthesized by seed-mediated synthesis using pluronic F-127 single-surfactant system are shown in **Fig 4.14**. Two plasmon

bands are observed after every successive addition of growth solution in the UV-Visible-NIR spectra. These plasmon bands correspond to the in-plane and out-of-plane resonances of GNPs. On successive addition of secondary growth solution; in-plane plasmon bands red shift with little increase in absorbance of both the plasmon bands are observed (**Fig. 4.14**). No red shift was observed after three successive additions of secondary growth solution. Formation of GNPs starts within a minute of the addition of gold seeds into the growth solution. This is evidenced from the two plasmon bands in the Vis-NIR spectrum immediately formed (reading 0) (**Fig. 4.14**). The plasmon band at 526 nm corresponds to the out-of-plane vibrations while the second band at 900 nm corresponds to in-plane quadruple oscillations of the electrons. With each successive addition, intensity of both the plasmon bands increases along with the red shift in the band position corresponding to in-plane quadruple oscillations indicating the growth of nanostructures. In-plane SPR stabilizes at 960 nm after three successive additions of secondary growth solution. No further shift in the SPR band is observed indicating the saturation of the growth.

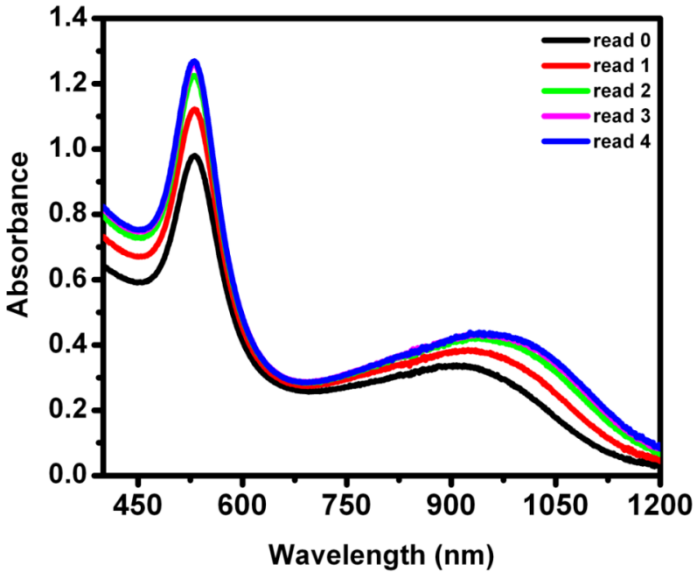

Fig. 4.14 UV-Vis-NIR spectra of GNPs prepared by successive addition of secondary growth solution.

This study indicates that successive additions of growth solution leading to limited tunability of plasmonic bands of GNRs. An attempt was also made to explore the effect of pH on the tunability of GNRs when synthesized through seedless approach. However, no systematic variations in the plasmon bands were observed. Hence tunability of plasmonic properties of GNPs is not explored further.

References:

1. X. Huang, S. Neretina, M.A. El-Sayed, *Adv. Mater*, **2009**, 21, 1–31.
2. P. Zhao, D. Astruc, N. Li, *Chem. Int. Ed*., **2014**, 53, 1756 – 1789.
3. J. Gao, C.M. Bender, C.J. Murphy, *Langmuir*, **2003**, 19, 9065-9070.
4. R. Kaur, S.K. Mehta, *Coord Chem Rev*., **2014**, 262, 37-54.
5. L. Zhang, K. Xia, Z. Lu, G. Li, J. Chen , Y. Deng, S.L.F. Zhou, N. He, *Chem. Mater*., **2014**, 26, 1794−1798.
6. N.R. Jana, L. Gearheart, C.J. Murphy, *Chem. Mater*., **2001**, 13, 2313-2311.
7. B. Nikoobakht, M.A. El-Sayed, *Chem. Mater*, **2003**, 15, 1957-1962.
8. C. Wang, T. Wang, Z. Ma, Z. Su, *Nanotechnology*, **2005**, 16, 2555–2560.
9. A.R. Tao, S. Habas, P. Yang, *Small*, **2008**, 4, 310-325.
10. J.P. Justea, I.P. Santosa, L.M.L Marzána, P. Mulvaney, *Coord. Chem. Rev*., **2005**, 249, 1870–1901.
11. S. Koeppl, C. Solenthaler, W. Caseri, R. Spolenak, *J. Nanomater*., **2011**, 2011, 515049, 1-13.
12. N.R. Jana, L.A. Gearheart, C.J. Murphy, *Adv. Mater*., **2001**, 13, 1389-1393.
13. K.A. Kozek, K.M. Kozek, W.-C.Wu, S.R. Mishra, J.B. Tracy, *Chem. Mater*., **2013**, 25, 4537–4544.
14. D.A. Zweifel, A. Wei, *Chem. Mater*., **2005**, 17, 4256−4261.
15. H. Tyagi, A. Kushwaha, A. Kumar, M. Aslam, *Int. J. Nanosci*., **2011**, 10, 857-860.
16. D.K. Smith, N.R. Miller, B.A. Korgel, *Langmuir*, **2009**, 25, 9518−9524.
17. T. Wen, Z. Hu, W. Liu, H. Zhang, S. Hou, X. Hu, X. Wu, *Langmuir*, **2012**, 28, 17517-23.
18. T.K. Sau, C.J. Murphy, *Philos. Mag*., **2007**, 87, 2143−2158.
19. L. Vigderman, E.R. Zubarev, *Chem. Mater*., **2013**, 25, 1450–1457.
20. X. Ye, L. Jin, H. Caglayan, J. Chen, G. Xing, C. Zheng, V.D. Nguyen, Y. Kang, N. Engheta, C.R. Kagan, C.B. Murray, *ACS Nano*, **2012**, 6, 2804–2817.
21. J.P. Juste, L.M. Liz-Marzan, S. Carnie, D.Y.C. Chan, P. Mulvaney, *Adv.Func.Maters.*, **2004**, 14, 571-579.
22. P. Zijlstra, C. Bullen, J.W.M. Chon, M. Gu, *J. Phys. Chem. B*, **2006**, 110, 19315–19318.
23. M.R.K. Ali, B. Snyder, M.A. El-Sayed, *Langmuir*, **2012**, 28, 9807–9815.
24. J. Zhu, K.T. Yong, I. Roy, R. Hu, H. Ding, L. Zhao, M.T. Swihart, G.S. He, Y. Cui, P.N. Prasad, *Nanotechnology*, **2010**, 21, 285106.
25. A. Brioude, X.C. Jiang, M.P. Pileni, *J. Phys. Chem. B*, **2005**, 109, 13138-13142.
26. C.L. John, S.L. Strating, K.A. Shephard, J.X. Zhao, *RSC Adv*., **2013**, 3, 10909-10918.
27. C.J. Orendorff, P.L. Hankins, C.J. Murphy, *Langmuir*, **2005**, 21, 2022-2026.
28. M.L. Personick, M.R. Langille, J. Zhang, C.A. Mirkin, *Nano Lett*., **2011**, 11, 3394–3398.
29. C.J. Murphy, L.B. Thompson, A.M. Alkilany, P.N. Sisco, S.N. Boulos, S. Sivapalan, J.A. Yang, D.J. Chernak, J. Huang, *J. Phys. Chem. Lett*., **2010**, 1, 2867-2875.
30. N.R. Jana, *Small*, **2005**, 1, 875-882.
31. S.E. Lohse, C.J. Murphy, *Chem Mater*., **2013**, 25, 1250−1261.

32. K. Park, L.F. Drummy, R.C. Wadams, H. Koerner, D. Nepal, L. Fabris, R.A.Vaia, *Chem. Mater*., **2013**, 25, 555–563.
33. M.S. Bakshi, *Cryst. Growth Des*., **2016**, 16, 1104-1133.
34. K. Park K, H. Koerner , R.A. Vaia, *Nano Lett*., **2010**, 10,1433−1439.
35. R.G. Alargova, I.I. Kochijashky, M.L. Sierra, R. Zana, *Langmuir*, **1998**, 14, 5412−5418.
36. V.K. Aswal, P.S. Goyal, *Chem. Phys. Lett*., **2003**, 368, 59−65.
37. M.S. Bakshi, K. Singh, *J. Colloid Interface Sci*., **2005**, 287, 288-297.

CHAPTER 5

STABILITY AND BIOCOMPATIBILITY OF GOLD NANOSTRUCTURES

5.1 INTRODUCTION

Wet chemical synthesis is being widely used for the preparation of GNRs and GNPs because of the ease and flexibility which this technique offers viz-a-viz tuning of plasmonic properties of these anisotropic nanostructures [1-4]. GNRs and GNPs due to their tuneable surface plasmon resonance deep into the NIR region are now been widely exploited for *in-vivo* hyperthermia treatment of cancer. Major short coming of wet chemical synthesis is the poor colloidal stability of synthesized nanoparticles [5, 6]. Colloidal stability of nanoparticles can be improved by various means for example, increasing electrolyte concentration, adjusting the solution pH, adding different inorganic salts, changing capping agents or changing dispersion medium [7-10]. Despite of the range of parameters available to improve stability of nanoparticles, poor stability and limited shelf life always remained a challenge and limits the applications of gold nanostructures in cancer hyperthermia. Cytotoxicity of GNRs and GNPs are not well documented. Biocompatibility of gold nanoparticles has previously been investigated as a function of concentration [11], size [12] and shape [13], stabilizing and capping agents [14, 15]. There are conflicting reports on the biocompatibility of these gold nanostructures.

To explore feasibility to be useable as an *in-vivo* agent in cancer hyperthermia, stability and biocompatibility of nanostructures are important issues and needs to be investigated [16-18]. In this chapter spectral and dimensional stability of GNRs and GNPs are investigated. Method of synthesis and medium of dispersion are the variables of the study in estimating the stability of GNRs against aging. Biocompatibility of GNRs and GNPs, prepared by seed-mediated and seedless synthesis approaches were also investigated in this chapter. Cell viability tests are conducted on the RAW 264.7 macrophage cell lines. Cytotoxicity of GNRs and GNPs was determined by MTT assays.

5.2 COLLOIDAL STABILITY OF GNRs

5.2.1 Effect of Colloidal Medium

GNRs were synthesized by seed-mediated method as described in chapter 3. Four samples of GNRs were prepared simultaneously under identical conditions. After centrifugation each sample was preserved under ambient conditions either in DI water, or in pluronic F-127, or in CTAB or in growth solution (GS). These colloidal suspensions were examined by UV-Visible spectroscopy for 30 days. Effect of colloidal medium on the stability of GNRs was evaluated on the basis of variation in their SPR bands. Samples were neither diluted nor sonicated prior to measurements.

UV-visible spectra of GNRs preserved in different mediums recorded over 30 days are shown in **Fig. 5.1**. Maximum blue shift (803 to 570 nm) was observed in the LSPR band of GNRs preserved in the growth solution, followed by CTAB (781 to 681 nm). Good stability of GNRs was observed in pluronic F-127 and in DI water. LSPR band shifted from 790 to 764 nm when preserved in pluronic F-127 and 793 to 741 nm when preserved in DI water. Effect of colloidal medium on the dimensions of GNRs was also investigated by photon correlation spectroscopy (**Fig. 5.2**). Two distinct size distributions were observed for each GNR suspension. The mean hydrodynamic size (length & diameter) of GNRs obtained from PCS on day-1 and day-30 are shown in **Table 5.1**. Here $D_{H_{S1}}$ and D_{HL_1} are the hydrodynamic dimensions of GNRs corresponding to short and long axis, respectively which are measured on day-1. $D_{H_{S30}}$and $D_{HL_{30}}$ are the hydrodynamic dimensions of GNRs corresponding to short and long axis, respectively which are measured on the day-30. A monomodal size distribution is obtained in PCS measurements on the 30th day for GNRs preserved in GS. Transformation of bimodal size distribution to monomodal size distribution of GNRs preserved in GS indicates that when GNRs are preserved in GS, their anisotropic shape deforms and gets converted into symmetric spherical morphology.

The variations in LSPR and TSPR band positions of GNRs preserved in different media as function of time is shown in **Fig. 5.3**. Corresponding variation in the absorbance maximum of LSPR and TSPR bands of GNRs are also shown in **Fig. 5.4**. GNR preserved in GS undergoes maximum blue shift in their LSPR band with the color of the colloid changes

from light pink to dark purple. This blue shift of LSPR band and change in the color of the colloid is because of the decrease in the aspect ratio of GNRs.

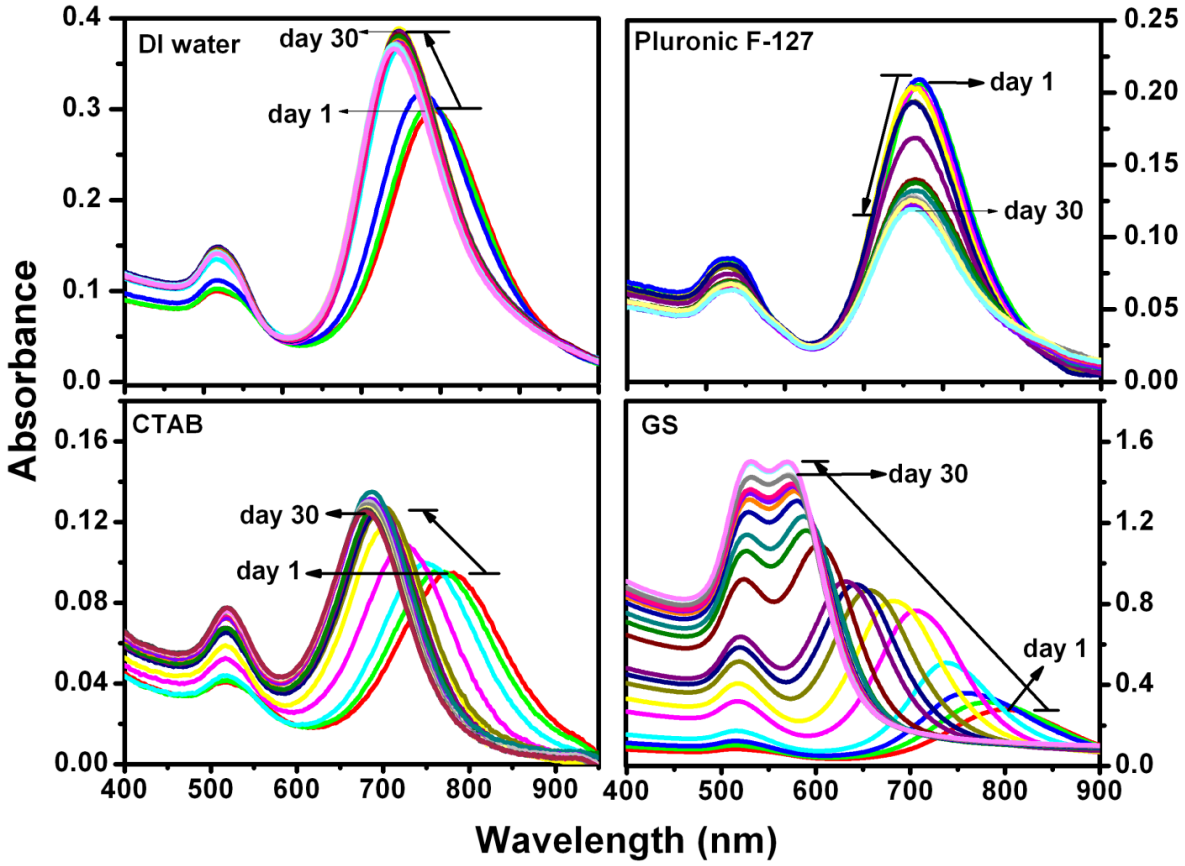

Fig. 5.1 UV-Visible absorption spectra of GNRs preserved DI water, pluronic F-127, CTAB and growth solution.

The spectral drift in absorbance maximum and band position of GNRs recorded for 30 days is shown in **Fig. 5.5**. Large shift in the LSPR band position from 803 nm (on day 1) to 570 nm (on day 30) has been observed in case of GNRs preserved in GS. Spectral Shift is quite prominent during first 20 days. LSPR band blue shifts from 803 nm to 580 nm within 20 days. After this, gradual drift upto 570 nm is observed in next 10 days.

The percentage change in the LSPR band position of GNRs when preserved in GS is 29%. A continuous red shift from 513 nm to 531 nm is observed in the TSPR band of GNRs preserved in GS. As can be seen in **Fig. 5.4**, there is constant increase in the TSPR (0.08 to 1.53) and LSPR (0.28 to 1.16) band intensities of GNRs preserved in GS. Upon aging well distinguishable TSPR and LSPR bands of GNRs preserved in GS starts over lapping and

eventually merge into single band (**Fig. 5.4**). This is because of the deformation of anisotropic rods into isotropic spheres.

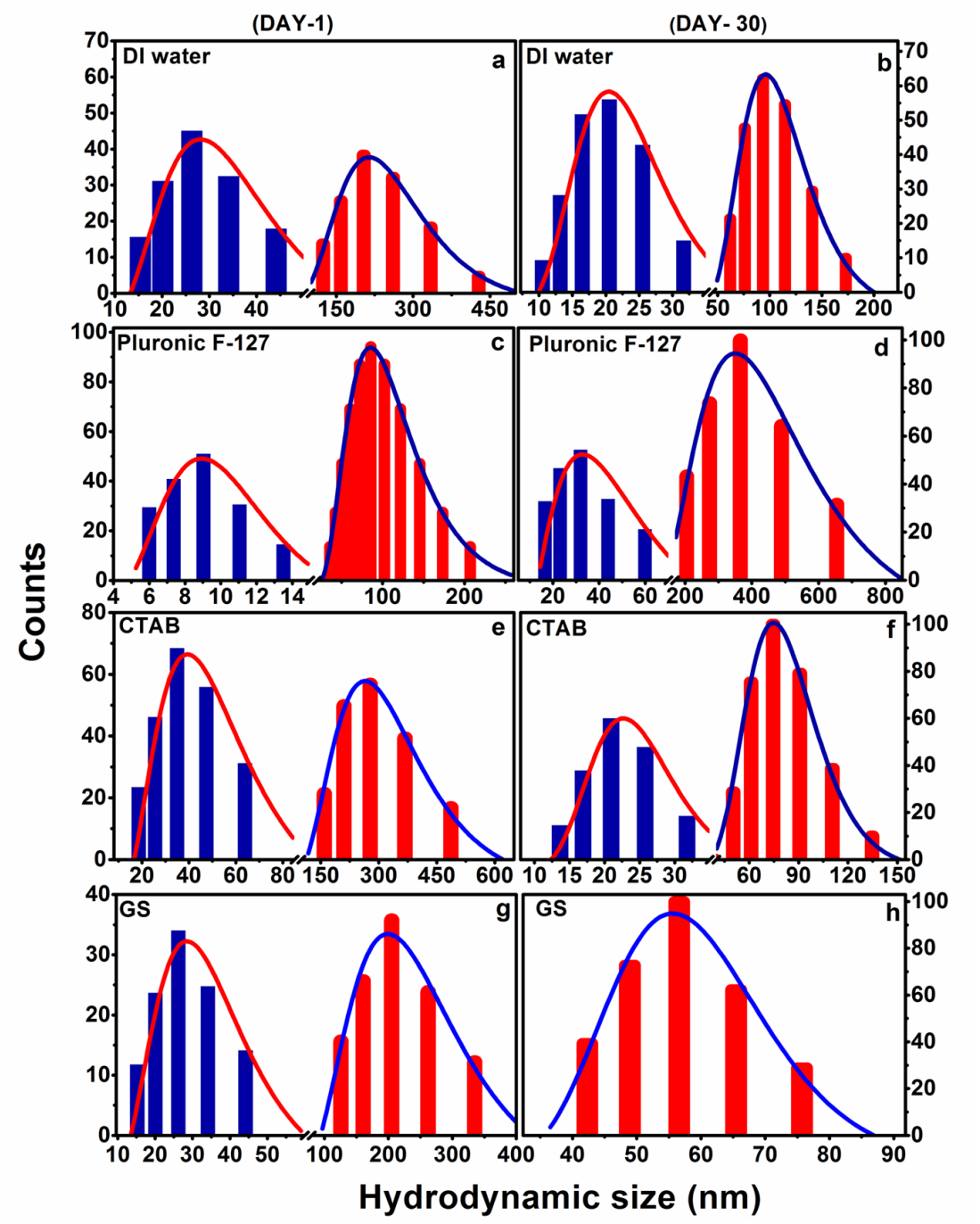

Fig. 5.2 Hydrodynamic size distribution of GNRs recorded on day-1 and day-30. GNRs are preserved in: DI water, pluronic F-127, CTAB solution and growth solution. Each histogram is fitted with lognormal particle size distribution function. Each histogram represents a bimodal size distribution corresponding to the long and short axis of GNRs (except h, where only single size distribution is observed).

Table 5.1 Hydrodynamic size distribution of GNRs preserved in DI water, pluronic F-127, CTAB and GS.

Medium	$D_{H_{S1}}$ (short axis) (nm)	$D_{H_{L1}}$ (long axis) (nm)	$D_{H_{S30}}$ (short axis) (nm)	$D_{H_{L30}}$ (long axis) (nm)
DI water	33.3	248.6	22.6	107.1
Pluronic F-127	09.9	106.1	47.9	438.7
CTAB	50.1	316.2	24.7	081.0
GS	34.0	239.0	58.2	058.2

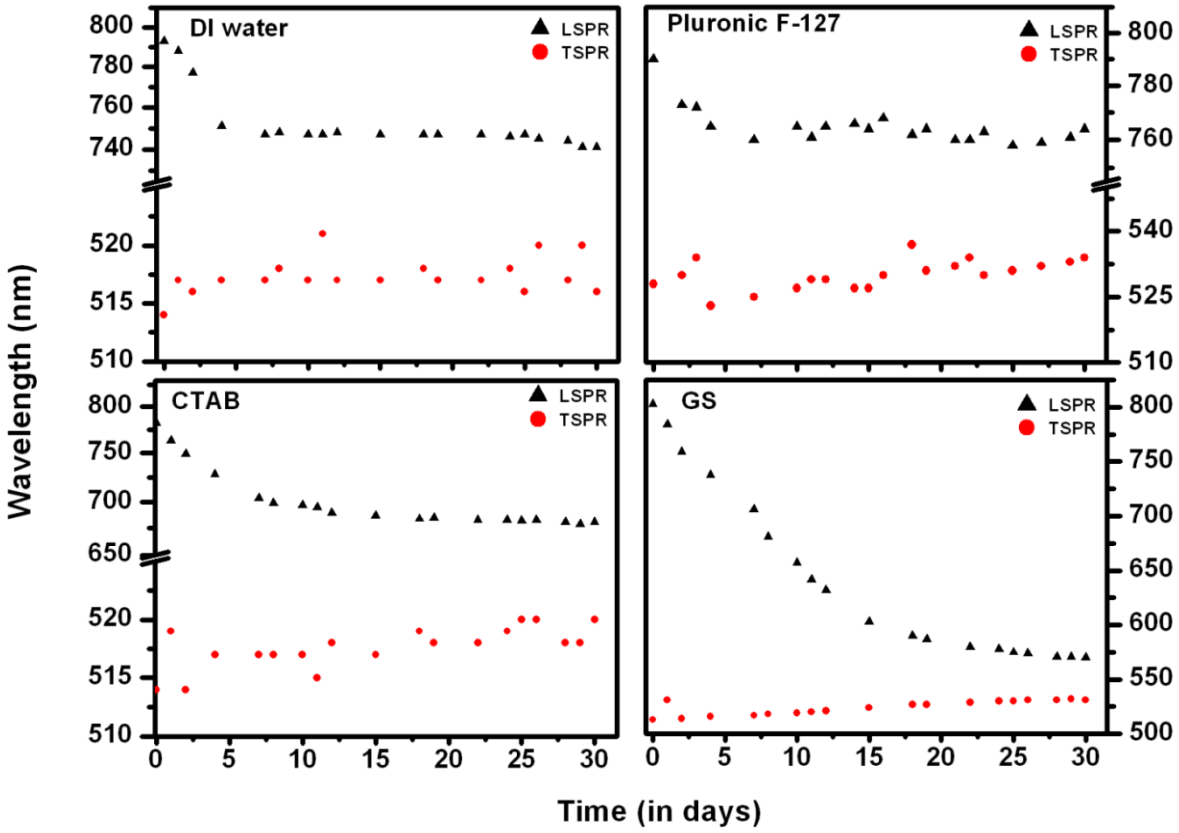

Fig. 5.3 Effect of aging on the LSPR and TSPR band positions of GNRs preserved in DI water, pluronic F-127, CTAB and GS.

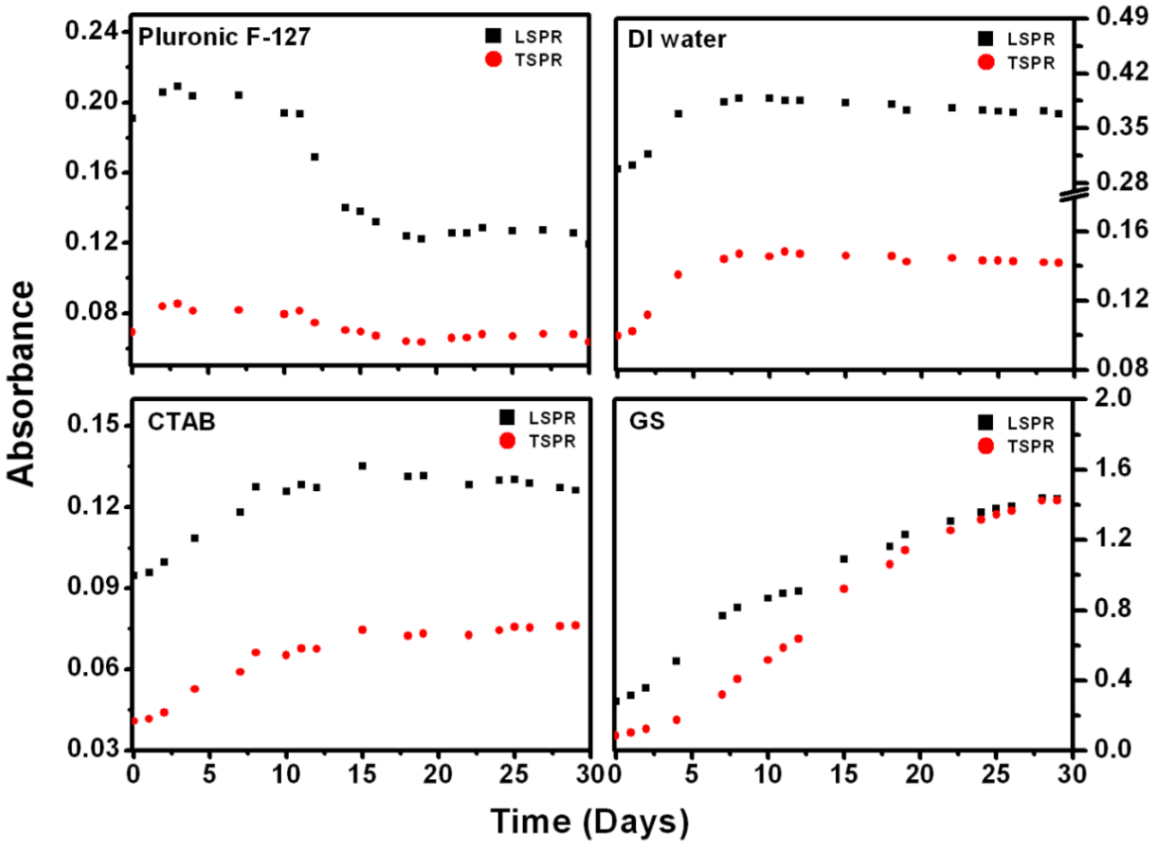

Fig. 5.4 Effect of aging on the absorption maximum of LSPR and TSPR bands of GNRs preserved in DI water, pluronic F-127, CTAB and GS.

GNRs preserved in CTAB shows a sharp blue shift (781 to 695 nm) of 85 nm in the LSPR band in the initial 10 days **(Fig. 5.3)**. After this the LSPR band stabilized at 681 nm. This shift might be because of the decrease in the aspect ratio of GNRs. In this case, LSPR band blue shifts by 12.80%. This shift is significantly lower than that observed for GNRs preserved in GS. A red shift of 6 nm (514 nm to 520 nm) in the TSPR band of GNRs is also observed. These changes are similar to those observed for GNRs preserved in GS. The only difference is in the magnitudes of the shift, which might be because of the difference in the change in the aspect ratio of GNRs preserved in GS and CTAB. A continuous rise in the absorbance of LSPR and TSPR bands are observed in the first 15 days after which they too saturate (**Fig. 5.4**). The percentage change in absorbance is 31.4 % for LSPR and 48.1% for TSPR. This large change both in the spectral shift and absorbance indicates that the GNRs have low stability in CTAB. This could be associated with the detachment of CTAB moieties from the surface of GNRs.

GNRs when preserved in pluronic F-127 show better stability as compared to those preserved in GS and CTAB. A blue shift of 26 nm (790 nm to 764 nm) is observed in the LSPR band of GNRs during first 3 days (**Fig. 5.3**). After that the LSPR band is stable at 764 ± 3 nm. Percentage change in LSPR band position is only 3.29%. TSPR band also red shifts by 18 nm. Similar behaviour is also observed for GNRs preserved in DI water. LSPR band blue shift by 46 nm (793 to 747 nm) during the initial 7 days and then it is stable at 741 ± 2 nm (**Fig. 5.3**). Percentage change in LSPR and TSPR band positions of GNRs preserved in DI water are 6.55% and 0.38%, respectively. Spectral stability and thus the structural stability of GNRs are highest in DI water.

In term of spectral intensities of LSPR and TSPR bands, the percentage change is 37.6% and 8.1%, respectively for GNRs preserved in pluronic F-127. Amongst GNRs preserved in different media, the percentage change in absorbance of TSPR band is minimum for pluronic F-127 (**Fig. 5.4**). Band intensity changes from 0.19 to 0.12 for LSPR and 0.07 to 0.06 for TSPR. This shifting is similar to that observed for GNRs preserved in CTAB. Effect of aging on the GNRs preserved in DI water, pluronic F-127, CTAB and GS on their plasmonic positions and their intensities are summarized in **Table 5.2 and Table 5.3**.

Fig. 5.6 shows the TEM micrographs of GNRs preserved in GS after 30 days. In the TEM micrograph spherical nanoparticles with few short aspect ratio nanorods are visible. A similar shape distortion is also observed in PCS measurement **(Fig. 5.2)**. TEM micrographs of GNRs preserved in DI water, pluronic F-127 and CTAB solution are also shown in **Fig. 5.6**. Size distribution histograms corresponding to long and short axis of GNRs obtained from TEM micrographs are also shown in **Fig. 5.6**. It can be seen from the micrographs and size distribution histograms that GNRs least deform in DI water. Deformation is highest in GS. Thus, GNRs preserved in DI water have higher stability as compared to those in GS. Aspect ratio of GNRs preserved in DI water, pluronic F-127 and CTAB solution remained between 3.1-3.5, while in GS, it drops to 1.0 **(Table 5.4)**. TEM images of GNRs at the beginning of aging cycle (I^{st} day) could not be recorded due to the non-availability of this facility on campus. UV-Visible spectroscopy, PCS and TEM microscopy reveals that the GNRs are structurally more stable when stored in DI water and least when kept in GS.

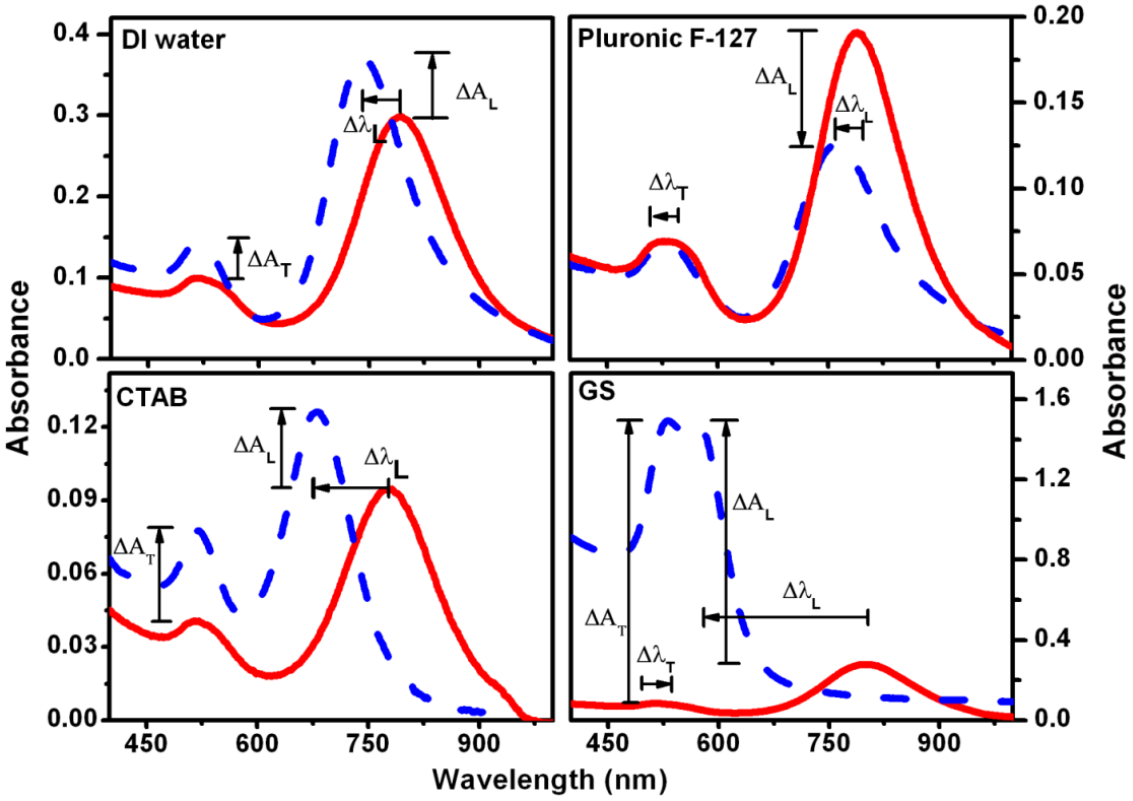

Fig. 5.5 UV-visible spectra of GNRs preserved in DI water, pluronic F-127, CTAB and GS. (——) represents the Ist day spectra and (——) represents to 30th day spectra. Spectral shift within both the LSPR and TSPR bands and their absorbance have been observed with aging.

Table 5.2 Effect of aging on the LSPR and TSPR band positions of GNRs preserved in DI water, pluronic F-127, CTAB and GS.

Medium	λ_{LSPR} (day 0) (nm)	λ_{LSPR} (day 30) (nm)	% change in λ_{LSPR}	λ_{TSPR} (day 0) (nm)	λ_{TSPR} (day 30) (nm)	% change in λ_{TSPR}
DI water	793	741	06.5	514	516	0.4
Pluronic F-127	790	764	03.3	513	531	3.5
CTAB	781	681	12.8	514	520	1.2
GS	803	570	29.0	513	531	3.5

Table 5.3 Effect of aging on the absorption maximum of LSPR and TSPR bands of GNRs preserved in DI water, pluronic F-127, CTAB and GS.

Medium	A_{LSPR} (day 0)	A_{LSPR} (day 30)	% change in A_{LSPR}	A_{TSPR} (day 0)	A_{TSPR} (day 30)	% change in A_{TSPR}
DI water	0.30	0.37	22.8	0.10	0.14	29.2
Pluronic F-127	0.19	0.12	37.6	0.07	0.06	08.1
CTAB	0.09	0.12	31.4	0.04	0.08	48.1
GS	0.28	1.16	76.7	0.08	1.53	94.5

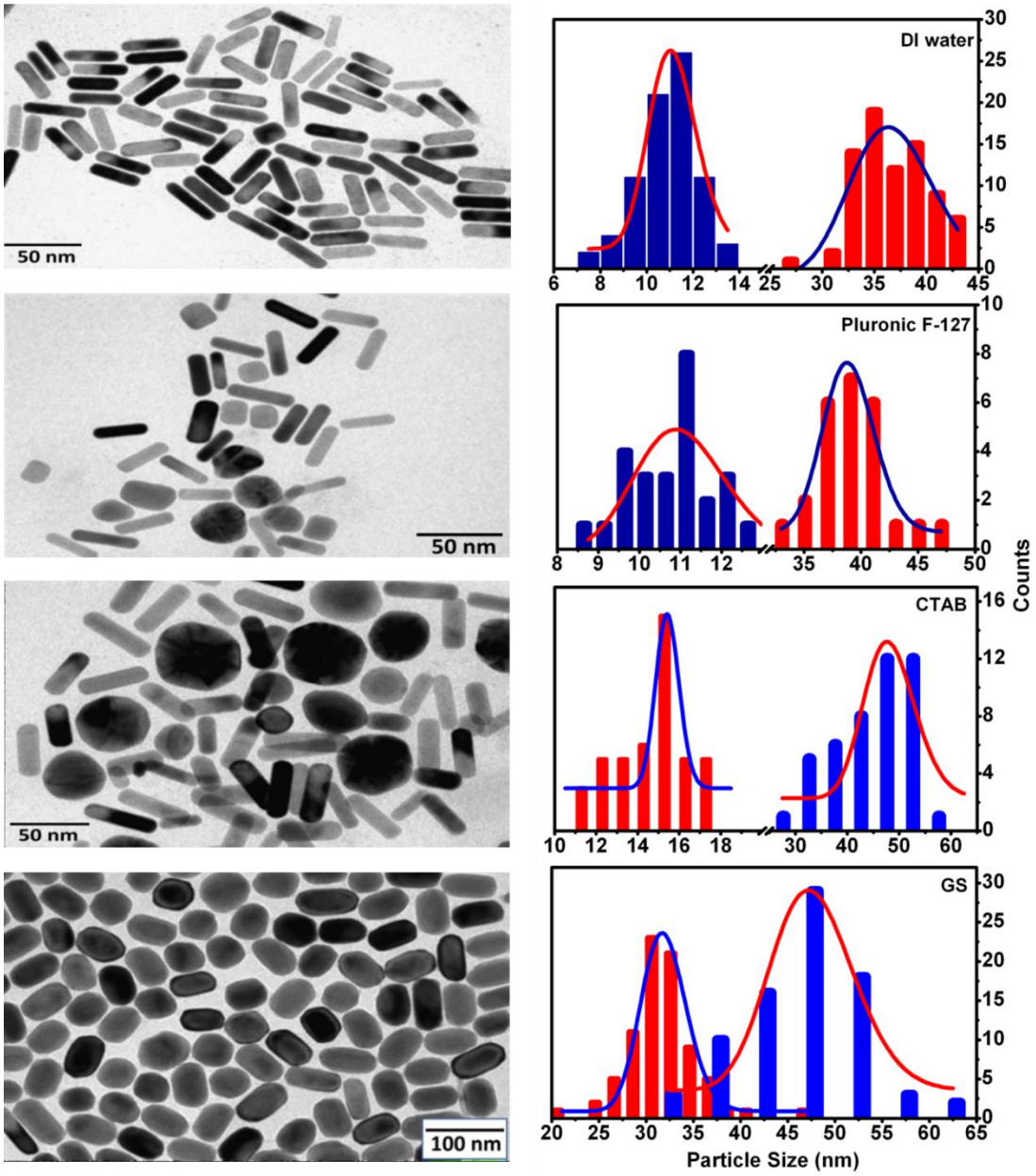

Fig. 5.6 TEM micrographs and corresponding size distribution histograms of GNRs preserved in DI water, pluronic F-127, CTAB and GS for 30 days.

Table 5.4 Effect of aging on physical size of GNRs preserved for 30 days in in DI water, pluronic F-127, CTAB and GS.

Medium	D (long axis) nm	D (short axis) nm	Aspect ratio
DI water	36.78 ± 0.62	11.12 ± 0.11	3.3
Pluronic F-127	38.90 ± 0.27	11.00 ± 0.33	3.5
CTAB	48.14 ± 1.65	15.42 ± 0.22	3.1
GS	47.60 ± 0.77	31.86 ± 0.11	1.5

5.2.2 Stability of GNRs

Colloidal stability of GNRs in different medium depends on the interactions of the medium with the surfactant. The reversal of nanorod growth i.e. “unzipping” is responsible for the deformation of GNRs morphology when preserved in GS. In the proposed unzipping mechanism, it is assumed that Ag^+ physi-adsorbed on the side facets of GNRs. These silver ions may desorb from the sides of nanorods during the aging. Once the silver ions desorb, the electrostatically stable $CTA^+–Br^––Ag^+$ complex gets destroyed (**Fig. 5.7**). Hence, CTAB ligands start desorbing from the sides of the nanorods. This leads to the deposition of gold atoms from the end facets to the side facets of the GNRs [19]. The anisotropic nanoparticles formed by the kinetic control are unstable and they slowly transform into the thermodynamically favourable shape through an aging process. This process is governed by the thermodynamics of the system and it eventually leads to the formation of spherical morphology of gold nanoparticles [20]. The zipping mechanism in case of GNRs preserved in CTAB is relatively slow as compared to GNRs preserved in GS. CTAB preserved GNRs undergo CTAB-CTAB bilayers rearrangement. Lower concentration of CTAB bilayers on GNRs’ surface can lead to the particle aggregation (**Fig. 5.7**). When CTAB concentration on the surface of GNRs is too low, the double layer structure begins to disintegrate which forces the free CTAB in the solution to bind with the GNRs’ surface. Since this process is rapid, each CTAB will be shared by two or more atoms. CTAB bilayer rearrangement also forces CTAB desorption from the sides of nanorods which then eventually results into desorption of gold atoms from the end faces of GNRs [21].

Water molecules can ionise into H^+ and $OH^–$ due to electric field fluctuations between neighbouring H_2O molecules. It is proposed here that H^+ ions sits along the $Br^–$ anions of the $CTA^+–Br^–$ pair of the CTAB bilayer across the length of the GNR. Whereas, $OH^–$ ions cap the CTA^+ head group of the $CTA^+–Br^––Ag^+$ complex, thus enhancing the rigidity of surfactant bilayer, which prevents unzipping and maximizing the stability of GNRs preserved in DI.

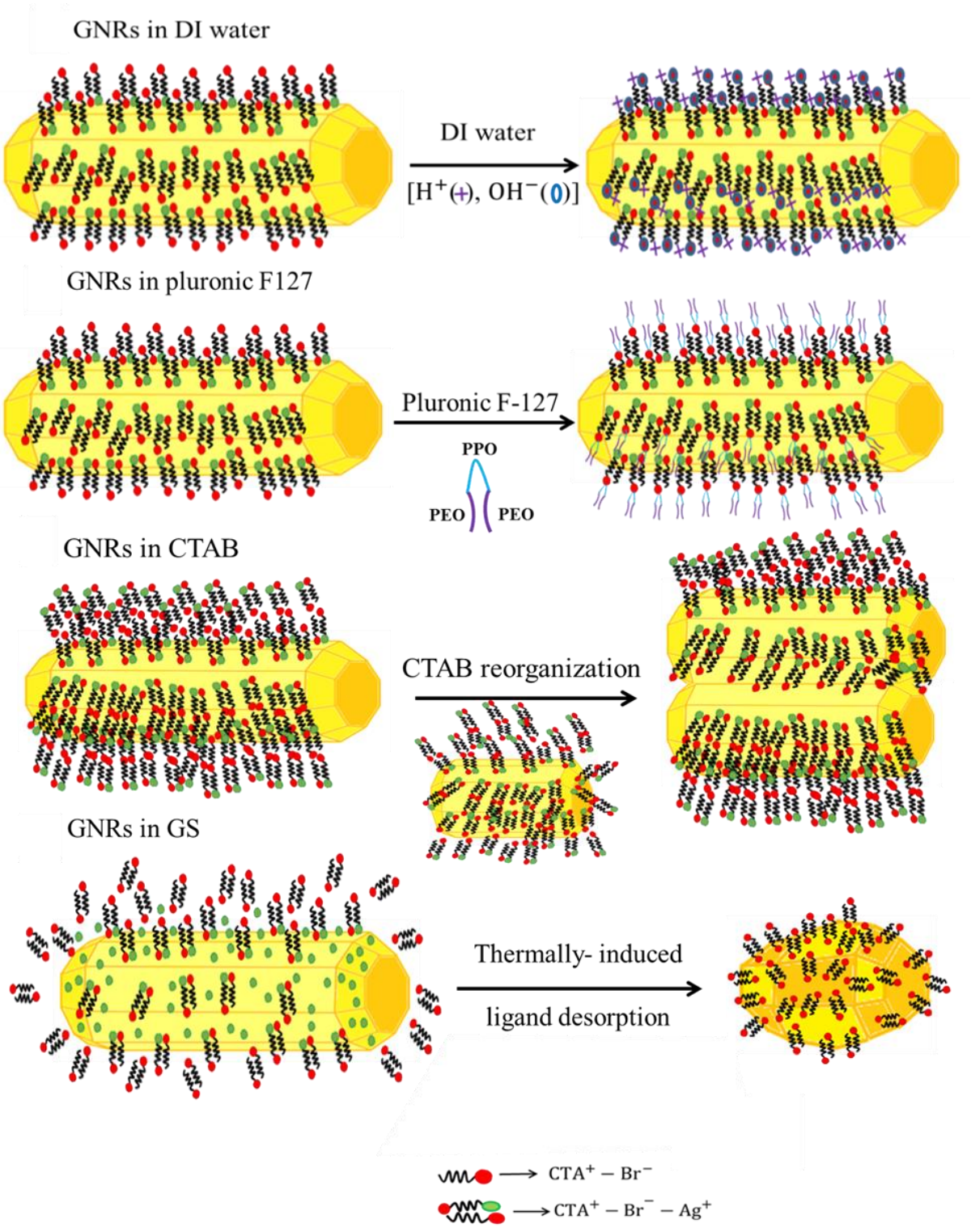

Fig. 5.7 Proposed unzipping mechanism responsible for difference in colloidal stability of GNRs preserved in DI water, pluronic F-127, CTAB and GS.

Pluronic is a commercially available non-ionic triblock polymer with a hydrophobic core chain of poly(propyleneoxide) (PPO) sandwiched at its ends by two hydrophilic blocks of poly(ethylene oxide) [22, 23]. GNRs preserved in pluronic F-127 also have moderate stability. The hydrophobic PPO block of pluronic binds with the hydrophobic tail of CTAB and forms a stable CTAB–pluronic F-127 complex (**Fig. 5.7**) [24, 25]. Formation of CTAB-pluronic F-127 complex improves the dispersion stability of GNRs in the colloidal phase and minimizes the probability of aggregation induced deformation in GNRs. In addition, it also decreases the electrostatic attraction between neighbouring nanorods and thus improves their structural stability as well.

5.2.3 Effect of pH

To investigate the effect of pH of the medium on the stability of nanorods, GNRs are synthesized by seedless method by using BDAC-CTAB co-surfactants as described in chapter 4. Four samples of GNRs with pH 1.3, 1.5, 1.7 and 2.0 were prepared simultaneously under identical conditions. After centrifugations each sample was preserved in ambient conditions in DI water. DI water was chosen as a colloidal medium for storage because maximum stability of GNRs was observed in DI water. These GNRs were examined by UV-Visible-NIR spectroscopy at periodic intervals for 180 days (**Fig. 5.8**).

Effect of pH of the colloidal medium on the spectral stability of GNRs was evaluated on the basis of variation in their LSPR band positions. Variation in LSPR band positions of GNRs prepared at different pH by seedless method and preserved in DI water as function of time is shown in **Fig. 5.9**. Maximum blue shift (874 to 867 nm) is observed in the LSPR band of GNRs synthesized at pH 2.0, followed by pH 1.7 (983 to 978 nm) and pH 1.5 (1160 to 1156 nm). Good spectral stability of LSPR band was observed in GNRs synthesized at pH 1.3 (1280 to 1278 nm). Percentage change in the LSPR band position is maximum (0.8%) at pH 2.0 and it is minimum at pH 1.3 (0.15%). These results are summarized in **Table 5.5**. Continuous but very slow decrease in the absorbance of LSPR band is observed in all the four samples of GNRs (**Fig. 5.10**). The percentage change in absorbance is 13.0% for GNRs preserved at pH 2.0 and 4.9% for that at pH 1.3. Results are summarized in **Table 5.6**. Decrease in the spectral shift of GNRs synthesized at lower pH shows that GNRs have higher spectra and structural stability at low pH. Hence, GNRs preserved in DI water at pH 1.3 are

least prone to aging induced deformation. This might be because of the reduced rate of GNRs growth at lower pH leading to perfect growth. Further investigations are required to establish the process leading to this exceptional stability of GNRs against aging at low pH. Effect of pH on the hydrodynamic size of the GNRs could not be monitored due to high surfactant concentration in the colloidal medium.

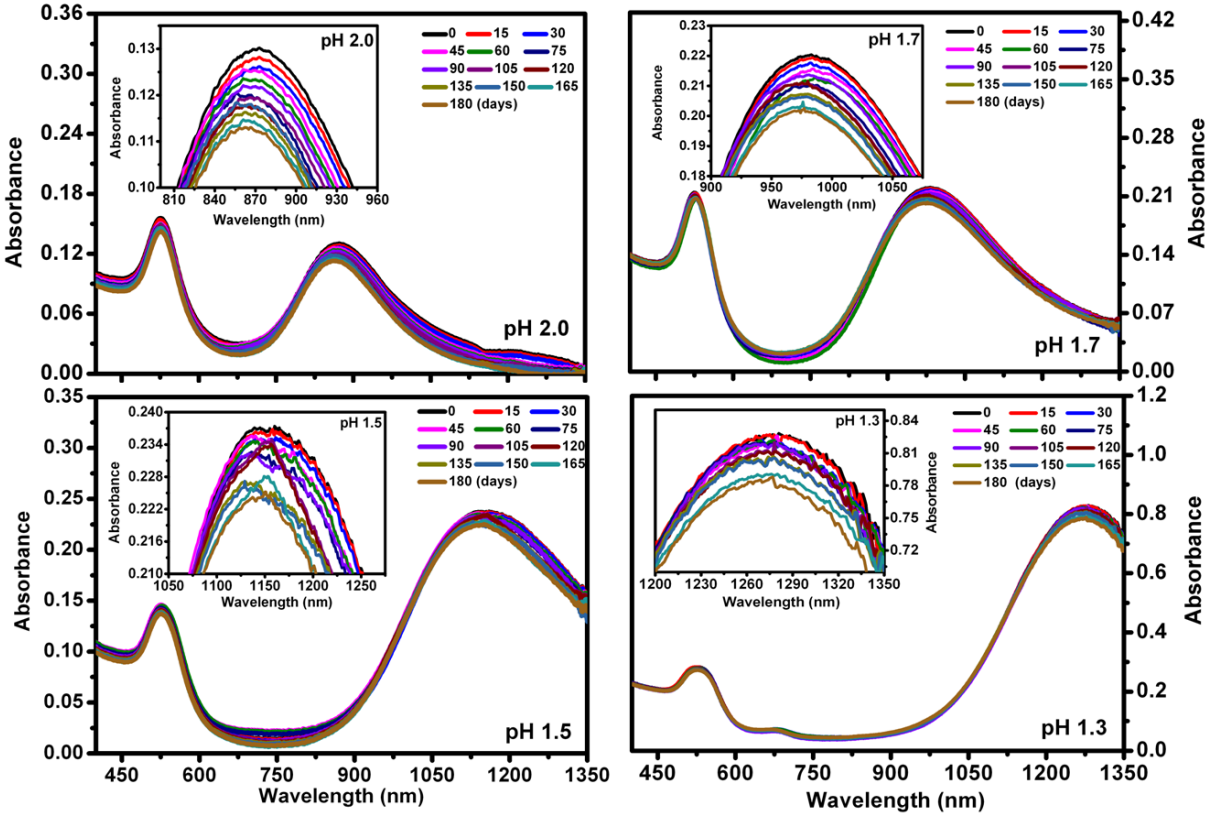

Fig. 5.8 UV-Visible absorption spectra of GNRs prepared at pH 1.3, 1.5, 1.7 and 2.0. Insets show the enlarged image of LSPR band in each case for clear comparison of the spectral shifts observed in their plasmon resonance bands.

Table 5.5 Spectral Shift in the LSPR band positions of GNRs prepared at pH 1.3, 1.5, 1.7 and 2.0.

pH	λ_{LSPR}(nm) (day 0)	λ_{LSPR}(nm) (day 180)	% change in λ_{LSPR}
1.3	1295	1293	0.15
1.5	1160	1156	0.35
1.7	983	978	0.50
2.0	874	867	0.80

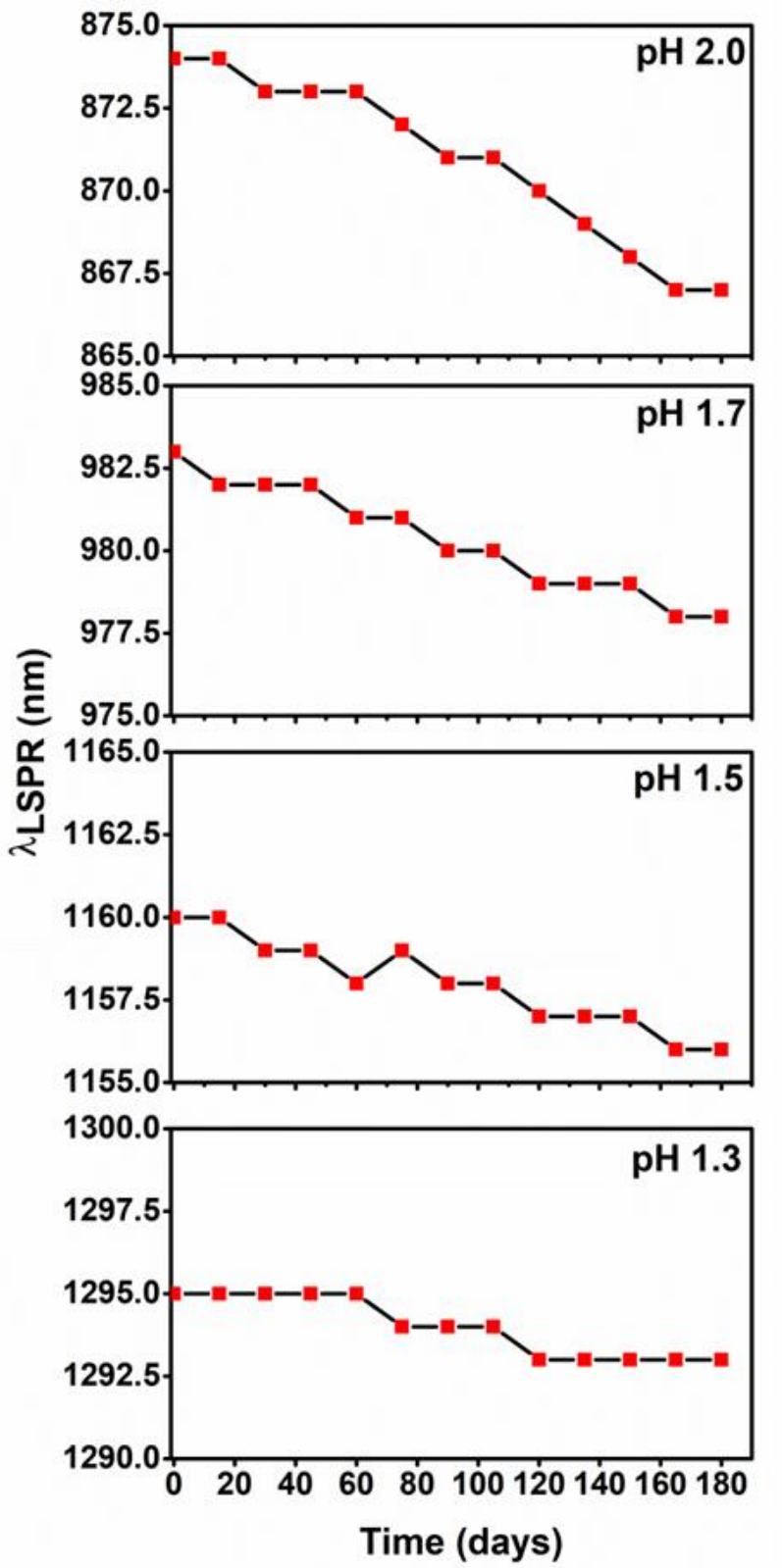

Fig. 5.9 Effect of aging on the LSPR bands of GNRs when prepared in DI water at pH 1.3, 1.5, 1.7 and 2.0 for 180 days.

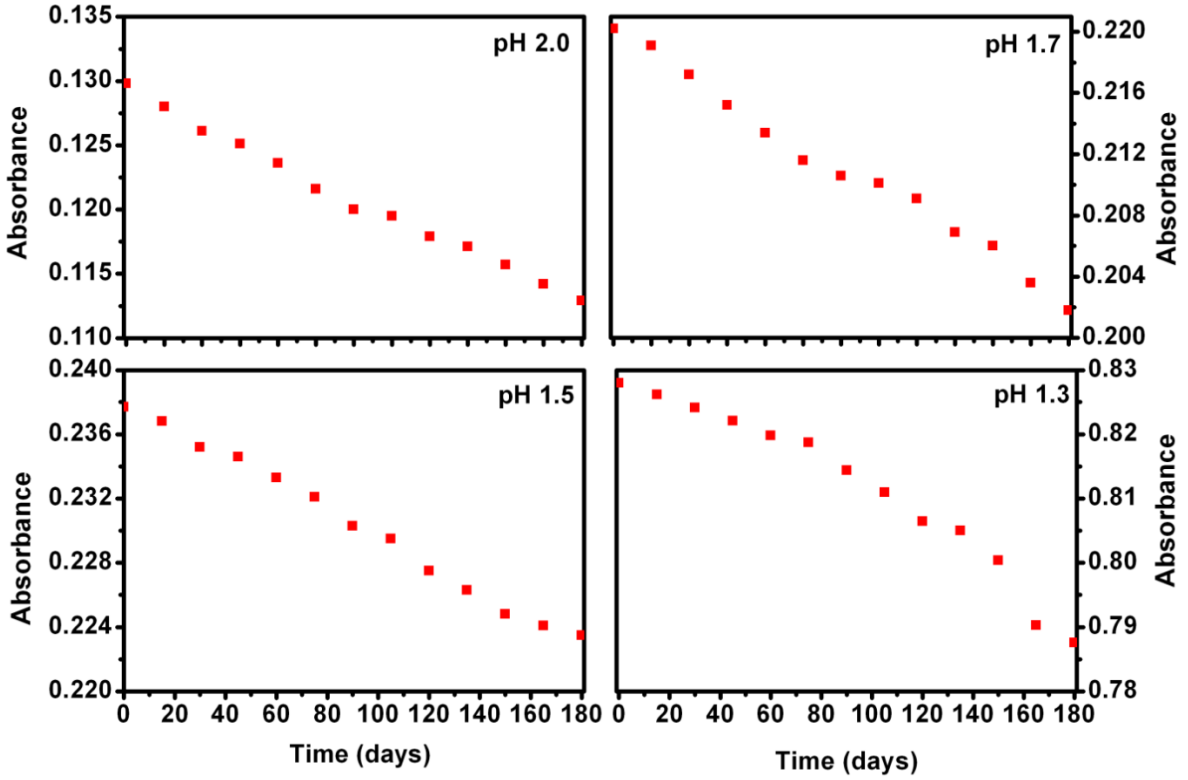

Fig 5.10 Effect of aging on the absorption maximum of LSPR band of GNRs prepared at pH 1.3, 1.5, 1.7 and 2.0 for 180 days.

Table 5.6 Effect of aging on the absorbance of LSPR band of GNRs prepared at pH 1.3, 1.5, 1.7 and 2.0.

pH	A_{LSPR} (day 0) (nm)	A_{LSPR} (day 180) (nm)	% change in A_{LSPR}
1.3	0.82	0.78	4.9
1.5	0.23	0.22	5.9
1.7	0.22	0.20	8.3
2.0	0.12	0.11	13.0

5.3 COLLOIDAL STABILITY OF GNPs

5.3.1 Effect of Colloidal Medium

GNPs were prepared by seed-mediated method as described in chapter 3. Three samples of GNPs were prepared simultaneously under identical conditions. As-synthesized GNPs were separated from the growth medium by centrifugation @ 6000 rpm for 10 minutes. After centrifugation GNPs were preserved under ambient conditions either in DI water, or in pluronic F-127, or in growth solution (GS). These colloidal suspensions of GNRs were

examined at periodic intervals by UV-Visible spectroscopy for 42 days. Effect of colloidal medium on the stability of GNPs was evaluated on the basis of variation in their SPR bands. Samples were neither diluted nor sonicated prior to UV-Visible spectroscopy.

UV-visible spectra of GNPs preserved in DI water, pluronic F-127 and GS are recorded at periodic intervals for 42 days are shown in **Fig. 5.11**. GNPs preserved in DI water loses their colloidal stability within 21 days as evidenced from the shift in the in-plane quadrupole resonance until it overlaps on the out-of-plane quadrupole resonance (**Fig. 5.12**). This is because of deformation in morphology of nanoparticles from plates to spheres. A blue shift (921 to 830 nm) 91 nm was observed in the in-plane resonance band of GNPs preserved in the GS. In-plane resonance band shifted from 805 to 818 nm when preserved in pluronic F-127. No further shift in the plasmon resonance band of pluronic stabilized GNPs were observed indicating the high stability of GNPs in pluronic F-127. An impressive stability of SPR band at 818 nm is observed over first 21 days with increase in absorption from 0.35 to 1. From 28 day onwards, no further increase in the absorption of plasmon band is observed.

The spectral shift in the plasmon band positions and the absorbance maximum of GNPs recorded for 42 days are shown in **Fig. 5.12 and Fig. 5.13** respectively. In-plane plasmon resonance band GNPs preserved in DI water disappear within 21 days. What is observed beyond this is only out-of-plane resonance with decreased absorbance. This is because of the deformation of anisotropic plate like structure of GNRs into the isotropic spheres. Out -of-plane resonance band of GNPs preserved in DI water shows small shift from 531 to 536 nm.

GNPs preserved in GS show a blue shift (921 to 830 nm) of 91 nm in the in-plane resonance band in 42 days (**Fig. 5.12**). This shift is 9.8%. It is still quite low as compared to that observed for GNPs preserved in DI water. A blue shift of 0.5% is observed in out-of-plane resonance band of GNPs when preserved in GS. GNPs when preserved in pluronic F-127 show better stability as compared to those preserved in GS and DI water. A red shift of 17 nm (805 nm to 822 nm) is observed in the in-plane resonance band of GNPs during first 14 days (**Fig. 5.12**). After this the in-plane resonance band was stable at 815 ± 3 nm. Percentage change in the in-plane resonance band is only 1.5%. Out-of-plane resonance band

also undergoes a red shift by1.3% (**Table 5.7**). GNRs preserved in pluronic F-127 have better spectral and structural stability as compared to those preserved in DI water or GS.

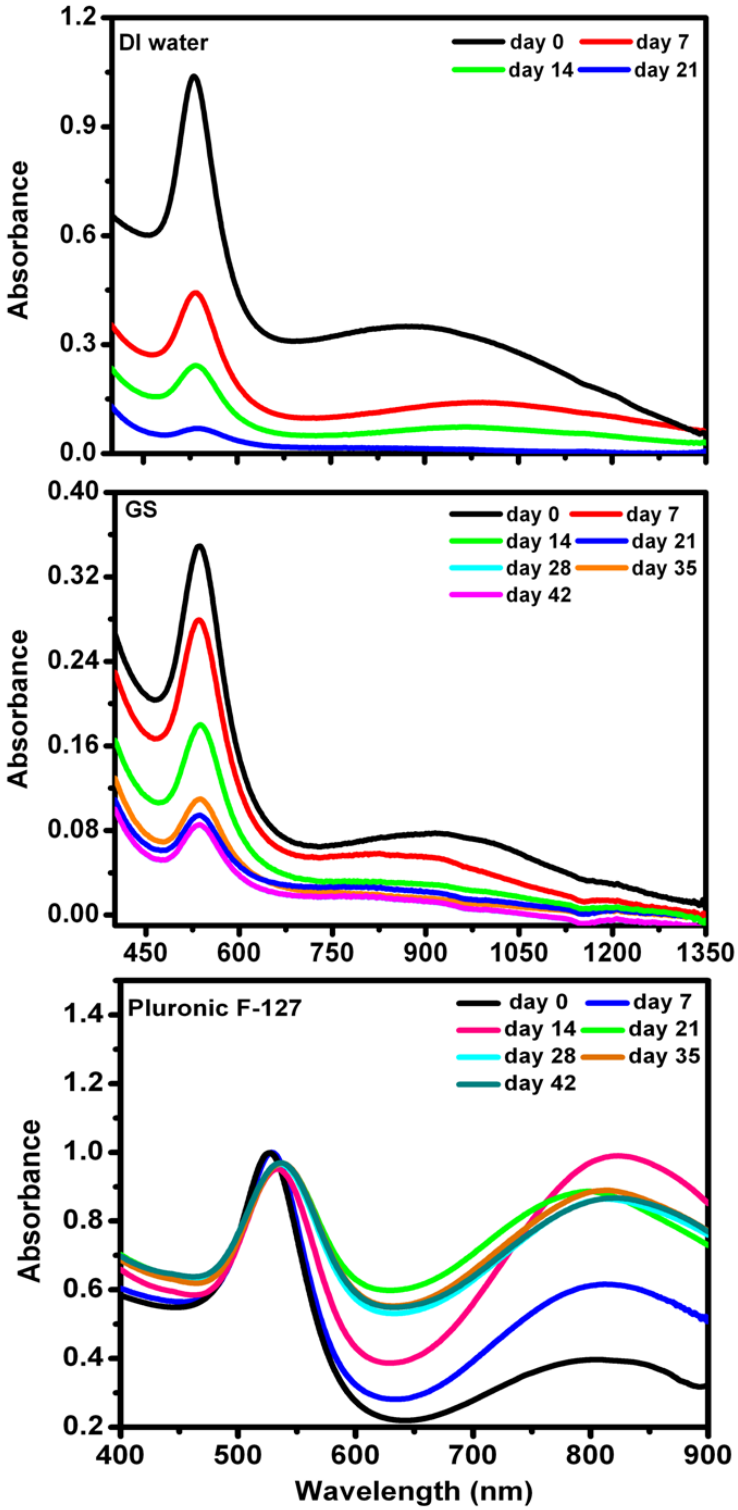

Fig. 5.11 UV-Visible absorption spectra of GNPs preserved DI water, pluronic F-127 and GS.

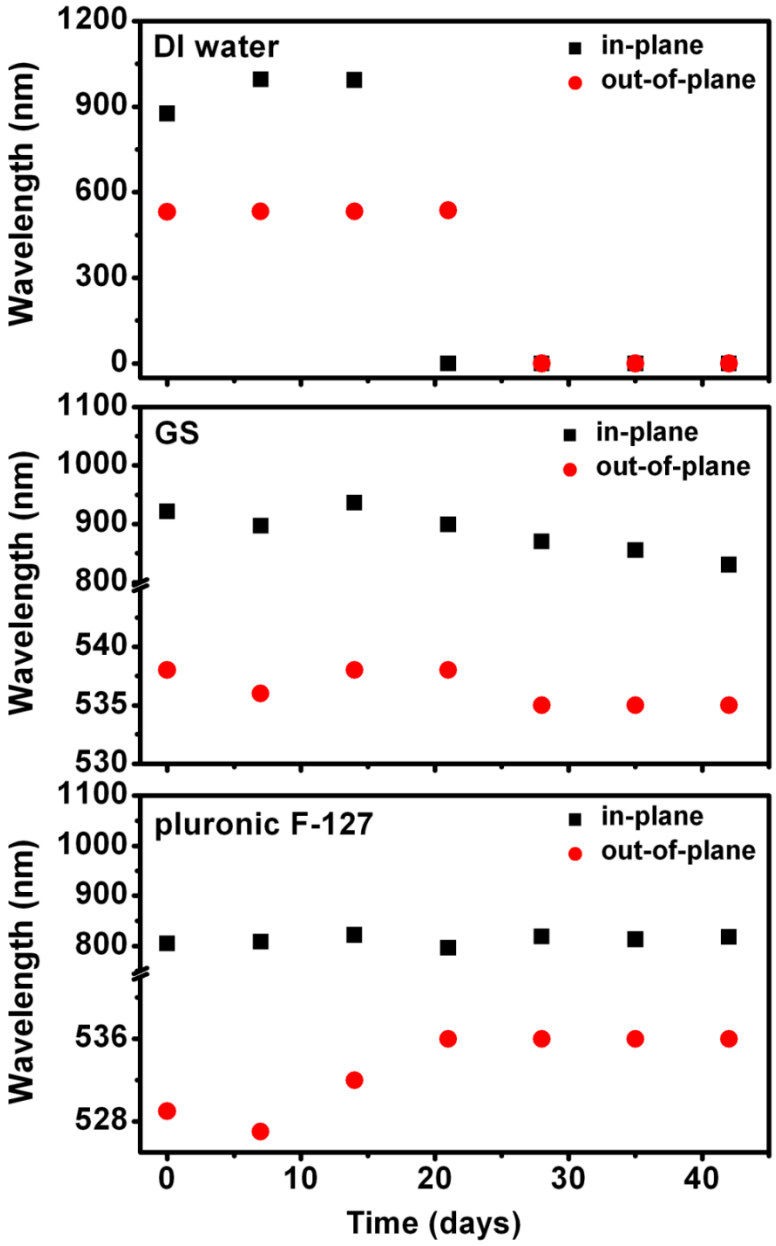

Fig. 5.12 Effect of aging on the in-plane and out-of-plane resonance band positions of GNPs preserved in DI water, pluronic F-127 and GS.

In terms of spectral intensities of in-plane and out-of-plane resonance bands amongst GNPs preserved in different media, the percentage change in absorbance of in-plane and out-of-plane resonance band is minimum (54.2% and 3.3% respectively) for GNPs preserved in pluronic F-127 (**Table 5.8**). The percentage change in the spectral intensities of GNPs preserved in GS is 82.2% and 75.5% for in-plane and out-of-plane resonance bands, respectively (**Table 5.8**). Large change in the intensity of plasmon resonance bands of GNPs

preserved in DI water was also observed prior to they transform their morphology from plates to spheres.

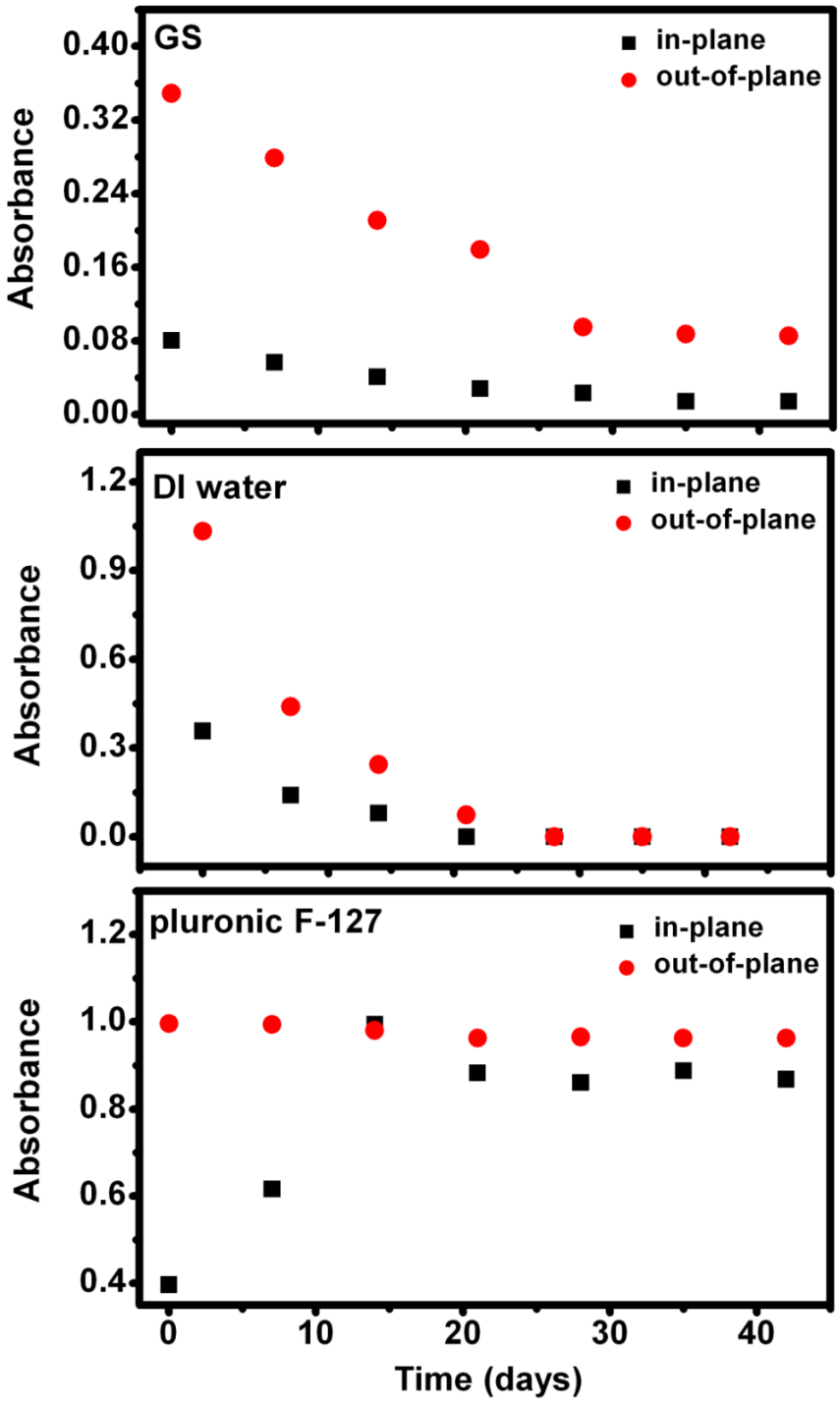

Fig. 5.13 Effect of aging on the absorption maximum of in-plane and out-of-plane resonance bands of GNPs when preserved in DI water, pluronic F-127 and GS.

Table 5.7 Effect of aging on the in-plane (λ_i) and out-of-plane (λ_o) band positions of GNPs preserved in DI water, pluronic F-127 and GS.

Medium	λ_i (nm) day 0	λ_i (nm) day 42	% change in λ_i	λ_o (nm) day 0	λ_o (nm) day 42	% change in λ_o
DI water	875	-	-	531	536	0.93
GS	921	830	9.8	538	535	0.55
Pluronic F-127	805	818	1.5	529	536	1.30

Table 5.8 Effect of aging on the absorption maximum of in-plane (A_i) and out-of-plane (A_o) band positions of GNPs preserved in DI water, pluronic F-127 and GS.

Medium	A_i (day 0)	A_i (day 42)	% change in A_i	A_o (day 0)	A_o (day 42)	% change in A_o
DI water	0.35	-	-	1.03	0.07	92.8
GS	0.08	0.01	82.2	0.34	0.08	75.5
Pluronic F-127	0.39	0.86	54.2	0.99	0.96	03.3

5.4 CYTOTOXICITY OF GOLD NANOSTRUCTURES

Size, shape and concentration dependent cell viability of as-synthesized GNRs and GNPs were determined on RAW 264.7 macrophage cell lines using MTT assay. Schematic of protocol of cell viability test by MTT assays is shown in **Fig. 5.14**. Cytotoxicity tests were carried out in 96-well microtiter plates. Cells were cultured in Dulbecco's modified Eagle's medium (DMEM). Cells were maintained at 37 ^oC supplemented with 5% CO_2. Culture media were changed every 2 days. Cells were trypsinzed on attaining 80-90% confluency. Each well in microtiter plate was seeded with 2 $X10^4$ cells (step 1). Different concentrations of as-synthesized gold nanoparticles (0.00005, 0.00025, 0.0005, 0.00075, 0.001, 0.005, 0.01, 0.05, 0.1, 0.5 and 1 μg/mL) were added into the well and incubated for 24 h (step 2-3). After incubation, 20 μL of the MTT reagent was added to each well (step 4). The plate was again incubated for another 4 h. The viability of the cells was determined from the amount of formazan crystals formed (step 5). To solubilise the formazan crystals, 100 μL of DMSO was added to each well and the absorbance of formazan was recorded at 570 nm on ELISA plate reader. The wells having only media and nanoparticles (no cells) were treated as blanks. Each experiment was performed in triplicates. Cell viability was calculated by using the following equation:

$$\% \text{ cell viability} = \frac{A_C - A_S}{A_C} \times 100 \qquad 5.1$$

Where A_c and A_s are the absorbance (of formazan) of control and sample measured at 570 nm [26].

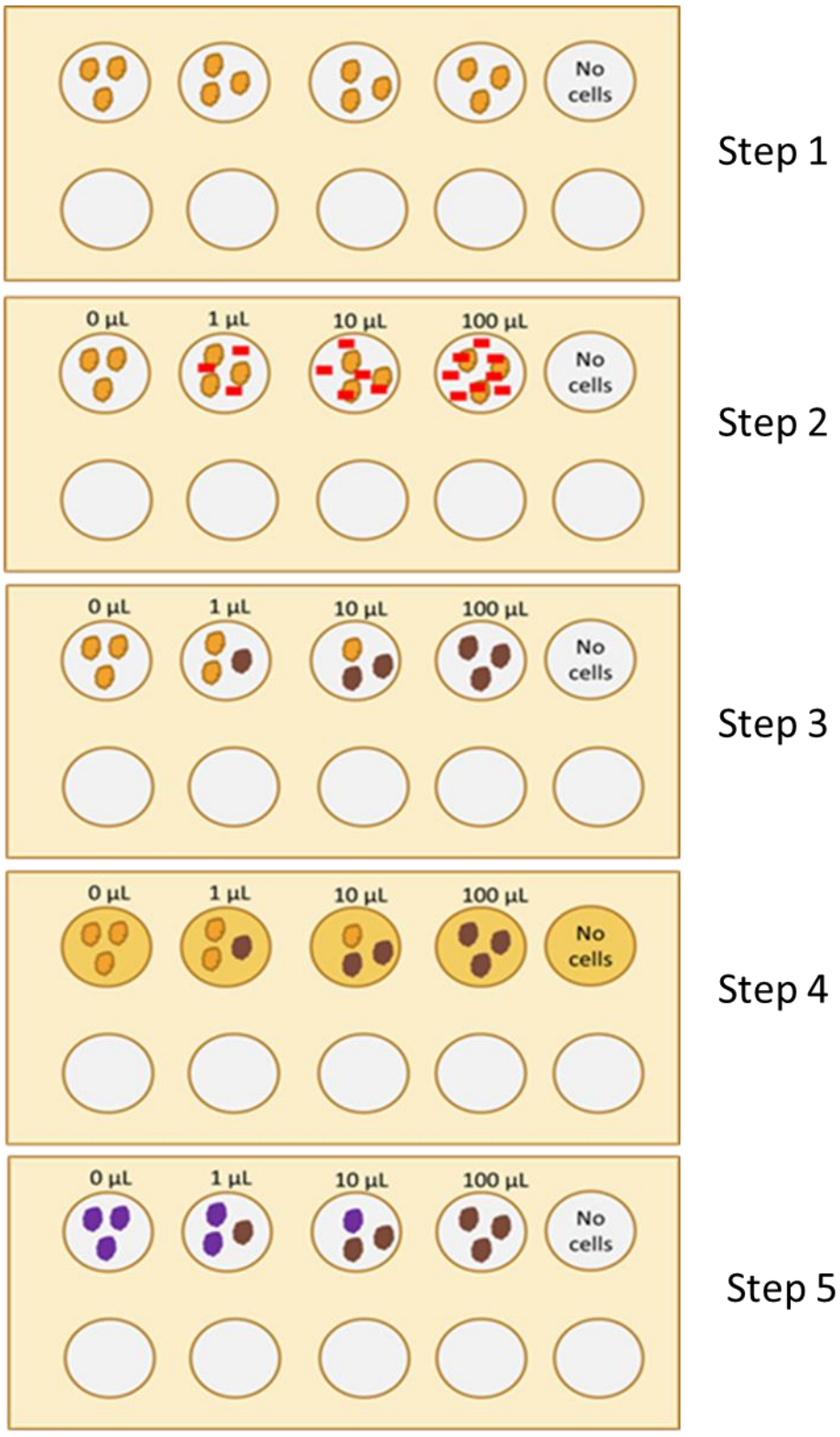

Fig. 5.14 Schematics diagram of protocol of cell viability test MTT assays.

5.4.1 Cytotoxicity of GNRs

Cytotoxicity of GNRs prepared by seedless approach with aspect ratios 8.9, 7.8, 5.9, 4.8 and 3.8 has been evaluated by cell viability assays. The % cell viability of RAW 264.7 cells against as-synthesized GNRs as function of their concentration is shown in **Fig. 5.15**. GNRs show size and concentration dependent toxicity against RAW 264.7 macrophage cells. Cell viability increases with decrease in concentration of GNRs irrespective of their aspect ratios. GNRs with aspect ratio's 3.8 and 4.8 show acute cytotoxicity at concentrations 1-10 μg/mL, where, the cells remained only 10-60% viable (**Fig. 5.15 (d-e)**). Cell viability for GNRs with aspect ratio 3.8, 4.8 and 5.9 increase beyond 60% as the concentration decreases below 1 μg/mL. At small concentrations (≤ 0.05 μg/mL), cell viability increases above 80 % for GNRs having aspect ratio 3.8-5.9. GNRs with aspect ratio 7.8 and 8.9 shows higher cell viability at same concentrations as compared to those for 3.8, 4.8 and 5.9 aspect ratio GNRs (**Fig. 5.15 (a,b)**). Cell viability is 90 % for both 7.8 and 8.9 aspect ratio GNRs at 1 μg/mL concentration (**Fig. 5.15 (a,b)**).

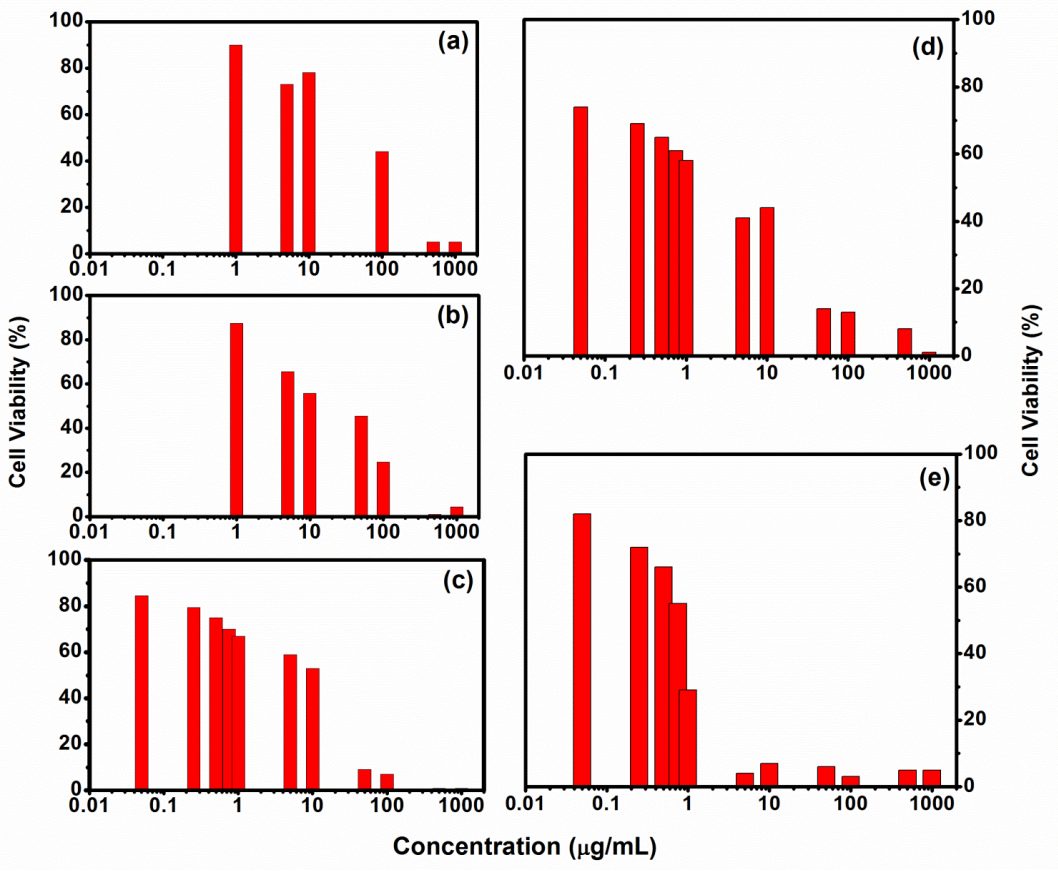

Fig. 5.15 % cell viability of RAW 264.7 macrophage cell lines as a function of GNRs concentration having aspect ratios (a) 8.9, (b) 7.8, (c) 5.9, (d) 4.8 and (e) 3.8.

5.4.2 Cytotoxicity of GNPs

Cell viability of as-synthesized GNPs preserved in pluronic F-127 was also determined by cell viability tests as explained in section 5.4. % cell viability as a function of concentration of GNPs is measured (**Fig. 5.16**). % cell viability varies between 40%- 60% at all tested concentrations. Even at higher concentrations (1000 μg/mL) the % cell viability of macrophage cell lines against GNPs is 50%. The toxicity of GNPs against macrophage cell lines does not show strong dependence on their concentration. This might be because of the presence of pluronic F-127 as passive layer on the surface of GNPs. Pluronic F-127 is known to be biocompatible and hence effectively suppress the toxicity of GNPs.

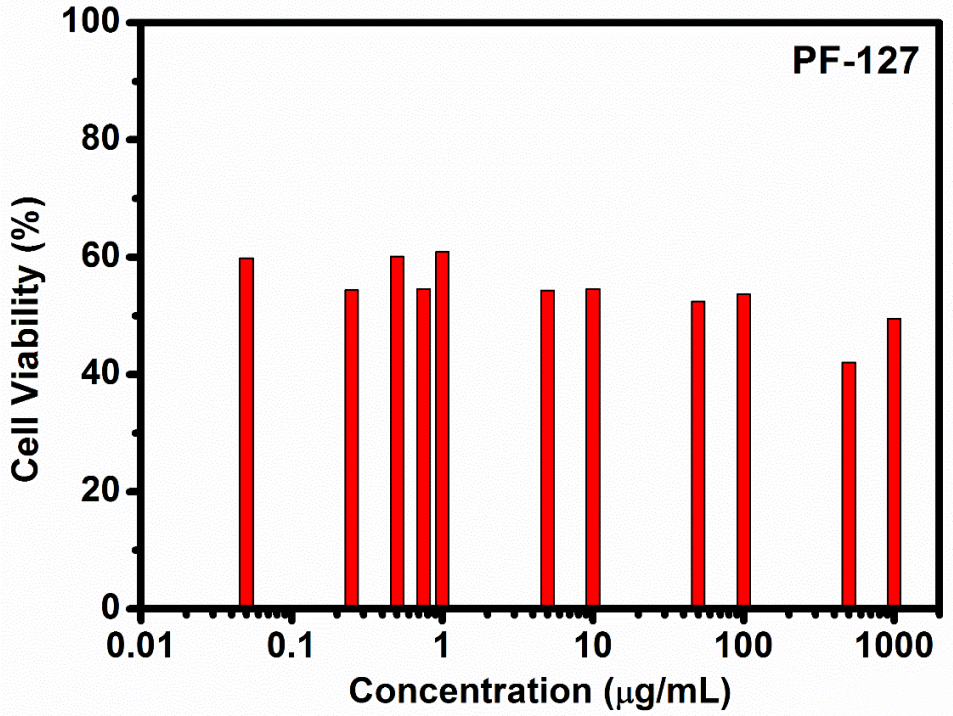

Fig. 5.16 % cell viability of RAW 264.7 macrophage cells lines as a function concentration of GNPs preserved in pluronic F-127.

To understand the effect of size, shape and surfactants on the biocompatibility of gold nanostructures, the results of % cell viability of macrophage cell lines against two GNRs (A.R. 8.9 and 3.8) and GNPs were compared (**Fig. 5.17**). The cell viability of GNRs with aspect ratio 8.9 is highest at all concentrations as compared to GNRs with aspect ratio 3.8. This result clearly suggests that the biocompatibility of GNRs increases with increase in their aspect ratio (i.e. size). Smaller GNRs are more toxic as compared to larger sized GNRs. This

observation is in good agreement with those reported by Sabine et al. [27]. They report the cell viability of CTAB-coated GNRs with aspect ratio ~ 3.9 to be 30%, 20% and 7% at 1, 10 and 100 μg/mL concentrations of GNRs. Toxicology of nanoparticles depends on the surface area of the nanoparticles which increases exponentially with decrease in the particle size [28]. High exposed area promotes release of metal ions from the nanoparticles as compared to their bulk counterparts [29]. Pluronic F-127 stabilized GNPs exhibits enhanced cell viability as compared to low aspect ratio GNRs at 1, 10, 100 μg/mL concentrations. The toxicity of GNPs as compared to high aspect ratio GNRs is high at low concentrations (≤ 10 μg/mL). Interestingly when compared at higher concentrations (100 μg/mL); the cell viability of macrophage cell lines is higher as compared to GNRs irrespective of their size. This might be due to the effective suppression of toxicity of gold core by the presence of biocompatible film of pluronic F-127 in the surface of GNPs.

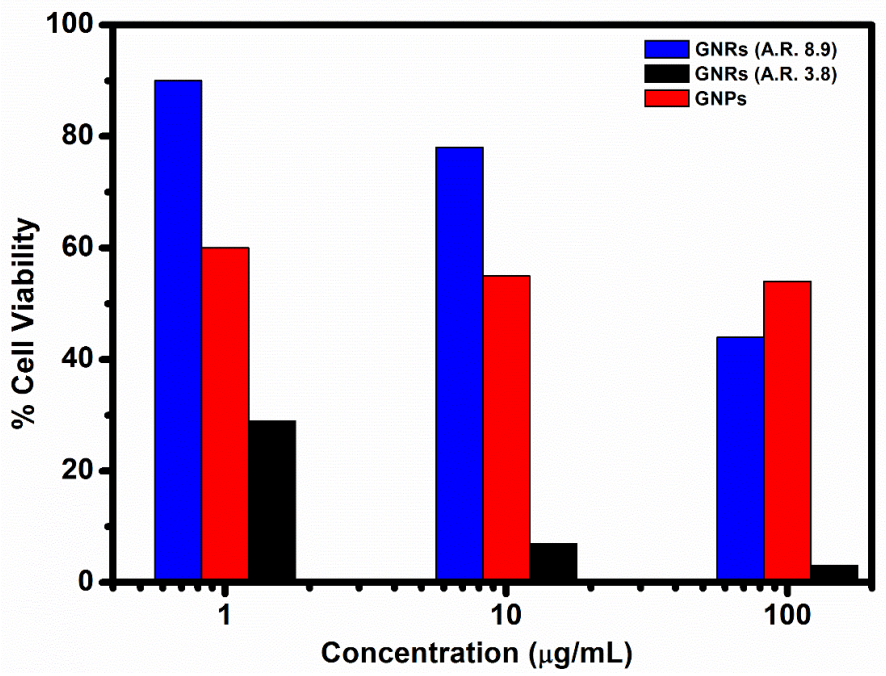

Fig. 5.17 Comparison of % cell viability of RAW 264.7 macrophage cell lines against GNRs (A.R. 8.9 and 3.8) and GNPs at concentrations of 1, 10 and 100 μg/mL.

References:

1. N.R. Jana, L. Gearheart, C. J. Murphy, *Chem. Mater*., **2001**, 13, 2313-2322.
2. B. Nikoobakht, M.A. El-Sayed, *Chem. Mater*., **2003**, 15, 1957-1962.
3. Z. Yang, Z. Li, X. Lu, F. He, X. Zhu, Y. Ma, R. He, F. Gao, W. Ni, Y. Yi, *Nano-Micro Lett*., **2017**, 9, -13.
4. X. Fan, Z.R. Guo, J.M. Hong, Y. Zhang, J.N. Zhang, N. Gu, *Nanotechnology*, **2010**, 21, 105602-105609.
5. C.L. John, S.L. Strating, K.A. Shephard, J.X. Zhao, *RSC Adv*., **2013**, 3, 10909-10918.
6. K. Imura, T. Nagahara, H. Okamoto, *J. Am. Chem. Soc*., **2004**, 126, 12730-12731.
7. P.C. Hiemenz, R. Rajagopalan, *Principles of Colloid and Surface Chemistry*, **1997**, third ed., Marcel Dekker, New York.
8. J.H. Lyklema, *Fundamentals of Interface and Colloid Science, in: Particulate Colloids*, **2005**, vol. IV, Amsterdam.
9. P. Pandey, S.P. Singh, S.K. Arya, V. Gupta, M. Datta, S. Singh, B.D. Malhotra, *Langmuir*, **2007**, 23, 3333–3337
10. G.P Luke, A. Bashyam, K.A Homan, S. Makhija, Y.S Chen, S.Y Emelianov, *Nanotechnology*, **2013**, 24, 45-51.
11. Y.S. Chen, Y.C. Hung, I. Liau, G.S. Huang, *Nanoscale Res Lett.*, **2009**, 4, 858–864.
12. Z. Li, S. Tang, B. Wang, Y. Li, H. Huang, H. Wang, P. Li, C. Li, P.K. Chu, X.F.Yu, *ACS Biomater. Sci. Eng*., **2016**, 2, 5, 789–797.
13. Y. Zhang, D. Xu, W. Li, J. Yu, Y. Chen, *J. Nanomater*., **2012**, 2012, 375496, 1-7.
14. J. Malgorzata, R. Smith, *Encyclopedia of Nanotechnology*, **2012**, 645-652.
15. S. Vijayakumar, S. Ganesan, *J. Nanomater*, **2012**, 2012, 734398, 1-9.
16. N. Li, P. Zhao, D. Astruc, *Angew. Chem. Int. Ed*., **2014**, 53, 1756 – 1789.
17. J. Stone, S. Jackson, D. Wright. *Interdiscip Rev Nanomed Nanobiotechnol*., **2011**, 3, 100-109.
18. Z. Ya, M.H. Xing, X.Y. Ping, L. Bo, L. Wei, C.Y. Zhao, *Chin. Sci. Bull.*, **2013**, 58, 21, 2530–2536.
19. K. C. Ng, W. Cheng, *Nanotechnology*, **2012**, 23, 105602.
20. D. Goh, T. Gong, U.S. Dinish, K.K. Maiti, C.Y. Fu, K.T. Yong, M. Olivo, *Plasmonics*., **2012**, 7, 595.
21. A.M. Alkilany, P.K. Nagaria, M.D. Wyatt, C.J. Murphy, *Langmuir*, **2010**, 26, 9328–9333.
22. M. Iqbal, Y.I. Chung, G. Tae, *J. Mater. Chem*., **2007**, 17, 335-342.
23. F.S. Khattak, R. Bhatia, C.R. Susan, *Tissue Eng*., **2005**, 11, 974-983.
24. T. Sakai, P. Alexandridis, *Langmuir*., **2006**, 20, 8426-8430.
25. T. Sakai, P. Alexandridis, *Chem. Mater*., **2006**, 18, 2577-2583.
26. C.S. Yah, *Biomed. Res*., **2013,** 24, 400-413.
27. K. Turcheniuk, R. Boukherrouba, S.Szunerits, *J. Mater. Chem. B*, **2015**, 4301-4324.
28. J.K. Fard, S. Jafari, M.A. Eghbal, *Adv. Pharm. Bull*., **2015**, 5, 447-54.
29. S. Bakand, A. Hayes, *Int. J. Mol. Sci*., **2016**, 17, 929-932.

CHAPTER 6

CONCLUSIONS AND SCOPE FOR FUTURE WORK

6.1 CONCLUSIONS

6.1.1 Synthesis of GNRs and GNPs

Well dispersed, uniform gold nanoparticles (GNRs and GNPs) with controllable size and narrow size distribution are prepared by seed-mediated and seedless growth methods (**Fig. 6.1**). Nanoparticle's yield, their morphology, particle size and size distribution, uniformity and dispersity are strongly correlated with the concentration of the surfactant cum stabilizer (CTAB, BDAC, pluronic F-127), and gold precursor ($HAuCl_4$). Other kinetic parameters like, reducing agent(s), silver ion concentration and nature of seeds, play a vital role in the synthesis of well-defined, NIR responsive gold nanostructures. Optimized conditions have been laid down for the synthesis of GNRs and GNPs with moderate yield and tunable response deep into the NIR region. The plasmon band of GNRs can be tuned upto 1300 nm while for GNPs; this tunability is limited to 950.

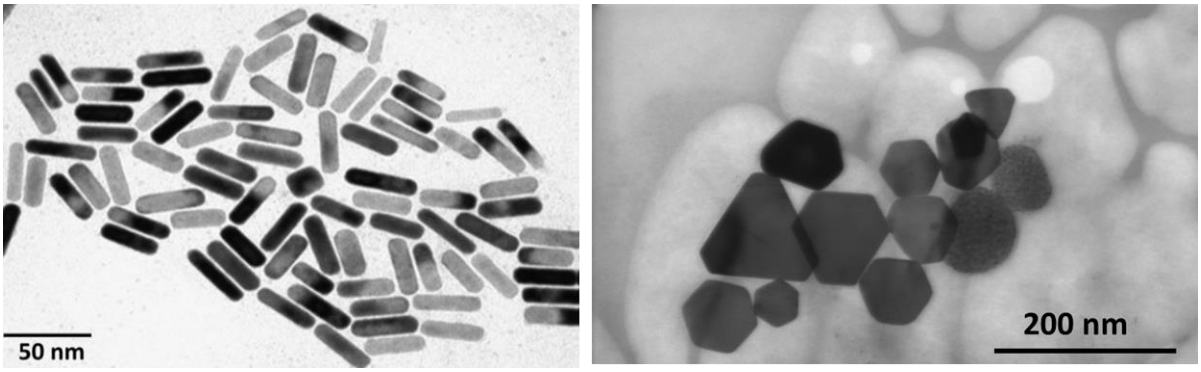

Fig. 6.1 TEM image of GNRs and GNPs synthesized under optimized conditions.

6.1.2 Tunability of GNRs and GNPs

Optical tunability of plasmon resonance band of GNRs has been achieved in both the synthesis approaches (**Fig 6.2**). In seeded route, optical tunability of LSPR band of GNRs has been achieved by serial additional of growth solution into presynthesized GNRs at periodic intervals. With this approach LSPR band could be tune upto 1150 nm. In seedless approach pH of the growth medium act as growth controlling agent which controls the dimensional

growth. By changing the pH of the growth solution from 2.0 to 1.3, the LSPR band of GNRs could be tuned from 780 – 1300 nm. A limited tunability of in-plane plasmon resonance band of GNPs has also been observed when synthesized by sequential seeded growth approach. However, tunability is limited to 900 – 960 nm only. No pH controlled tunability was achieved in GNPs when synthesized via seedless approach. A plausible mechanism responsible for impressive pH dependent dimensional and optical tunability in GNRs synthesized by seedless approach has also been proposed. In conclusion, GNRs have better tunability as compared to GNPs. No significant difference is observed in the tunability of GNRs prepared by seeded or seedless approach. However, considering the high yield and ease of preparation, GNRs synthesized by seed approach is better match for intended application.

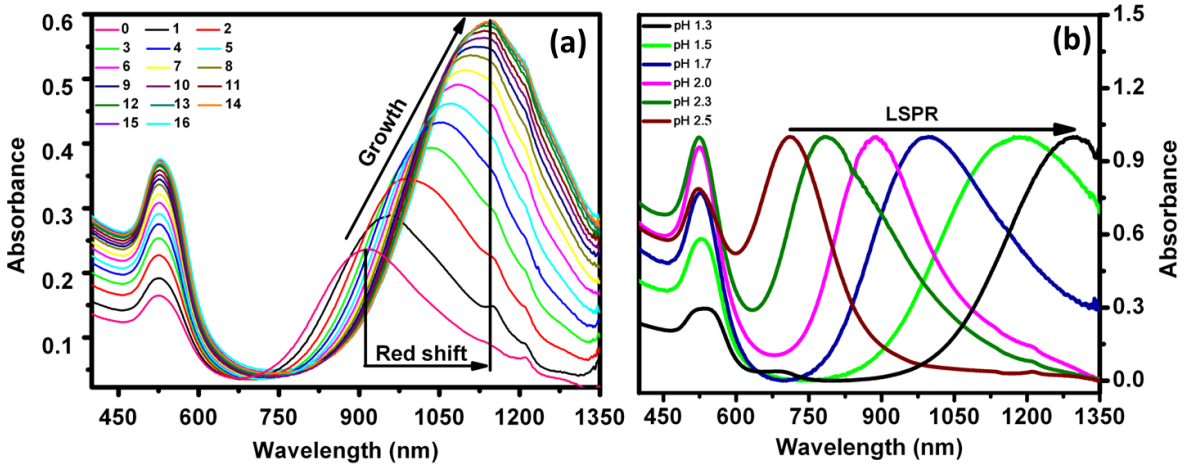

Fig. 6.2 Optical tunability of GNRs synthesized by (a) seeded and (b) seedless approaches.

6.1.3 Stability of GNRs and GNPs

Colloidal stability of as-synthesized GNRs and GNPs has been evaluated by aging them in different media. GNRs preserved in deionized water are most stable. The spectral shift of LSPR band is only 6.5% when stored for 30 days. A plausible mechanism leading to the improved stability in aqueous media is also proposed. Surface driven kinetic control of unzipping of gold ions into the aqueous media is responsible for observed influence of dispersion medium on the colloidal stability and shelf life of GNRs. GNRs prepared via seedless approach has better stability as compared to GNRs prepared by seeded approach (**Fig. 6.3**). The spectral shift in LSPR band of GNRs synthesized by seedless approach is

limited to 0.15% only when stored for a period of 180 days. GNPs preserved in pluronic F-127 have limited stability (spectral shift 1.5% in 42 days) of several weeks. Overall, GNRs are more stable as compared to GNPs and within GNRs, those which are synthesized by seedless approach have better colloidal stability and hence larger shelf life.

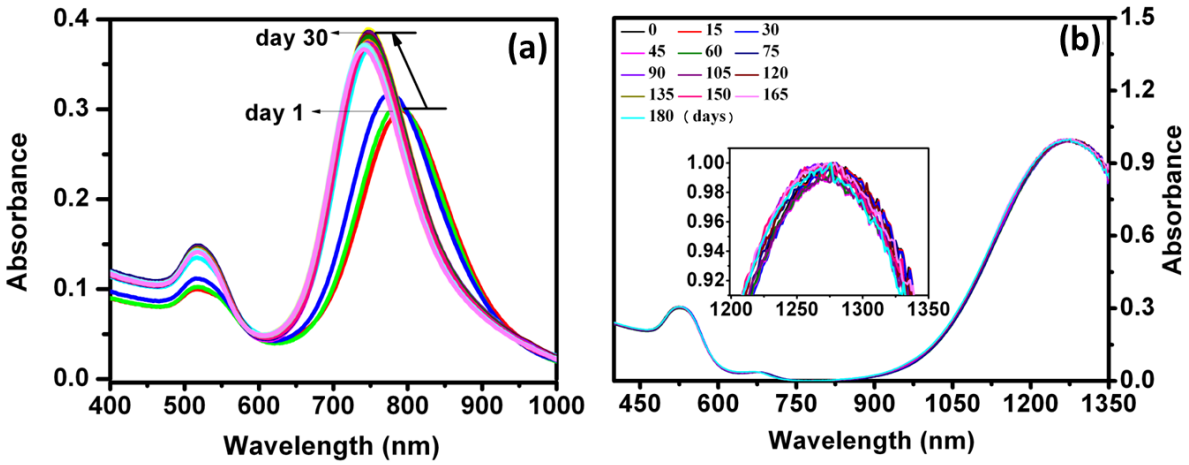

Fig. 6.3 Stability of GNRs synthesized by (a) seeded and (b) seedless approach. Spectral shift is 6.5% (in 30 days) in GNRs synthesized by seeded approach while it is only 0.15% (in 180 days) when synthesized by seedless approach.

6.1.4 Biocompatibility of GNRs and GNPs

GNRs and GNPs show concentration dependent toxicity. Irrespective of concentration, GNRs having smaller aspect ratio (and smaller length, too) are most potent to macrophage cell lines, demonstrating the highest toxicity amongst the tested nanostructures. At low concentrations (≤ 10 μg/mL), GNRs having larger aspect ratio (and larger length, too) have better biocompatibility vis-à-vis GNPs (**Fig 6.4**). However, at higher concentrations, GNPs have lower toxicity as compared to GNPs (having A.R. 8.9). This might be due to the suppression of gold core by biocompatible pluronic F-127 in GNRs. Thus surface chemistry (coating) of nanostructures is a determining factor for the cytotoxicity of gold nanostructures at high concentrations, while the size of the nanoparticles becomes a determinant parameter at low concentrations.

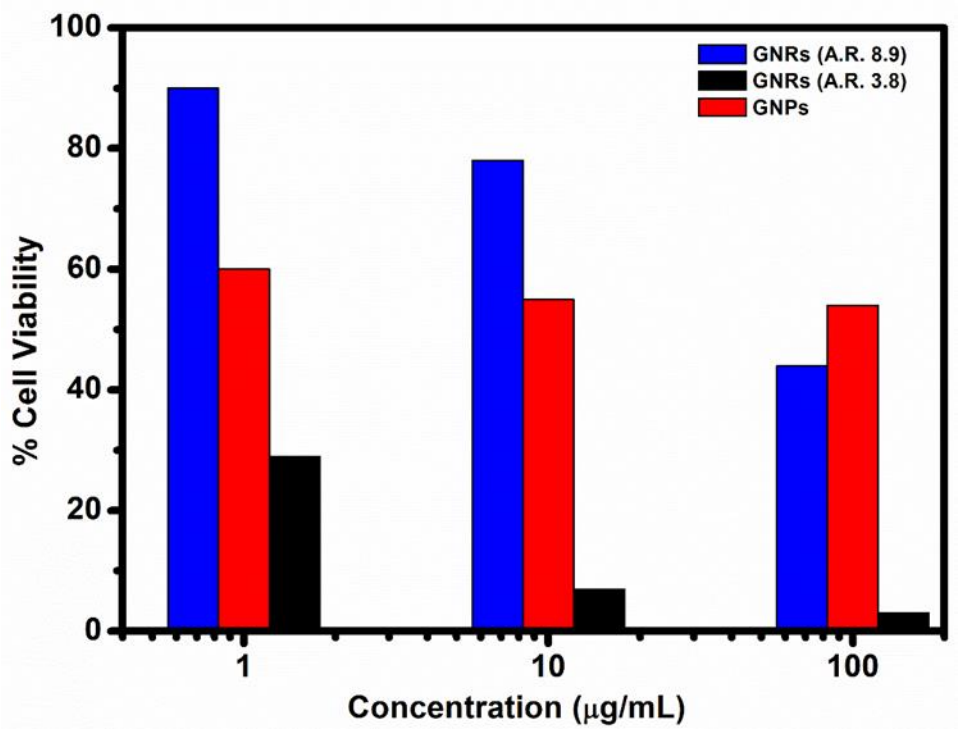

Fig. 6.4 % cell viability of macrophage cell lines against GNRs (A.R. 8.9 and 3.8) and GNPs.

6.2 SCOPE FOR FUTURE WORK

In this thesis protocols for the synthesis of anisotropic gold nanostructures (GNRs and GNPs) with tunable plasmonic properties in the tissue transparent NIR region have been developed. Colloidal stability and shelf life of these nanostructures have been improved by carefully regulating the interaction of the colloidal medium and the surface passivating layers of the nanostructures. We have obtained the stability for 6 months and extensive study for long term is required. These nanostructures have concentration dependent toxicity against RAW 264.7 macrophage cell lines, which can be regulated by modulating the surface chemistry, morphology and hydrodynamic dimensions of nanostructures.

Increasing the GNRs yield is another challenging task and the need of the day to develop a successful plasmonic photothermal therapy. We have been able to grow few milligrams of the sample through both the seed-mediated and seedless synthesis approaches. Further, improvement is required in the growth protocols to increase GNRs yield to grams scale and beyond without compromising their physical and chemical properties.

In-vitro cytotoxicity experiments can be performed on various cancer cell lines to understand the pharmacodynamics of anisotropic gold nanostructures leading to the cell apoptosis. To understand the role of plasmonic properties in the cell apoptosis in plasmonic photothermal therapy, cytotoxicity of gold nanostructures while exposing them with NIR radiations should be determined. This study in conjugation will cell cytotoxicity in the absence of NIR radiation will provide estimates of efficiency of plasmonic photothermal therapy.

Efficiency of plasmonic photothermal therapy strongly depends on the degree of internalization of plasmonic nanostructures in the cellular environment within the cancerous tissues. Various strategies have been developed to improve this internalization in targeted drug delivery of cancer nanomedicine. Amongst them, the most potent approach is to functionalize nanostructures with small biomolecules which provides them the stealth capabilities that can prevent their opsonisation in blood plasma. These biomolecules have differential affinity towards the healthy and cancer tissues and hence improves the internalization of nanostructures in the cancerous tissues. These 'active approach' used in the drug delivery can also be explored further to improve the efficiency of plasmonic photothermal therapy by using functionalized gold nanostructures.

Synergistic effects of traditional cancer therapies are well known. Traditional cancer therapies are used in conjugation with each other to improve the overall efficiency of the treatment. This can also be explored for plasmonic photothermal therapy by combining it with the traditional chemotherapy. Functionalized gold nanostructures can be loaded with anticancer drugs whose release can be trigged by photo or thermal response in tumor environment. This proposed combinational therapy will have better overall efficiency of treatment with minimal side effects.

Every drug / drug carriers need to be tested *in-vivo* in animal models prior to human trials. Once the listed objectives get fulfilled *in-vitro*; they will be tested *in-vivo* in animal models. Considering the complexity of such *in-vivo* experiments, several modifications might be required in the primary design of functionalized gold nanostructures prior to human trials. After successful human trials; plasmonic photothermal therapy stand alone or a combinational therapy in the form of plasmonic photothermal therapy conjugated with

chemotherapy will be used as an affordable model of cancer treatment with high degree of precision. Finally, closer partnership among academic researchers, clinicians, pharmaceutical industries, the National Cancer Institute, and the FDA are necessary to promote the translational research of promising photothermal therapy applications.

ANNEXURE − I

EXPERIMENTAL

Materials

Gold (III) chloride ($HAuCl_4$) (99.9%), silver nitrate ($AgNO_3$) (99.8%), pluronic F-127 (99.9%) and sodium borohydride ($NaBH_4$) (98.0%) were procured from Sigma-Aldrich. Ascorbic acid was obtained from Merck, India. CTAB was purchased from SD-Fine chemicals, India. All chemicals were used as received without further purification. Milli-Q deionized (DI) water (ρ = 18.2 MΩ) was used in all the experiments. The chemical structures of the reagents used for the synthesis of gold nanostructures are shown below:

CTAB

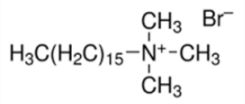

$HAuCl_4$

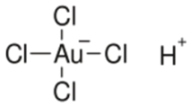

$AgNO_3$

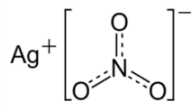

$NaBH_4$

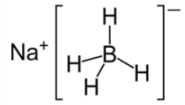

Ascorbic acid

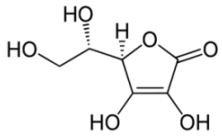

Pluronic F-127

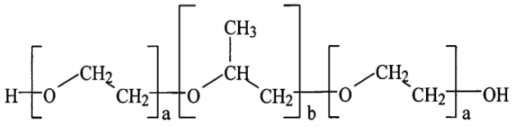

a= 100 and b=66

A1. Seed-Mediated Synthesis of GNRs

Formation of gold seeds: A seed solution was prepared by mixing 5 mL, 0.5 mM $HAuCl_4$ solution to 5 mL, 100 mM aqueous solution of CTAB. For complete dissolution of CTAB, it was sonicated for 15 min at 27 °C. After that, freshly prepared ice cold 0.6 mL, 10 mM $NaBH_4$ was added at once to CTAB-$HAuCl_4$ solution. It was stirred vigorously for two min. The solution color changes from transparent to brownish yellow. This brownish yellow solution contains gold seeds. They were subsequently used for the synthesis of GNRs.

Synthesis of GNRs: In a typical experiment, 5 mL, 0.1-2.0 mM $HAuCl_4$ and 5 mL, 0.01-0.2 M CTAB were mixed. To this solution, 4 mM, 0-1000 µL aqueous solution of $AgNO_3$ was added and shakes gently. 30-50 µL, 0.1 M ascorbic acid was added to this solution. Upon addition of ascorbic acid, the solution turns colorless, indicating the reduction of Au(III) to Au(I). 12 µL of gold seed solution was then added to this colorless growth solution. This process gets completed within 3 min. Formation of GNRs is apparent from the color change of the growth solution, from colorless to pink. Color of the growth solution changes gradually and stabilizes within 20 mins. Growth of GNRs saturates in 24 h. Nanorods were removed from the growth solution by centrifugation. It was centrifuged at relative centrifugal force of 7168g (8000 rpm) for 10 min. Supernatant was removed and equal volume of DI water was added into the precipitates. GNRs were then redispersed by sonication and centrifuged again to remove excess CTAB and water soluble impurities, if any. GNRs were redispersed in DI water and preserved under ambient conditions.

A2. Seedless Synthesis of GNRs

In a typical procedure, the growth solution was prepared by mixing 5.0 mL, 1.0 mM $HAuCl_4$ with 5 mL, 100 mM aqueous solution of CTAB. To this homogeneous mixture of $HAuCl_4$ - CTAB, 4 mM, 0.2 mL $AgNO_3$ was added. 45µL, 0.1 M ascorbic acid was added dropwise to this growth solution, until the solution becomes colorless. Freshly prepared (1-100) µL, 10 mM ice-cold $NaBH_4$ was added into the colorless growth solution to initiate the GNRs growth. Temperature of the growth solution was kept constant at 27 ºC. The color of the growth solution gradually changes from pink to dark red within 2-4 h. Nanorods were allowed to grow for 24 h. GNRs were centrifuged at 10,000 RPM for 10 min. Precipitates of GNRs were redispersed in DI water. This dispersion was again centrifuged at 8000 rpm for

10 min to insure complete removal of excess surfactants and other water soluble impurities, if any. GNRs were preserved in DI water at room temperature.

A3. Seed-Mediated Synthesis of GNPs

Formation of gold seeds: Gold seeds were prepared by reduction of 0.5 mM, 5 mL aqueous $HAuCl_4$, by 10 mM, 0.6 mL ice-cold $NaBH_4$ in the presence of 1 mM, 5 mL pluronic F-127. The color of the solution immediately turned from golden to brownish red. This seed solution was used within 2 h for the synthesis of GNPs.

Synthesis of GNPs: Aqueous solution of 1 mM, 5 mL pluronic F-127 and 1 mM, 5 mL $HAuCl_4$ is prepared separately. To this growth solution 4 mM, 0.2 mL $AgNO_3$ was added. 100 mM, 45 µL ascorbic acid (AA) was added which immediately reduces Au ions and renders the solution colorless. 12 µL seed solution was added to this solution and it was mixed gently. The color of the growth solution turned to light pink immediately on addition of seeds, which further changes to dark-purple within 15–20 min. No further change in the color of the colloid was observed. Throughout the experiment the reaction temperature was maintained at 27 ºC. As-synthesized GNPs were preserved under ambient conditions in 1 mM pluronic F-127.

A4. Seedless Synthesis of GNPs

Growth solution was prepared by mixing 5.0 mL, 1.0 mM $HAuCl_4$ with 5 mL, 100 mM aqueous solution of pluronic F-127. To this homogeneous mixture of $HAuCl_4$ and pluronic F-127, 4 mM, 0.2 mL $AgNO_3$ was added. 45µL, 0.1 M ascorbic acid was added dropwise to this growth solution, until the solution becomes colorless. Freshly prepared 0-100 µL, 10 mM ice-cold $NaBH_4$ was added into the colorless growth solution to initiate the growth of GNPs. The temperature of the growth solution was kept constant at 27 ºC. The color of the growth solution gradually changes from pink to dark red in 10-20 min. GNPs were centrifuged at 10,000 RPM for 10 min. Precipitates of GNPs were redispersed in ultra-pure distilled water. This dispersion was again centrifuged at 8000 rpm for 10 min to insure complete removal of excess surfactants and other impurities. GNPs were preserved in 1 mM pluronic F-127 at room temperature.

A5. Seed-Mediated Tunability of GNRs Synthesized by BDAC-CTAB Co-Surfactant System

Growth solution – A was prepared by mixing 5.0 mL, 0.15 M BDAC and 0.1 g CTAB with 200 μL of 4 mM $AgNO_3$. To this surfactant solution, 5.0 mL of 0.5 mM $HAuCl_4$ was added followed by the addition of 0.1 M ascorbic acid. This reduces Au (III) ions in the growth solution to Au (I) as evidenced from the color change from orange to colorless. 12 μL gold seeds solution was prepared as explained above and was then added to the growth solution. Similarly, Growth solution – B was prepared by following the same steps as explained for Growth solution – A till the reduction of Au (III) to Au (I) by ascorbic acid. This growth solution – B was then added sequentially to growth solution – A in multiple steps of 1 mL each repeated every 20 min. After each successive addition, UV-Visible spectrum was recorded to determine the spectral shift of the GNRs. When the GNRs growth saturates; they were centrifuged twice @ 8500 RPM for 10 min to remove excess surfactant and water soluble impurities, if any. They were preserved under ambient conditions. To evaluate the effect of BDAC-CTAB co-surfactant on the plasmonic properties of synthesized GNRs, their UV-Visible spectra were recorded. The correlation between the tunability of LSPR band of GNRs and serial additions of growth solution containing BDAC-CTAB surfactant have been established.

A6. pH Controlled Tunability of GNRs Synthesized by Seedless Approach Using BDAC-CTAB Co-Surfactant System

In a typical procedure, the growth solution was prepared by mixing 5.0 mL, 0.15 M BDAC with 0.10 gm CTAB. The mixture was sonicated for 30 min at 45 ºC for complete dissolution of BDAC and CTAB. To this homogeneous mixture of BDAC-CTAB, 4 mM, 0.2 mL $AgNO_3$ was added. It was then added to 5.0 mL, 1.0 mM $HAuCl_4$. The pH of the growth solution was adjusted to 1.3-2.5 with HCl. 0.1 M ascorbic acid was added drop-wise to this growth solution, until the solution becomes colorless. Freshly prepared 5-15 μL, 10 mM ice-cold $NaBH_4$ was then added into the colorless growth solution to initiate the nanorods growth. The temperature of the growth solution was kept constant at 27 ºC. The color of the growth solution gradually changes from pink to dark red in 24 h. After 24 h GNRs were centrifuged at 10,000 RPM for 10 min. Precipitates of GNRs were redispersed in ultra-pure distilled water and preserved in ambient conditions. To evaluate the effect of pH on the

plasmonic properties of synthesized GNRs, their UV-Visible spectra were recorded. The correlation between the tunability of LSPR band of GNRs and serial additions of growth solution containing BDAC-CTAB co-surfactant and effect pH have been established.

A7. Seed-Mediated Tunability of GNPs Synthesized by Pluronic F-127

Growth solution –A was prepared by mixing 5.0 mL, 0.01 M pluronic F-127 to 5.0 mL, 1.0 mM $HAuCl_4$. To this homogeneous mixture 4 mM, 0.2 mL $AgNO_3$ was added. Ascorbic acid, 45 µL, 0.1 M was added to reduce Au (III) ions in the growth solution to Au (I). It is evidenced from the color change from light yellow to colorless. Gold seeds solution was prepared by mixing 5 mL, 1 mM pluronic F-127 and 0.5 mM $HAuCl_4$ and reducing it with 0.6 mL, 0.01 M $NaBH_4$. 12 µL this seed solution was then used to grow GNPs. The growth solution – B was prepared by following the same steps as explained for growth solution – A till reduction of Au (III) to Au (I) by ascorbic acid. The growth solution – B was then added sequentially to growth solution – A in multiple steps of 1 mL each repeated every 20 min. After each successive addition, UV-Visible spectrum was recorded to determine the spectral shift of the GNRs. When the GNPs growth saturates; they were centrifuged twice @ 8500 RPM for 10 min to remove excess surfactant and water soluble impurities, if any. They were preserved under ambient conditions. To evaluate the effect of pluronic F-127 on the plasmonic properties of synthesized GNPs, their UV-Visible spectra were recorded. The correlation between the tunability of in-plane resonance band of GNPs and serial additions of growth solution containing pluronic F-127 surfactant have been established.

Characterizations

UV-Visible spectra of as-synthesized gold nanoparticles were recorded on Shimadzu UV-2600 spectrophotometer. Measurements were carried out at room temperature in the spectral range of 400-1400 nm. Transmission electron microscopy (TEM) images were recorded on Philips CM200 transmission electron microscope operating at 200 KV. Samples for transmission electron microscopy were prepared by placing a drop of the colloidal dispersion of gold nanoparticles in DI water onto an amorphous carbon-coated copper grid and the DI water was allowed to evaporate slowly at room temperature. Hydrodynamic particle size and size distribution of gold nanoparticles were obtained by photon correlation spectroscopy (PCS). Measurements were carried out at 25°C on the Brookhaven 90Plus particle size analyzer.